ABSTRACT

SPECIATION OF GASEOUS OXIDIZED MERCURY MOLECULES RELEVANT TO ATMOSPHERIC AND COMBUSTION ENVIRONMENTS

by
Francisco J. Guzman

Mercury is a pervasive and highly toxic environmental pollutant. Major anthropogenic sources of mercury emissions include artisanal gold mining, cement production, and combustion of coal. These sources release mostly gaseous elemental mercury (GEM), which upon entering the atmosphere can travel long distances before depositing to environmental waters and landforms. The deposition of GEM is relatively slow, but becomes greatly accelerated when GEM is converted to gaseous oxidized mercury (GOM) because the latter has significantly higher water solubility and lower volatility. Modeling GOM deposition requires the knowledge of its molecular identities, which are poorly known because ultra-trace (tens to hundreds part per quadrillion) level of GOM in the atmosphere makes its experimental detection and analysis a formidable task. It is here where computational methods can help address the GOM molecular identity problem. Accordingly, the two major goals of this work are to (a) develop a computationally inexpensive approach for assessing accurate thermochemistry of GOM species and (b) investigate ion-molecule reactions of GOM species in order to assist experimentalists in the development of a novel detection method.

The first goal addresses the question of what are some of the molecular identities of GOM species that could be present in combustion and atmospheric environments. *Ab*

initio and density functional theory calculations are used in combination with the methods of isodesmic and isogyric work reactions in order to calculate accurate heats of formation for GOM species that can form in reactions of GEM with atomic halogens, OH, OCl, and OBr. The accuracy of the calculations is assessed by comparing the calculated values against experimental data and data from rigorous and computationally expensive state-of-the-art *ab initio* calculations. Bond dissociation energies (BDE) are determined from the heats of formation and used as a measure of the stability of the GOM species studied.

The second goal of this work addresses the question of how can GOM species be measured in the atmosphere in real-time while retaining speciation information, using chemical ionization mass spectrometry. *Ab initio* and density functional theory calculations are used to determine structures of products of ion-molecule reactions and calculate associated reaction enthalpies and Gibbs free energies. The obtained data are used to identify reagent ions that can be used for atmospheric detection of GOM. The calculations provide an understanding of the complex ion-molecule chemistry that occurs during the chemical ionization process.

The implications of this body of work are as follows. A low computational cost methodology is established that can be used to study a wide range of GOM species outside the scope of this work. The thermochemistry of the GOM species calculated in this work can serve as the foundation for future kinetic studies with the goal of improving the reaction mechanism in global transport models to provide a better understanding of the global mercury budget. Reagent ions identified in this work can be used for real-time speciation of GOM in the atmosphere, using chemical ionization mass spectrometry.

SPECIATION OF GASEOUS OXIDIZED MERCURY MOLECULES RELEVANT TO ATMOSPHERIC AND COMBUSTION ENVIRONMENTS

by
Francisco J. Guzman

A Dissertation
Submitted to the Faculty of
New Jersey Institute of Technology
in Partial Fulfillment of the Requirements for the Degree of
Doctor of Philosophy in Chemical Engineering

Department of Chemical and Materials Engineering

May 2019

APPROVAL PAGE

SPECIATION OF GASEOUS OXIDIZED MERCURY MOLECULES RELEVANT TO ATMOSPHERIC AND COMBUSTION ENVIRONMENTS

Francisco J. Guzman

Dr. Joseph Bozzelli, Dissertation Advisor Date
Distinguished Professor Emeritus of Chemistry and Chemical Engineering, NJIT

Dr. Alexei Khalizov, Dissertation Co-advisor Date
Associate Professor of Chemistry and Environmental Science, NJIT

Dr. Mirko Schoenitz, Committee Member Date
Associate Research Professor of Chemical and Materials Engineering, NJIT

Dr. Robert Barat, Committee Member Date
Professor of Chemical and Materials Engineering, NJIT

Dr. Ilona Kretzschmar, Committee Member Date
Professor and Chair of Chemical Engineering, CUNY City College, New York, NY

BIOGRAPHICAL SKETCH

Author: Francisco J. Guzman

Degree: Doctor of Philosophy

Date: May 2019

Undergraduate and Graduate Education:

- Doctor of Philosophy in Chemical Engineering,
  New Jersey Institute of Technology, Newark, NJ, 2018

- Master of Science in Chemical Engineering,
  Virginia Polytechnic Institute, Blacksburg, VA, 2012

- Bachelor of Engineering in Chemical Engineering,
  CUNY City College, New York, NY, 2009

Major: Chemical Engineering

Presentations and Publications:

Guzman, F. J. and Bozzelli, J. W., "Thermodynamics of OHgX, XHgOH, XHgOCl, XHgOBr, HOHgY gaseous oxidized mercury molecules from isodesmic, isogyric, and atomization work reactions (X = Halogen, Y = OH, OCl, OBr)," Journal of Physical Chemistry A, *In Preparation*.

Guzman, F. J. , Cooper, M., Antley, J. , Bozzelli, J. W. , and Khalizov, A., "Towards direct molecular analysis of atmospheric oxidized mercury," Journal of Physical Chemistry A, *In Preparation*.

Guzman, F. J, Cooper, M., Antley, J., Bozzelli, J. W., and Khalizov, A., "Ion-molecule reactions relevant to the detection of atmospheric oxidized mercury by chemical ionization mass spectrometry," Eastern States Sections of the Combustion Institute, Pennsylvania State University, State College, PA, March 4-7, 2018.

Guzman, F. J, Bozzelli, J. W., and Khalizov, A., "Computational elucidation of the ion-molecule reaction mechanism relevant to the detection of atmospheric gaseous oxidized mercury", 36th Regional Meeting on Kinetics and Dynamics, Northeastern University, Boston, MA, January 27th 2018.

This work is dedicated to my parents (Ancizar and Maria), my wife (Yesica), and son (Adrian). Without you, there is no meaning in any of this.

To my wife in particular, this is the beginning of another chapter in our lives:
Bueno, y ahora que hacemos?

ACKNOWLEDGMENT

I would like to thank my advisors Joseph Bozzelli and Alexei Khalizov for all their constant support, advice and encouragement throughout my studies. I would like to thank my committee members Ilona Kretzschmar, Robert Barat, and Mirko Schoenitz. I would like to thank the Chemical Engineering department and the office of the provost for the teaching assistantships.

I would like to thank the many group members and friends at NJIT I had the opportunity to learn from and collaborate with (Suarwee Yui Snitsiriwat, Suriyakit Pom Yommee, Heng Wang, Douglas Purnell, John Antley, Matt Cooper, Ogochukwu Enekwizu, Jason Hudzik, Itsaso Auzmendi-Murua, Justin Pinca). A special thanks goes to the ARCS staff (Kevin Walsh, David Perel, Gedaliah Wolosh) for the vital computational support.

The journey towards the PhD started a long time ago. Luis Cardoso and Ian Gu gave me my first opportunity at research and began what has become a lifelong calling. Ilona Kretzchmar and John Walz are two people I was very lucky to worth with prior to joining NJIT. There are many more people to thank who in one way or another lead me to this point. To all my friends, colleagues, and family my deepest thanks.

TABLE OF CONTENTS

TABLE OF CONTENTS
(Continued)

TABLE OF CONTENTS
(Continued)

Chapter **Page**

LIST OF TABLES

Table **Page**

LIST OF TABLES
(Continued)

Table **Page**

LIST OF FIGURES

LIST OF FIGURES
(Continued)

Figure **Page**

CHAPTER 1

INTRODUCTION

1.1 Objective

The objective of this dissertation is to broaden our understanding of the molecular identity of gaseous oxidized mercury (GOM) in the environment. Using low cost computational chemistry methods we calculated accurate thermochemistry for numerous GOM molecules, which can potentially exist in the atmosphere or combustion flue gases. We also evaluated thermochemistry of several sets of ion-molecule reactions for the development of a novel GOM detection system based on chemical ionization mass spectrometry. Our calculations identified several reagent ions that can be used for GOM detection and provided insight into the complex chemistry of ion-molecule reactions.

1.2 Mercury Emissions: A Global Problem

Mercury (Hg) is pervasive environmental pollutant[1-5]. Emitted into the atmosphere predominately as gaseous elemental mercury (GEM), mercury can travel large distances from the emission source before depositing unto environmental waters and landforms. The deposition of GEM is relatively slow but becomes greatly accelerated when GEM is converted to gaseous oxidized mercury (GOM or Hg^{II}) because the latter has significantly higher water solubility and lower volatility. $HgCl_2$ for example, has a water solubility of 66 g/L[5] which compared to GEM, which has a solubility ~ 0.5 μg/L[5], is many orders of magnitude larger.

Adding to the complexity is that GOM species are present at trace level concentrations, making the experimental detection a very challenging task. In the continental United States mean total gaseous mercury (TGM) concentrations in the atmosphere[6] are close to 1.2 ng/m^3. There is very little experimental data available and scientists are left with relying on accurate computational chemistry predictions in order to develop chemical models to understand mercury transport and deposition in the environment. Furthermore, due to the large size of the Hg atom (200.5 amu, atomic number 80) highly accurate calculations of GOM species are computationally very expensive and require non-trivial corrections accounting for relativistic effects such as spin-orbit coupling. Although formation of GOM is a key pathway for environmental deposition, GOM formation and speciation is poorly understood and a current area of research.

The chemistry of mercury in the environment is global problem, involving the coupling of chemistry and transport over distances from hundreds to thousands of kilometers. Figure 1.1 shows a schematic of the complex mercury chemistry and transport cycle.

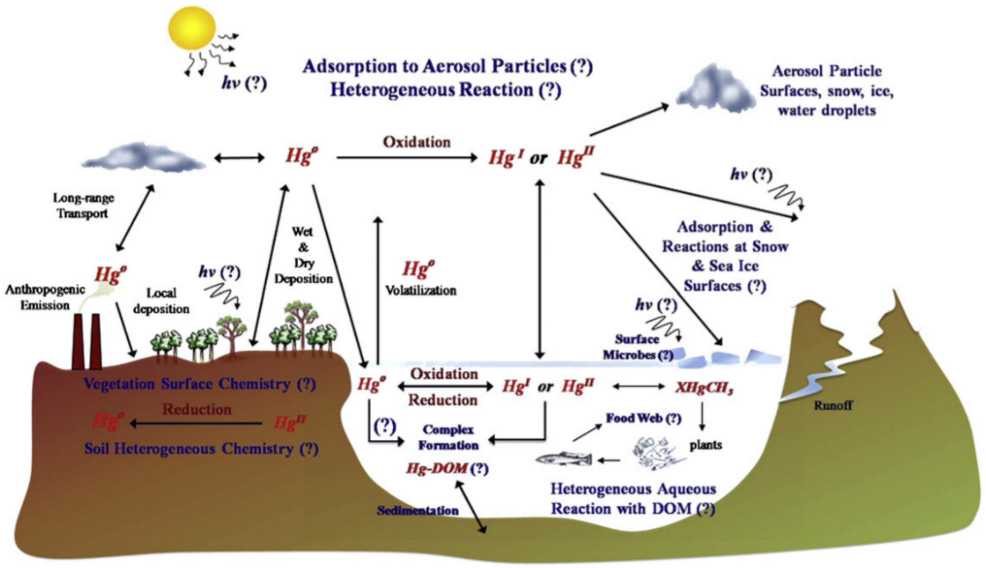

Figure 1.1 Schematic of the mercury transport cycle.
Note: Figure is adapted from Subir et al.
Source: [7]

Once elemental mercury is emitted into the atmosphere, it can undergo several processes, such gas-phase oxidation or heterogeneous reactions on surfaces, before it is deposited to various environmental compartments, such as soil and water. Upon entering those compartments, microorganisms predominately under anaerobic conditions can convert GOM into Methylmercury substances ($MeHg^+$), a highly potent neurotoxin that bioaccumulates due to its lipophilic and protein binding properties [2, 8-9]. The main pathway of $MeHg^+$ into the human diet is thought to be from the consumption of contaminated fish; however, rice grown in contaminated regions can also be an important exposure route[10, 11].

1.3 Sources and Estimates of Mercury Emissions

Major sources of mercury emissions are fossil-fueled power plants, artisanal gold mining, non-ferrous metal manufacturing, cement production, and re-emissions of previously deposited mercury from natural and anthropogenic sources[3]. Between new anthropogenic and natural emissions sources, 70% of the yearly emissions are from natural sources[3]. Clearly, even if all new anthropogenic emissions of mercury are ceased immediately, there is a major mercury re-circulation problem, which must be studied.

Recent calculations by Horowitz et al.[12] for total gaseous mercury (TGM = GEM + GOM) determined a TGM lifetime against deposition of 5.2 months, a tropospheric GEM lifetime against oxidation of 2.7 months, and GOM lifetime of 13 days against reduction and 27 days against deposition[12]. Considering the lifetime of TGM against deposition, the global mass of mercury in the atmosphere was calculated to be 4,400 Mg[12] (1Mg = 1.10 US ton).

The TGM lifetime calculations are based on a GEM-GOM oxidation-reduction mechanism coupled with the GEOS-Chem global chemical transport model. Using meteorological data as the flow field, GEOS-Chem computes atmospheric concentrations depending in part on the chemical model specified. The Horowitz et al. study also includes a 3D ocean circulation model adapted to include geochemical forms and transport of Hg[13] because GOM is water soluble. This approach essentially couples the atmosphere-ocean dynamics, considering both chemistry and transport phenomena.

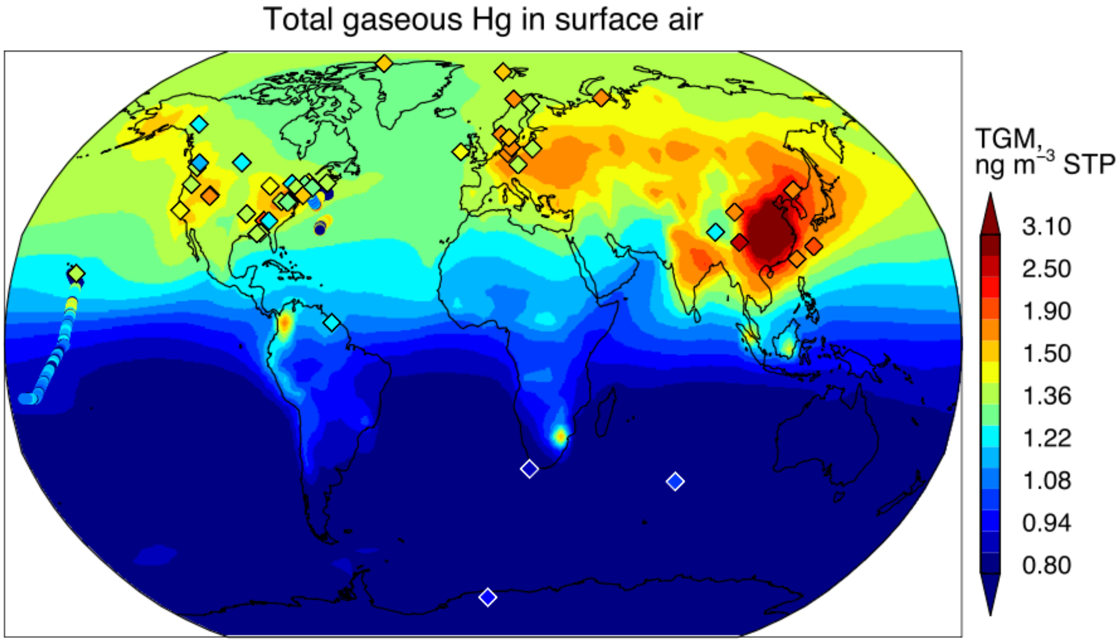

Figure 1.2 Annual means between 2007 and 2011 of the global distribution of total gaseous mercury (TGM). The diamond and circular symbols represent land and oceanic observations, respectively.
Note: Figure is adapted from Horowitz et al.
Source: [12].

Horowitz et al. investigated the monthly seasonality of TGM concentrations from January to December across the northern and southern hemisphere. Figure 1.3 shows the comparison between the simulated and observational data.

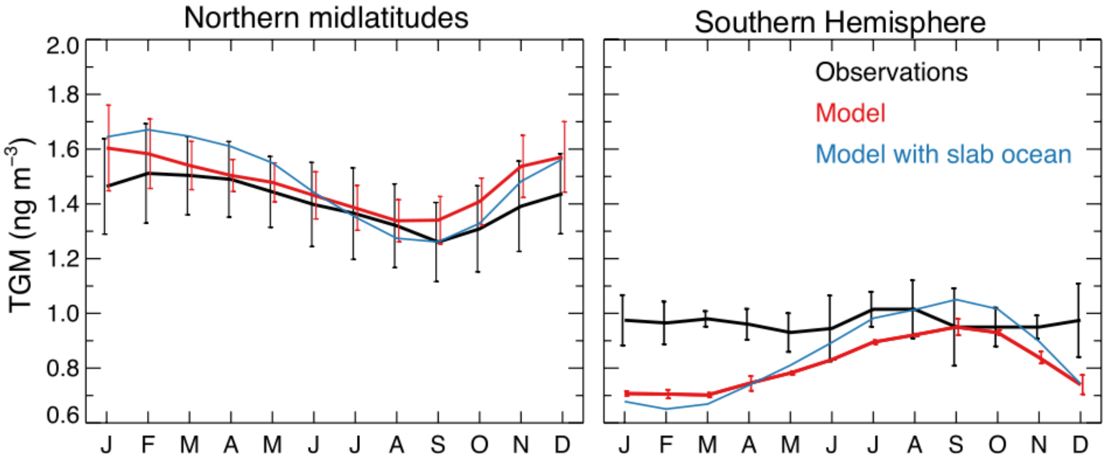

Figure 1.3 Mean seasonal and spatial standard deviation of TGM concentrations between the northern midlatitudes and southern hemisphere. The black, red, and blue lines are observational data, simulated data with a 3D ocean physics model, and simulated data with a 2D slab ocean model with no lateral transport.
Note: Figure is adapted from Horowitz et al.
Source: [12].

As seen in Figure 1.3 the simulated data, including the 3D ocean physics model, is generally in good agreement with the observational data, but there are some discrepancies between the observed and predicted seasonality of TGM in the southern hemisphere. Identifying the exact reason for the discrepancy is a non-trivial task given all the coupled chemical and transport processes in the model. Given the lack of speciation information available for GOM molecules, a plausible explanation could be that key GEM to GOM oxidation-reduction reactions and GOM species may still be missing.

Assessing the global mercury budget requires a fundamental understanding of the GEM-GOM (or Hg^0-Hg^{II}) oxidation-reduction rates. Before discussing the accepted gas phase GEM to GOM reaction mechanism, we first highlight experimental evidence for mercury oxidation-reduction reactions in the atmosphere and during the industrial combustion of coal.

1.4 Empirical Evidence for Gaseous Elemental Mercury Oxidation and Reduction

In 1995, at an Artic measurement site in Alert, Canada, it was discovered that unusually low baseline GEM concentrations occurred during the Artic spring between the months of March and June [14]. This was a surprising result at the time because prior to his study it was thought that the atmospheric lifetime of GEM was between 6 to 24 months. It took several years of measurements before these atmospheric mercury depletion events (AMDE) were considered a real phenomena being first reported literature by Schroeder et al.[14] Since then, several other continuous GEM measurements sites in the artic have been established as shown in Figure 1.4.

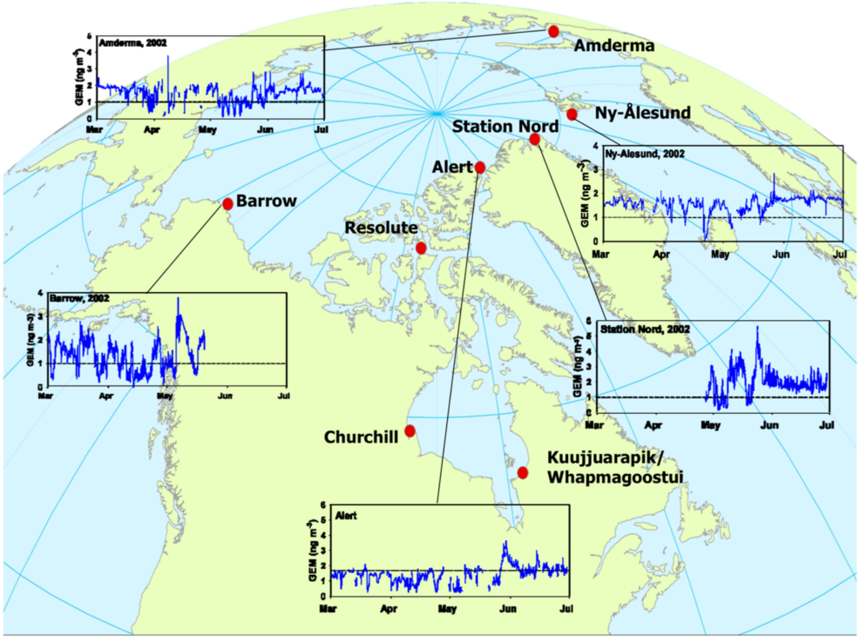

Figure 1.4 Map of surface level GEM sampling sites in the Artic during the Spring of 2002. The insets are the GEM concentration levels as a function of time.
Note: Figure is adapted from Steffen et al.
Source: [15].

Early attempts at identifying this chemistry involved reactions pathways with Br, Cl, BrO, and ClO oxidizing mercury (GEM to GOM oxidation) via the following reaction pathways[17]

$$\mathrm{Br/Cl + O_3 \rightarrow ClO/BrO + O_2} \tag{1.1}$$

$$\mathrm{BrO/ClO + Hg^0 \rightarrow HgO + Br/Cl} \tag{1.2}$$

$$\mathrm{Hg^0 + 2Br/Cl \rightarrow HgBr_2/HgCl_2} \tag{1.3}$$

In these reactions, O_3 first reacts with free Br or Cl forming a halogen monoxide species. The halogen monoxide then reacts with GEM forming HgO. An HgX_2 (X = halogen) GOM species could also be formed via reaction (1.3) where GEM reacts with two of the free halogen radicals. The gas phase oxidation of GEM was also thought to occur via reactions with NO_3 and H_2O_2 such as[14]

$$\mathrm{Hg^0 + NO_3 \rightarrow HgO + NO_2} \tag{1.4}$$

$$\mathrm{Hg^0 + H_2O_2 \rightarrow Hg(OH)_2} \tag{1.5}$$

Since $HgO_{(s)}$ is a well-known solid, it was plausible that HgO should also exist in the gas phase and be an important species explaining the observed AMDE. However, gas phase HgO has been poorly characterized experimentally with Hg-O dissociation energies ranging from 53 +/- 8 [15] kcal/mol to 64 +/- 15 kcal/mol [16]. It was not until the seminal work of Shepler and Peterson[20] that benchmark HgO dissociation energies were determined. They used highly correlated *ab initio* coupled cluster calculations with basis sets close to the complete basis set limit and included corrections for spin-orbit coupling. The ground state bond dissociation was calculated to be 4.0 kcal/mol, which is significantly different from the previously reported dissociation energies. Peterson's reference values makes reactions (1.2) and (1.4) highly endothermic and effectively discards gaseous HgO as a meaningful species relevant to the gas phase oxidation of mercury. Similar results have been observed for the HgS sulfides where the first bond formed is weak, but can be stabilized as more bonds are formed[21]. The rest of the group 12 elements (Zn, Cd, Hg, and Cn) also show a similar behavior[22].

The above example highlights the importance of oxidation of GEM to GOM. Evidence for GOM to GEM reduction has also been observed. Continuous measurements of TGM in-stack and exhaust plume of commercial coal-fired power plants (CFPP) showed in-plume reduction of Hg^{II} to Hg^0[23]. The extent of Hg^{II} to Hg^0 reduction was determined by comparing Hg^0 exhaust plume measurements taken from an airship and TGM measurements in-stack of the CFPP. Relative to the in-stack measurements, the authors observed significant increase of Hg^0 in the exhaust plume. This means that any Hg^{II} or GOM being formed is being reduced back to elemental Hg^0. The authors also noticed that the observed Hg^{II} to Hg^0 reduction was coal blend dependent, but it remains unclear if the determining factor is between the sulfur content, the halogen content of the coal, or another interaction.

A similar study by Deeds et al.[24] also found a reduction in the in-plume GOM concentrations, but explained the reduction in GOM concentration as a plume dilution effect rather than a GOM to GEM reaction in the plume. Although the results of these studies are mixed, we highlight that neither studies could identify a chemical mechanism proving or invalidating the GOM to GEM reduction hypothesis. Other studies have also shown evidence for the reduction of GOM in the atmosphere and the CFPP effluent; however, it remains unclear as to the exact composition of GOM[25-27]. Regardless of the mechanism, having the coal blend characteristics, such as sulfur and halide content, impact the overall TGM speciation and GOM composition would suggest that the coal composition may moderate the near-field impacts as well as affecting remote areas with no local source of Hg emissions[15, 23].

Other potential GOM to GEM reduction pathways could be the photoreduction of Hg^{II} to Hg^0[27]. Figure 1.5 shows the modeled global GEM spatial distributions as a function of the GOM to GEM reduction rate.

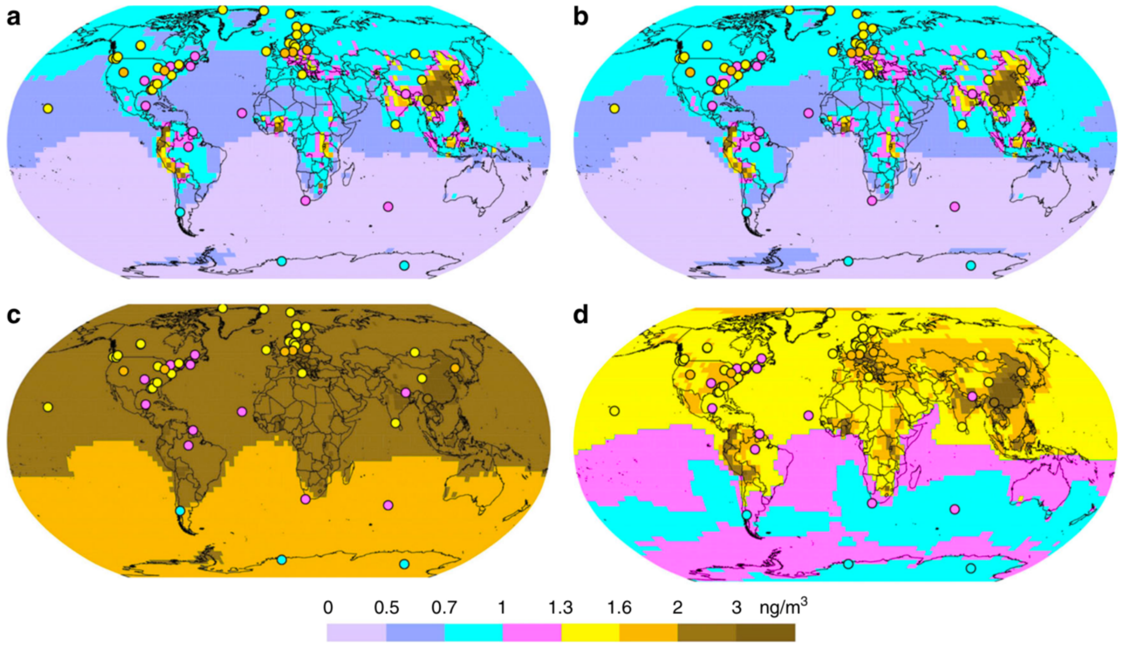

Figure 1.5 Modeled GEM spatial distributions including various Hg^{II} to Hg^0 photoreduction rates: a) No Hg^{II} photoreduction, b) Aqueous phase Hg^{II} photoreduction, c) Hg^{II} to Hg0 photoreduction, and d) Hg^{II} to Hg^I photoreduction. The circles are experimental measurement sites.
Figure is adapted from Saiz-Lopez et al.
Source: [27].

Figure 1.5 shows that the agreement between the calculated GEM distribution and the experimental GEM measurement sites vary significantly as a function of the GOM photoreduction rate included in the model. The best agreement is seen with the inclusion of a Hg^{II} to Hg^I reduction rate (Figure 1.5 d). The Hg^I species formed can then further reduce to GEM because of the relatively weak Hg-X bonds. We note that the recent Horowitz[12] study does not include any GOM-GEM photoreduction reactions, therefore, the calculated lifetimes of TGM could be underestimated. Other GOM to GEM reduction pathways include the aqueous reduction of GOM to GEM[28] or the reduction of GOM in-clouds[29].

The findings of these studies are significant because due to the significant differences in solubilities between Hg^0 and Hg^{II}, any GOM to GEM reduction would affect the GOM deposition rates. Adding to the complexity is that GOM species are at trace level concentrations making the experimental speciation of GOM a very challenging task. Without information on the molecular speciation of GOM, it is extremely difficult to verify a GEM to GOM oxidation-reduction mechanism.

As a result of the trace level concentrations, there is very little experimental data available and scientists are left with relying on accurate computational chemistry predictions to develop chemical models. Furthermore, due to the large size of the Hg atom, highly accurate calculations of GOM species are computationally very expensive and require non-trivial corrections accounting for relativistic effects such as spin-orbit coupling. Before addressing the established chemistry of mercury oxidation-reduction, we first highlight the experimental challenges of measuring GOM.

1.5 Measurement Techniques for TGM and Speciation of GOM

Determining the exact chemical form of GOM is very difficult in part because we do not know what species are being measured. TGM and GOM in the environment can be measured using passive or direct sampling techniques[30, 26]. In passive sampling, gaseous species are captured via diffusion with minimal user control over the sampling rate (SR). Factors affecting the SR are the diffusivity of the gas, the diffusion path length, and the concentration gradient. Design parameters of a passive sampler include the diffusion path length, which is often affected by the external wind speeds that affect the internal turbulence of the system[30]. Higher turbulence promotes higher SR allowing for shorter exposure times, however, the chaotic nature of turbulence leads to spatial concentration gradients potentially lowering the collection efficiency. Hence, passive samplers are often designed to be diffusion limited, but as a consequence require long exposure times on the order of days to weeks [30].

In direct sampling, the user controls the volume of incoming sample allowing for real time measurements and speciation of the sample. A commercially available system is the Tekran® 2537 system where the analyte sample is pre-concentrated in a gold amalgamation process followed by thermal desorption and detection via atomic fluorescence spectrometry. However, GOM speciation information is lost during the thermal desorption which dissociates the GOM species into GEM. For the detection and speciation of atmospheric GOM, the available sampling techniques must have very low detection limits, short sampling times, and avoid transformation of the measured species by either thermal decomposition, transformations in the condensed phase, or surface-catalyzed reactions with the chamber walls.

A class of analytical techniques that can potentially work for GOM speciation are two derivates of chemical ionization mass spectrometry (CIMS): proton transfer reaction mass spectrometry (PTRMS) and ion-drift chemical ionization mass spectrometry (ID-CIMS). PTRMS and ID-CIMS are soft ionization techniques where the analyte is measured as an ion that results from the reaction between the analyte and ions produced from a well from a well characterized reagent source.

The potential for PTRMS as a GOM detection technique is based on a computational study by Dibble et al.[31]. PTRMS uses H_3O^+ ions produced from H_2O to transfer a proton to the target trace gas[32]. A general PTRMS reaction with an arbitrary X species is given as:

$$H_3O^+ + X \rightarrow XH^+ + H_2O \tag{1.5}$$

where the reaction is exothermic if the proton affinity (PA) of X is greater than that of H_3O^+. A typical PTRMS setup consists of an ion source to produce H_3O^+, a drift tube reactor where the proton-transfer-reaction between the H_3O^+ reagent ion and species X takes place, and a mass spectrometer where the product and reagent ions are detected[32]. Advantages of using PTRMS include very high sensitivities ranging from 10-100 pptv, prevention of fragmentation of product ions, and fast response times on the order of 1-10 seconds[32]. Disadvantages include insensitivity to any isomers formed and complexities of interpretations of the mass spectra due to formation of cluster ions. The computational study by Dibble et al. analyzed the protonation of BrHgY species (Y = NO_2, ClO, BrO, HOO) with H_3O^+ and showed the stable products formed where predominately $BrHgYH^+$ [31]. The Dibble study also showed that PTRMS will not work for $HgCl_2$ and $HgBr_2$ because the proton affinities are too low [32]. These computational results can serve as a tool used to interpret the mass spectra generated from a PTRMS measurement.

Although in theory standard PTRMS could be used for GOM detection, several caveats must be accounted for. Either low pressures (~1 Torr) or strong electric field are needed to breakup any $H_3O^+(H_2O)_{n=1,2,..}$ clusters, which are less reactive than H_3O^+. Since the concentration of GOM is very low to begin with, lowering the pressure further dilutes

GOM, making standard PTRMS an impractical approach. For PTRMS to work for GOM speciation measurements, pressures near atmospheric would be required. At atmospheric pressure, voltages about 50 kV would be needed to create electric field strong enough to break up the water clusters. The high electric fields will create a discharge, which could potentially dissociate the GOM species losing the speciation information.

ID-CIMS is similar to PTRMS except that any positive or negative reagent ions can be employed[33]. In ID-CIMS the reaction mechanism for ionization could be either charge transfer, ion transfer, or a combination of the two. In the drift tube, the general reaction scheme for an arbitrary species X and R reagent ion is:

$$X + R^{+/-} \rightarrow X^{+/-} + R \quad \text{(charge transfer)} \qquad (1.6)$$

Example: $HgCl_2 + SF_6{-} \rightarrow HgCl_2{-} + SF_6$

$$X + R'^{+/-} \rightarrow X'^{+/-} + R \quad \text{(ion transfer)} \qquad (1.7)$$

Example: $HgCl_2 + SF_6{-} \rightarrow HgCl_2F{-} + SF_5$

where the prime indicates that an atom has been transferred from the reagent ion to the neutral species. Assuming elementary kinetics, the concentration of the product ion in the drift tube is given by

$$[X'^{+/-} \text{ or } X^{+/-}] = k[R][X]\Delta t \qquad (1.8)$$

where k is the ion-molecule rate constant and the residence $\Delta t = l/U_t$ can be determined from the length of the drift tube, l, and the total flow rate of the reagent ion, U_t. The concentration of species X can then be determined from the ratio of product and reagent ions signals measured from the mass spectrometer as

$$[X] = [X'^{+/-} \text{ or } X^{+/-}]]/(k[R]\,\Delta t) \tag{1.9}$$

This allows for a quantitative measurement of trace species X without the need of performing calibrations with standards of the trace gas[33]. ID-CIMS can thus be used for exploratory studies of yet undetected GOM species.

1.5.2 Selection of reagent ions for ID-CIMS

By using reagent ions other than H_3O^+, a more selective charge/ion-transfer process can be established. To be applicable for the atmospheric GOM detection, a reagent ion should meet the following criteria: (1) the Gibbs energy of reaction between GOM and R should be negative, (2) clustering of the reagent ion with water should be small, (3) reactivity with other trace gases such as O_3 and NO_2 should be low.

Chapter 4 of this dissertation is part of a collaborative study with the group of Dr. Alexei Khalizov, who have developed an ID-CIMS system for use in GOM speciation measurements. We support the development of the system by using computational chemistry methods in order to shed light on the ion-molecule chemistry leading to detected GOM product ions.

1.6 Chemistry of Gaseous Mercury and Gaseous Oxidized Mercury

The current consensus on GEM to GOM oxidation is that it occurs as a two-stage process[12]

$$\mathrm{Hg} + \mathrm{X} \rightarrow \mathrm{HgX} \tag{1.10}$$

$$\mathrm{HgX} + \mathrm{Y} \rightarrow \mathrm{HgXY} \tag{1.11}$$

where X / Y could be any oxidant such as a halogen, NO_x, ClO and BrO. An interesting characteristic of mercury chemistry is that the first Hg-X is significantly weaker than the second XHg-X bond. Consider the reactions

$$\mathrm{Hg} + \mathrm{Cl} \rightarrow \mathrm{HgCl} \tag{1.12}$$

$$\mathrm{HgCl} + \mathrm{Cl} \rightarrow \mathrm{HgCl_2} \tag{1.13}$$

using reference data for Hg ($\Delta H^0_f = 14.67$) ref [19], Cl ($\Delta H^0_f = 28.99$) ref [19], HgCl ($\Delta H^0_f = 18.75$) ref [19], and $HgCl_2$ ($\Delta H^0_f = -34.96$) ref [19] the heats of reaction for Equation (1.12) and Equation (1.13) are -24.91 and -82.7 kcal/mol, respectively. Considering -dHrxn as the bond dissociation energy (BDE), then clearly the second bond XHg–X formed is significantly stronger than the first Hg-X bond. This is because the first HgX species formed is a radical whereas the second XHgX species is a closed shell molecule. This also means that the limiting factor to forming a stable (GOM) species is determined by the bond strength of the first Hg–X bond formed. As a rule of thumb, the BDE of the first

Hg-X bond be should be greater than 10 kcal/mol in order for the HgX species to exist long enough to react with another species X or Y. Additional criterion for the first stage oxidant X include availability near mercury emissions sites and regions where GEM is located, and ideally, a low reactivity of X with non-mercury species.

It is generally accepted that atmospheric mercury oxidation is thought to occur from Br or Cl as the first stage oxidant[12]. Hydroxyl (OH) could be another oxidant, but the Hg-OH BDE is on the order of 10 to 14 kcal/mol making HgOH a relatively short-lived species. In coal fueled power plants (CFPP) environments, where the temperatures are upwards of 600 K, F sources could be an important stage oxidant as F forms the strongest Hg–X bond among all the halogens (see Table 3.13 in Chapter 3). Cao et al. studied the impact of halogen addition on GEM oxidation in CFPP environments[34]. In their study, the authors doped the flue gas with either HF, HBr, HCl, or HI as a halogen source. The results of this study are presented in Figure 1.6. Note, every HX dataset in Figure 1.6 is an independent experiment.

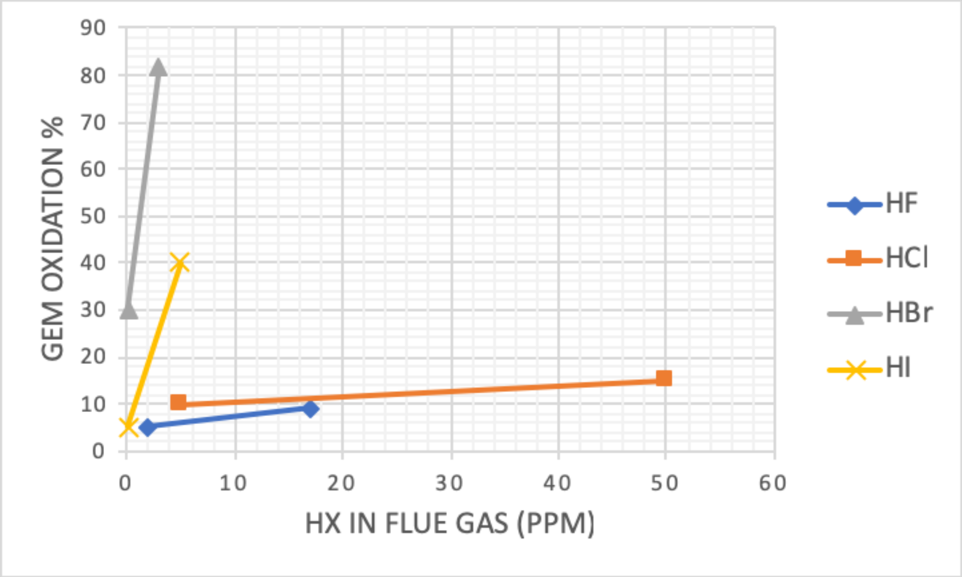

Figure 1.6 Effect of HX on the GEM oxidation rate at T = 620K.
Note: Figure is adapted Cao et al.
Source: [34].

Between the halogens added, Br is the most efficient at oxidizing GEM on a ppm basis. Relative to Cl, the behavior of F in the oxidation of GEM similar. At the elevated CFPP temperatures, the Cao et al. study shows empirical evidence for the oxidation of GEM by F. The mechanism by which F oxidizes GEM is not yet understood. It is likely that the initial HgF species is formed via heterogeneous pathway.

Another potential GOM formation pathway could be via an insertion reaction, such as

$$\mathrm{Hg} + \mathrm{X_2} \rightarrow \mathrm{XHgX} \tag{1.14}$$

$$\mathrm{Hg} + \mathrm{OX} \rightarrow \mathrm{OHgX} \tag{1.15}$$

where X is any halogen species. Table 1.1 shows the calculated heats of reaction for reactions (1.14) and (1.15).

Table 1.1 Reactions Enthalpies for the Hg + X_2 / OX Insertion [a]

Reaction	ΔHrxn (kcal/mol)
Reactions with X_2	
$Hg + F_2 \rightarrow HgF_2$	-84.85
$Hg + Cl_2 \rightarrow HgCl_2$	-49.63
$Hg + Br_2 \rightarrow HgBr_2$	-35.09
$Hg + I_2 \rightarrow HgI_2$	-18.53
Reactions with OX	
$Hg + OF \rightarrow OHgF$	-44.35
$Hg + OCl \rightarrow OHgCl$	-21.34
$Hg + OBr \rightarrow OHgBr$	-18.48
$Hg + OI \rightarrow OHgI$	-10.37

[a] Heats of formation for Hg, X_2, OCl, OHgX, and HgX_2 are in Tables 3.2 and 3.3 in Chapter 3 of this dissertation.

Based on the thermochemistry, reactions (1.14) and (1.15) are exothermic and could potentially be a plausible GOM formation pathway. Unlike the free radical reactions (1.10) and (1.12), reactions (1.14) and (1.15) have significant free energy barriers. Prior computational studies have shown the insertion of Hg + Br_2 / Cl_2 /I_2 to have barriers in the range of 40 kcal/mol[35], making these gas-phase reactions highly unlikely. To the best of our knowledge, there are no studies where the (1.15) insertion reaction barriers have been calculated or experimentally determined.

A third possible GOM formation pathway could be a heterogeneous or interfacial reaction pathway between mercury and a surface. The term surface is loosely defined here and could represent an a water droplet, snow, ice, a soot particle, or the walls of a reactor. Reactions that are endothermic in the gas phase could be catalyzed by a surface or interface. Rigorous theoretical calculations for accurate heterogenous or interfacial reaction predictions, including a transition state prediction, would be best with an *ab initio* molecular dynamics (AIMD)[36] approach.

The AIMD approach uses a molecular dynamics algorithm to move the molecules in space using Newton's equations of motion and density functional theory (DFT) to determine the electronic interactions. Even with DFT, these calculations are very computationally expensive for even the smallest of systems. Adding to the complexity is the requirement of including relativistic corrections due to the atomic size (mass) of mercury. There are also very few experimental data sets available for mercury chemistry so even if the calculations can be properly executed, it would be difficult to gauge their accuracy. Although AIMD calculations are cutting edge and could potentially be used for heterogenous mercury oxidation-reduction reactions, it is outside the current scope of this work.

1.7 Atmospheric and CFPP Combustion Environments

The difference between atmospheric and coal fueled power plants (CFPP) combustion environments relevant to the GEM to GOM oxidation-reduction reactions are the temperatures and the origins of the non-mercury species. The logic of the two-stage gas-phase redox mechanism discussed in Section 1.6 remains the same for both atmospheric and CFPP combustion environments, however, the reactants could be significantly different.

The major first-stage mercury oxidants are generally considered to be halogen radicals (F, Cl, Br, I), hydroxyl (OH), and/or halogen oxide radicals (ClO, BrO). Once the first HgX bond is formed or if a triatomic OHgX is formed, then there are many more species that can lead to a stable GOM molecule. The second stage reactants can be another halogen radical, OH, halogen oxide radicals, HO_2, NO_x, SO_x, and organic hydrocarbon species. Because the limiting step to forming a stable GOM species is the strength of the first HgX bond formed, in this section we will only focus on sources the following first-stage oxidants: F, Cl, Br, and OH. As will be discussed in Chapter 3, many of these species (OCl, OBr, I, NO_x) form bonds that are too weak to be considered first-stage oxidants, but can form the second XHg-X bonds of significant strength in stage two.

In the atmosphere, bromine radicals are thought to be the main stage one oxidant[12]. Atmospheric bromine radicals originate from oceanic emissions of organic bromocarbons[37] such as CH_3Br and CH_2Br_2, as bromide (Br^-) ejected from sea salts aerosols[38], and from the convective transport of photochemically decomposed organobromocarbons[38] from the stratosphere. Most of the oxidation of mercury occurs in the troposphere (lowest region of the atmosphere) following the atmospheric Br distribution[39]. Second to Br, are Cl radicals, which similarly originate from organic chlorocarbons[40] and dechlorination of sea salt aerosols. Once the first BrHg or ClHg bond is formed, second stage oxidants NO_2 and HO_2 can form XHgONO and XHgOOH (X = Br or Cl) as the stable GOM species. It is thought that the dominant GOM species in the atmosphere are BrHgONO and BrHgOOH[12].

In CFPP combustion environments, an additional level of complexity is added depending on the type of coal or coal blend used. The first factor that should be considered is the rank and geologic age of the coal. Figure 1.7 shows the rank, age, and chlorine content of several commercial USA coals.

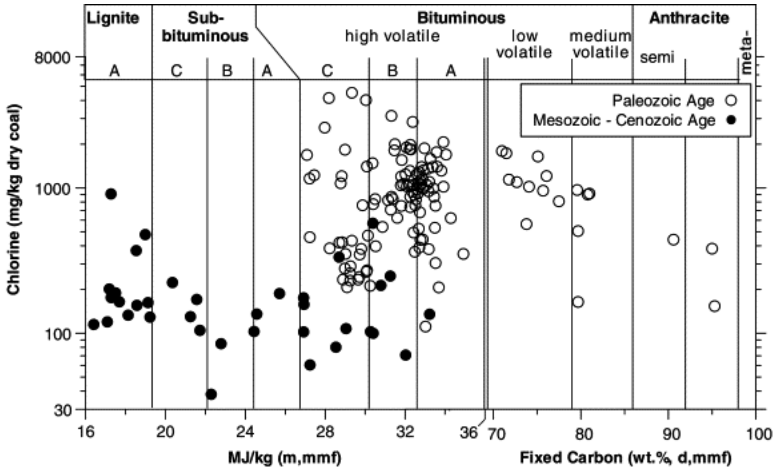

Figure 1.7 Chlorine content, rank, and age of commercial USA coals.
Note: Figure is adapted from Kolker et al.
Source: [41].

The rank of coal is a measure of the carbon content and wetness of the coal. Coals with higher carbon contain less moisture (H_2O) and vice versa. In descending order the coal ranks[42] are: Anthracite (highest grade), Bituminous, Subbituminous, and Lignite. For the geologic eras, the Paleozoic age is 544-245 million years ago and the Mesozoic – Cenozoic era is 66-248 million years ago. As seen in Figure 1.7 and assuming no doping or modification of the coal, the older coals and Bituminous coals have a higher Cl content. A similar trend is seen for the Br content[43] and the same may apply for other halogen species (F and I).

Typical CFPP furnace temperatures are around 1500K. At these elevated temperatures, it is unlikely that any GEM is being transformed into GOM due to the relatively weak intramolecular Hg–X bonds. When the flue gas is processed through air pollution control devices (APCD), there are significant temperature decreases where GOM and particulate bound mercury (PBM) can potentially form. Figure 1.8 shows a schematic of APCD devices in a CFPP.

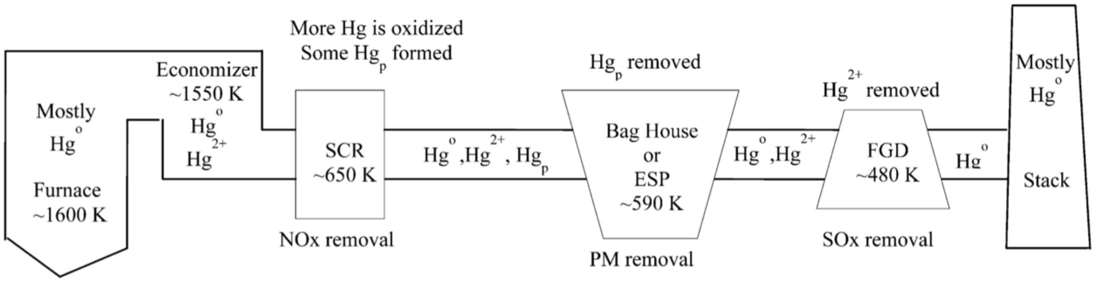

Figure 1.8 Schematic of a CFPP air pollution control device.
Note: Figure is adapted from Auzmendi-Murua and Bozzelli.
Source: [44].

After the flue gas leaves the furnace, it begins to cool as it flows through the multiple APCDs. Economizers are used to recover some of the residual heat from the flue gas and recycle it to preheat the boiler water feedwater. A small reduction in temperature occurs in this step that should promote GEM to GOM oxidation. The selective catalytic reduction (SCR) is used for the removal of nitrogen oxides (NO_x). During this step, there is a significant temperature decrease, further increasing the likelihood of GOM formation. The SCR processes for NO_x removal can potentially catalyze the GEM to

GOM oxidation. The next step in the APCD processes is the removal of particulates from the effluent gas. If there is any PBM present, it will likely be removed here.

Next is the flue-gas desulfurization (FGD) step, which targets the removal of sulfur oxides (SO_x). FGD technologies can include the use of wet-scrubbers, which could also strip any GOM from the effluent gas. A co-benefit of both the SCR and FGD removal technologies is that NO_x, SO_x, and GOM are all simultaneously removed. Technologies specific to Hg removal include doping the flue gas with a Br source[45, 46] or activated carbon[43], promoting GOM or PBM formation. A disadvantage of these technologies is that the addition of halogens causes corrosion problems and even small amounts of activated carbon can absorb the air-entraining agents in the fly ash which are valuable for concrete production[43]. Once the flue gas exits the APCD systems, any remaining mercury is released into the environment.

1.8 Summary

Mercury is a global pollutant governed by a complex set of redox reactions and transport processes. The deposition rate of mercury unto environment sources is dependent on the formation of a water-soluble oxidized form. Mercury is emitted at trace levels concentrations making physical measurements an extremely challenging task. Established measurement techniques do not retain real-time speciation information because of the relatively weak nature of the intramolecular mercury bonds. There is a lack of a fundamental understanding of the molecular identity (speciation) of the mercury species that can exist in the atmosphere or in combustion effluents. The mercury species in the established two-stage gas phase redox mechanism are predominately based on the results of rigorous *ab initio* calculations. Due to the size of the atoms involved, these calculations are prohibitively expensive for many of the mercury species that can potentially exist. Some of the open questions relevant to mercury research include:

1. Is there a computationally efficient approach that can be used for developing accurate gaseous oxidized mercury (GOM) thermochemistry?
2. What are some of the GOM species that can exist and how stable are they?
3. How can GOM be measured in real time without losing speciation information?

The work in this dissertation seeks answers to these questions as follows. We develop an isodesmic / isogyric work reaction scheme that allows for accurate GOM thermochemistry calculations. Work reactions cancel out the errors in the bond energies associated with a calculation method. The work reaction approach costs close to a factor of 20 less CPU time relative to the state-of-the-art *ab initio* methods used for GOM calculations. Establishing the methodology, we calculate thermochemistry for series OHgX, XHgOH, XHgOBr, and XHgOCl molecules (X = Halogen) and calculate the X–Hg–Y bond dissociation energies. We also support the development of an ion-drift chemical ionization mass spectrometry (ID-CIMS) system for real-time GOM speciation measurements. The calculations are used to identify reagent ions viable for the ID-CIMS GOM measurements and provide insight into the complex mercury-reagent ion, ion-molecule chemistry.

CHAPTER 2

THEORETICAL BACKGROUND

2.1 Quantum Mechanics and the Schrödinger Equation

Quantum mechanics is one of the pillars of modern physics. In 1926 Erwin Schrödinger published the Schrödinger equation establishing the basis of quantum mechanics. The Schrödinger equation can be thought of as an extension of some of the principals of classical mechanics (momentum, kinetic, and potential energy) applied to the wavefunction, $\Psi(\vec{\boldsymbol{r}},\mathrm{t})$, where $\Psi(\vec{\boldsymbol{r}},\mathrm{t})$ is used to determine the probability that a particle will be found in a region of space at a given time. The Schrödinger equation is an Eigenvalue equation given as:

$$-\frac{\hbar}{2m}\nabla^2\Psi(\vec{r},\mathrm{t})+V\Psi(\vec{r},\mathrm{t})=i\hbar\frac{\partial\Psi(\vec{r},\mathrm{t})}{\partial t} \tag{2.1}$$

where m is the mass of the system, $\hbar$ is the reduced Planck constant, and V is the potential energy operator of the system. If the solution is restricted to cases where there is no time dependence on the potential energy and assume $\Psi(\vec{\boldsymbol{r}},\mathrm{t})$ is separable, then:

$$\Psi(\vec{r},\mathrm{t})=\Psi(\vec{r})\Psi(\mathrm{t}) \tag{2.2}$$

$$\Psi(t)=e^{-iEt/\hbar} \tag{2.3}$$

$$\widehat{H}\Psi(\vec{r}) = E\Psi(\vec{r}) \tag{2.4}$$

where $\widehat{H}$ is the Hamiltonian operator and E is the Eigenvalue. The Hamiltonian is the sum of the kinetic and potential energy operators, $\widehat{H} = \widehat{T} + \widehat{V} = -\frac{\hbar}{2m}\nabla^2 + V(\vec{r})$. Equation (2.4) is the known as the time-independent Schrödinger equation. Using dimensional analysis, E must have units of energy therefore E is also the energy of the system. In physical chemical systems one is normally concerned about the state of the system and not necessarily the time evolution of the system. Many areas of computational and quantum chemistry dedicated to electronic structure theory have developed on the principal that solving the time independent Schrödinger equation is sufficient for practical chemical accuracy. Time dependent methods such as time-dependent density functional theory (TDDFT) are available but are outside the scope of this work.

2.2 The Adiabatic and Born-Oppenheimer Approximation

The most basic electronic structure method within the construct of the Born-Oppenheimer approximation of the Schrödinger equation is known as Hartree-Fock theory (HF). The Born-Oppenheimer approximation is also referred to the adiabatic approximation. In this context adiabatic does not refer to the thermodynamics definition but rather a quasi-static process. The key points of the Born-Oppenheimer approximation are highlighted, however, a rigorous derivation can be found in Jensen[47].

The Born-Oppenheimer approximation is the assumption that since the motion of electrons is much faster than those of the nuclei, the wavefunction can be decoupled into electronic and nuclear components. Following Jensen[47], the wave function can be written as

$$\Psi(\vec{R},\vec{r}) = \Psi_{nuclear}(\vec{R})\Psi_{electronic}(\vec{r}) \tag{2.5}$$

where $\vec{r}$ denotes the positions of the electrons and $\vec{R}$ the position of the nuclei. Assuming that the full set of solutions to the electronic Schrödinger equation are available, then the wave function can be written as a complete set of solutions over i=1, 2, 3,... electrons as

$$\Psi_{tot}(\vec{R},\vec{r}) = \sum_{i=i}^{\infty}\Psi_{n,i}(\vec{R})\Psi_{i}(\vec{r},\vec{R}) \tag{2.6}$$

Revisiting the Schrödinger equation, the Hamiltonian is transformed to the center of mass of a system expressed as a function of nuclear and electronic operators as follows

$$\begin{gathered}\widehat{H_{tot}}\Psi_{tot} = E_{tot}\Psi_{tot}\\ \widehat{H}_{tot} = \widehat{T}_n + \widehat{H}_e + \widehat{H}_{mp}\end{gathered} \tag{2.7}$$

$$\widehat{H}_e = \widehat{T}_e + \widehat{V}_{ne} + \widehat{V}_{ee} + \widehat{V}_{nn} \tag{2.8}$$

$$\widehat{H}_{mp} = -\frac{1}{2M_{tot}}\left(\sum_{i}^{N_{elec}} \nabla_i\right)^2 \tag{2.9}$$

where the subscript n denotes nuclear coordinates and e denotes electronic coordinates, $\widehat{T}_n = \nabla_n^2$ is the nuclear kinetic energy operator, $\widehat{V}_{ne}$, $\widehat{V}_{ee}$, $\widehat{V}_{nn}$ are the nuclear-electron, electron-electron, and nuclear-nuclear potential energy operators, and M_{tot} is the total mass of the nuclei. $\widehat{H}_{mp}$ is called the mass-polarization and arises because it is not possible to decouple the motion of the center of mass of a system from the internal motion for a system with more than two atoms.

Substituting Equation (2.6) into (2.7) considering that $\widehat{T}_e$, $\widehat{V}_{ne}$, $\widehat{V}_{ee}$, and $\widehat{H}_{mp}$ only operate on the electronic part of the wave function the Schrödinger equation becomes:

$$\sum_{i=1}^{\infty}\left\{\begin{matrix} \Psi_i(\nabla_n^2\Psi_{ni}) + 2(\nabla_n\Psi_i)(\nabla_n\Psi_i) + \\ \Psi_{ni}(\nabla_n^2\Psi_{ni}) + \Psi_{ni}E_i\Psi_i + \Psi_{ni}\widehat{H}_{mp}\Psi_i \end{matrix}\right\} = E_{tot}\sum_{i=1}^{\infty}\Psi_{ni}\Psi_i \tag{2.10}$$

Integrating (2.10) by the complex conjugate of a specific electronic wave function Ψ_j^* and because the solutions are orthornormal ($\left\langle \Psi_i \middle| \Psi_j \right\rangle = \delta_{ij}$ and $\delta_{ij} = 1\ iff\ i = j, else\ \delta_{ij} = 0$ then Equation (2.10) becomes (using bra-ket notation):

$$\nabla_n^2 \Psi_{ni} + E_j \Psi_{nj} \sum_{i=1}^{\infty} \left\{ \begin{array}{l} 2\left\langle \Psi_j \middle| \nabla_n \middle| \Psi_i \right\rangle + \left\langle \Psi_j \middle| \nabla_n^2 \middle| \Psi_i \right\rangle \Psi_{ni} + \\ \left\langle \Psi_j \middle| \widehat{H}_{mp} \middle| \Psi_i \right\rangle \Psi_{ni} \end{array} \right\} = E_{tot} \Psi_j \tag{2.11}$$

In the adiabatic approximation, the solution is limited to only one electronic surface i.e., i = j. The adiabatic approximation is usually good for chemical accuracy for the majority of chemical systems, but can break down for molecules when two or more solutions of the Schrödinger equation are energetically close together. This can occur during a potential energy surface calculation on an X-Y bond, where the molecule can be described by an ionic wave function at the equilibrium distance, but dissociates into two neutral X and Y species, or vice-versa. For the work in this dissertation, the adiabatic approximation is enough for chemical accuracy i.e., errors within 1 kcal/mol. Neglecting the mass polarization term the Schrödinger equation now becomes:

$$\left(\nabla_n^2 + E_j + \left\langle \Psi_j \middle| \nabla_n^2 \middle| \Psi_j \right\rangle \right) \Psi_{nj} = E_{tot} \Psi_{nj} \tag{2.11}$$

The term $\left\langle \Psi_j \middle| \nabla_n^2 \middle| \Psi_j \right\rangle$ is also referred as the diagonal Born-Oppenheimer correction or DBOC. For a H atom, the DBOC is on the order of m_e^3 / m_n^2 which is in essence a reduced mass effect [43]. The effect of the DBOC for large molecules such as Hg should therefore be minimal. Finally, the Born-Oppenheimer approximation reduces the Schrödinger equation to:

$$\left(\nabla_n^2 + E_j\right)\Psi_{nj} = E_{tot}\Psi_{nj} \tag{2.12}$$

which is the functional form of the Schrödinger equation solved by the quantum chemical calculations program used for this dissertation.

2.3 Hartree-Fock Theory

The fundamental *ab initio* method for solving the Schrödinger equation is the Hartree-Fock method (HF) which is also referred to the Self-Consistent-Field (SCF) method. It is a mean field solution to the Schrödinger equation based on solving for the energy of a Slater determinant. Slater determinants are a way of building the anti-symmetry property of the wave function. Slater determinants are a square matrix of a collection of single-electron wave functions (i.e., spin-orbitals or molecular orbitals) for an N number of electrons. A general N electrons and N spin orbital slater determinant is given by:

$$\Phi_{SD} = \frac{1}{\sqrt{N!}} \begin{vmatrix} \phi_1(1) & \phi_2(1) & \cdots & \phi_N(1) \\ \phi_1(2) & \phi_2(2) & \dots & \phi_N(2) \\ \vdots & \vdots & \ddots & \vdots \\ \phi_1(N) & \phi_2(N) & \cdots & \phi_N(N) \end{vmatrix} \tag{2.13}$$

where ϕ are the spin-orbitals. In a Slater determinant, the columns represent different spin orbitals and the rows are the electron coordinates. A significant assumption in HF theory is that the wave function consists of a single Slater determinant. This means that electron correlation is not explicitly considered and that the electron-electron repulsion is considered as an average or mean-field effect. The HF equations are a result of determining the energy of a Slater determinant from the variational principle ($E_0 \le \left\langle \Psi \middle| \widehat{H} \middle| \Psi \right\rangle$), minimizing the energy of the wave function. The Slater determinant can also be written as the diagonal of the determinant multiplied by an anti-symmetrizing operator $\widehat{\mathrm{A}}$. Following Jensen[47]

$$\Phi = \widehat{\mathrm{A}}[\phi_1(1)\phi_2(2)\cdots\phi_N(N)] = \widehat{\mathrm{A}}\Pi \tag{2.14}$$

$$\widehat{\mathrm{A}} = \frac{1}{\sqrt{N!}} \sum_{p=0}^{N-1} (-1)^p \widehat{P} = \frac{1}{\sqrt{N!}} \left[\hat{1} - \sum_{ij} \widehat{P}_{ij} + \sum_{ijk} \widehat{P}_{ijk} - \dots \right] \tag{2.15}$$

where $\hat{1}$ is the identiy operator, $\widehat{P_{ij}}$ are all the possible two electron permutations, $\widehat{P_{ijk}}$ are the 3 electron permutaions, etc. Expanding the operators in (2.8) and collecting according to electron indices, i

$$\begin{aligned}
\widehat{H}_e &= \widehat{T}_e + \widehat{V}_{ne} + \widehat{V}_{ee} + \widehat{V}_{nn} \\
\widehat{T}_e &= -\sum_{i}^{N_{elec}} \tfrac{1}{2}\nabla_i^2 \\
\widehat{V}_{ne} &= -\sum_{A}^{N_{nuclei}} \sum_{i}^{N_{elec}} \frac{Z_A}{\left|\vec{R}_A - \vec{r}_i\right|} \\
\widehat{V}_{ee} &= \sum_{i}^{N_{elec}} \sum_{j>i}^{N_{elec}} \frac{Z_A}{\left|\vec{r}_i - \vec{r}_j\right|} \\
\widehat{V}_{nn} &= -\sum_{A}^{N_{nuclei}} \sum_{B>A}^{N_{nuclei}} \frac{Z_A Z_B}{\left|\vec{R}_A - \vec{R}_B\right|}
\end{aligned} \tag{2.16}$$

$$\begin{aligned}
\hat{h}_i &= -\tfrac{1}{2}\nabla_i^2 - \sum_{A}^{N_{nuclei}} \frac{Z_A}{\left|\vec{R}_A - \vec{r}_i\right|} \\
\hat{g}_{ij} &= \frac{1}{\left|\vec{r}_i - \vec{r}_j\right|} \\
\widehat{H}_e &= \sum_{i}^{N_{elec}} \hat{h}_i + \sum_{j>i}^{N_{elec}} \hat{g}_{ij} + \widehat{V}_{nn}
\end{aligned} \tag{2.17}$$

Combining Equations (2.14) and (2.15) the energy may be written as

$$\begin{aligned} E &= \left\langle \Phi \middle| \widehat{H}_e \middle| \Phi \right\rangle \\ &= \sum_{p=0}^{N-1} (-1)^p \left\langle \Pi \middle| \widehat{H}_e \middle| \widehat{P}\,\Pi \right\rangle \end{aligned} \tag{2.18}$$

Focusing on the $\left\langle \Pi \middle| \widehat{H}_e \middle| \widehat{P}\,\Pi \right\rangle$ part and combining with (2.17)

$$\left\langle \Pi \middle| \widehat{H}_e \middle| \widehat{P}\,\Pi \right\rangle = \left\langle \Pi \middle| \hat{h}_1 \middle| \Pi \right\rangle + \left\langle \Pi \middle| \hat{g}_{12} \middle| \Pi \right\rangle - \left\langle \Pi \middle| \hat{g}_{12} \middle| \widehat{P_{12}}\,\Pi \right\rangle + V_{nn} \tag{2.19}$$

where V_{nn} comes from the fact that $\widehat{V}_{nn}$ is independent of the electron coordinates, thus $\left\langle \Phi \middle| \widehat{V}_{nn} \middle| \Phi \right\rangle = V_{nn} \left\langle \Phi \middle| \Phi \right\rangle = V_{nn}$ since the solutions are orthonormal. Evaluating the remaining terms in Equation (2.19)

$$\begin{aligned} \left\langle \Pi \middle| \hat{h}_1 \middle| \Pi \right\rangle &= \left\langle \phi_1(1) \middle| \hat{h}_1 \middle| \phi_1(1) \right\rangle = h_1 \\ \left\langle \Pi \middle| \hat{g}_{12} \middle| \Pi \right\rangle &= \left\langle \phi_1(1)\phi_2(2) \middle| \hat{g}_{12} \middle| \phi_1(1)\phi_2(2) \right\rangle = J_{12} \\ \left\langle \Pi \middle| \hat{g}_{12} \middle| \widehat{P_{12}}\,\Pi \right\rangle &= \left\langle \phi_1(1)\phi_2(2) \middle| \hat{g}_{12} \middle| \phi_2(1)\phi_1(2) \right\rangle = K_{12} \end{aligned} \tag{2.20}$$

where J_{12} is the Coulomb integral and K_{12} is the exchange integral. The exchange integral has no classical physics analogy and is the result of two electrons being indistinguishable from one another. Re-writing the energy in terms of Coulomb and Exchange operators

$$\begin{aligned}
E &= \sum_{i=1}^{Nelec} \left\langle \phi_i \middle| \hat{h}_1 \middle| \phi_i \right\rangle + \frac{1}{2} \sum_{ij}^{Nelec} (\left\langle \phi_j \middle| \hat{J}_i \middle| \phi_j \right\rangle - \left\langle \phi_j \middle| \hat{K}_i \middle| \phi_j \right\rangle) + V_{nn} \\
\hat{J}_i \left| \phi_j(2) \right\rangle &= \left\langle \phi_i(1) \middle| \hat{g}_{12} \middle| \phi_i(1) \right\rangle \left| \phi_j(2) \right\rangle \\
\hat{K}_i \left| \phi_j(2) \right\rangle &= \left\langle \phi_i(1) \middle| \hat{g}_{12} \middle| \phi_j(1) \right\rangle \left| \phi_i(2) \right\rangle
\end{aligned} \tag{2.21}$$

The method of Lagrange multipliers can now be used to determine a set of spin-orbitals (i.e., Molecular Orbitals) that make the energy a minimum. This method can be used because this is a constrained optimization problem, since the spin-orbitals are required to be orthornormal. This results in the following set of equations

$$\begin{aligned}
L &= E - \sum_{ij}^{Nelec} \lambda_{ij} (\left\langle \phi_i \mid \phi_j \right\rangle - \delta_{ij}) \\
\delta L &= \delta E - \sum_{ij}^{Nelec} \lambda_{ij} (\left\langle \delta\phi_i \mid \phi_j \right\rangle - \left\langle \phi_i \mid \delta\phi_j \right\rangle) = 0 \\
\delta E &= \sum_{i=1}^{Nelec} \left\langle \delta\phi_i \middle| \hat{h}_i \middle| \phi_i \right\rangle + \sum_{i=1}^{Nelec} \left\langle \phi_i \middle| \hat{h}_i \middle| \delta\phi_i \right\rangle + \\
&\quad \sum_{ij}^{Nelec} (\left\langle \delta\phi_i \middle| \hat{J}_j - \hat{K}_j \middle| \phi_j \right\rangle + \left\langle \phi_j \middle| \hat{J}_j - \hat{K}_j \middle| \delta\phi_i \right\rangle)
\end{aligned} \tag{2.22}$$

where λ_{ij} is the Lagrange multiplier. Collecting the $\hat{h}_i$, $\hat{J}_j$, and $\hat{K}_j$ terms leads to

$$\delta E = \sum_{i=1}^{Nelec} \left\langle \delta\phi_i \middle| \widehat{F}_i \middle| \phi_i \right\rangle + \sum_{i=1}^{Nelec} \left\langle \phi_i \middle| \widehat{F}_i \middle| \delta\phi_i \right\rangle$$
$$\widehat{F}_i = \hat{h}_i + \sum_{j}^{Nelec} (\widehat{J}_j - \widehat{K}_j) \tag{2.23}$$

where $\widehat{F}_i$ is defined as the Fock operator or HF Hamiltonian. The final set of HF equation is given by

$$\widehat{F}_i \phi_i = \sum_{j}^{Nelec} \lambda_{ij} \phi_j \tag{2.24}$$

where λ_{ij} is a Hermitian matrix of Lagrange multipliers. Because Hermitian matrices must have real eigen values, Equation (2.24) can be transformed into a pseudo eigen value equation by diagonalizing λ_{ij}. This leads to

$$\widehat{F}_i \phi_i^{'} = \varepsilon_i \phi_i^{'} \tag{2.25}$$

where $\phi_i^{'}$ are a special set of canonical spin-orbitals which make the λ_{ij} matrix diagonal. The expectation value (i.e., the energy) can then be found by integrating (2.25) with the complex conjugate of $\phi_i^{'}$. This leads to

$$\left\langle \phi_i^{'} \middle| \widehat{F}_i \middle| \phi_i^{'} \right\rangle = \varepsilon_i \qquad (2.26)$$

A set of spin-orbitals that is the solution to (2.26) are called the Self-Consistent Field (SCF) orbitals.

A final but important point is the treatment of open shell molecules where there is one or more unpaired electrons (i.e., Doublet, Triplet, …). Within the HF method, there are two main approaches for this: Unrestricted HF(HF) and Restricted Open Shell HF (ROHF). In UHF the spatial orbital of spin-alpha (spin up) are allowed to differ from the spin-beta (spin down) electrons. UHF therefore imposes no restriction on the spin-orbitals used to build the initial Slater determinant for the trial wave function. UHF method leads to lower energies at the cost of spin-contamination of the ground state energy. The spin contamination occurs because the UHF wave function is not a true Eigenfunction of the spin operator ($\widehat{S}^2$). The ground state wave function can therefore include spin-orbitals of higher doublet and triplet states. In ROHF the spin-alpha and spin-beta electrons are paired with the exemption of the unpaired electron. This is clearly a restriction on calculations for open-shell species because we do not know a priori if the unpaired electron is of alpha or beta spin. The alpha or beta spin electron will interact differently with the exchange operator (Equation (2.21)) and could result in different ground state energies. ROHF calculations generally tend to be higher in energy than the UHF. Whether or not ROHF or UHF is a more accurate calculation for a specific system is up to the discretion of the user. Regardless of the approach, once the canonical $\phi_i^{'}$ set of spin-orbitals are determined, they can then be used to build other spin-orbitals such as spin-orbitals accounting hybridization.

Summarizing, the HF method is the first *ab initio* established method for an approximate solution of the Schrödinger equation. The key assumptions built into the HF method are:

1. The Born-Oppenheimer approximation is assumed
2. The wave function is built from a single Slater determinant
3. There is no electron correlation. Electrons interact with each in a mean-field sense via the two electron operators (Equation (2.20))
4. For open shell molecules, UHF is typically lower in energy over ROHF at the cost of some spin contamination.

2.4 Post Hartree Fock Methods: CI, MPn, and CC

The HF method typically accounts for ~99% of the total energy[47]. A significant limitation of the HF approach is the lack of electron correlation. Considering that chemistry generally happens with the valence electrons, errors in the final 1% of the energy could lead to significant changes in the nature of bonds molecules form.

The simplest and most straightforward approach accounting for electron correlation is to build the trial wave function from multiple Slater determinants of varying excitation. The Configuration Interaction (CI) method is oldest method to do so and is expressed as

$$\Psi_{CI} = a_0\Phi_{HF} + \sum_S a_S\Phi_S + \sum_D a_D\Phi_D + \ldots = \sum_{i=0} a_i\Phi_i \tag{2.27}$$

where the subscripts S, D, and i indicate Singly, Doubly, up to the ith excited Slater determinant. Excited Slater determinants are built by moving electrons into unoccupied or virtual orbitals, where the amount of virtual orbitals available depends on the size of the basis set used. The advantage of the CI approach is that by including a large number of excited determinants, most of the correlation energy can be obtained. However, the number of possible excited Slater determinants increases factorially with the number of electrons and basis functions. Consider calculations for one H_2O molecule with the 6-31G(d) basis set up to the 10th exited Slater determinant. The 6-31G(d) basis includes 38 spin-orbitals, of which only 10 are occupied and 28 are unoccupied (i.e., 10 electrons in H_2O, so $38 - 10 = 28$ unoccupied or virtual orbitals). For this relatively small system the number of excited Slater determinants is of the order of 30 million! For calculations of mercury molecules which can have several hundred electrons and basis functions, this approach is effectively ruled out.

A second class of methods accounting for electron correlation are based on the theoretical framework of Many Body Perturbation Theory (MBPT). The idea behind MBPT is that the true energy of the system differs from the approximate solution by small amount or a smalln. A common flavor of MBPT is Møller-Plesset perturbation theory (MPn) where the starting or zeroth order approximation is taken as the solution of the HF equations. The perturbed Hamiltonian equation can be written as:

$$\widehat{H} = \widehat{H}_0 + \lambda\widehat{V} \tag{2.28}$$

where $\widehat{H}_0$ is the HF Hamiltonian , λ is a dimensionless parameter, and $\widehat{V}$ is the perturbed Hamiltonian. The total energy and exact wave function can be expressed as

$$\begin{aligned} E &= E^{(0)} + \lambda E^{(1)} + \lambda^2 E^{(2)} + \lambda^3 E^{(3)} + \ldots \\ \Psi &= \Psi + \lambda^{(1)}\Psi^{(1)} + \lambda^2\Psi^{(2)} + \lambda^3\Psi^{(3)} + \ldots \end{aligned} \tag{2.29}$$

where the superscripts (1), (2), (3), represent the 1st, 2nd, 3rd, …, and nth order perturbations. Expanding the Schrödinger equation and collecting terms over λ leads to

$$\begin{aligned} &\lambda_0 \quad : \widehat{H}_0\Psi_0 = E^{(0)}\Psi_0 \\ &\lambda^{(1)} : \widehat{H}_0\Psi^{(1)} + \widehat{V}\Psi_0 = E^{(0)}\Psi^{(1)} + E^{(1)}\Psi_0 \\ &\lambda^{(2)} : \widehat{H}_0\Psi^{(1)} + \widehat{V}\Psi^{(1)} = E^{(0)}\Psi^{(2)} + E^{(1)}\Psi^{(1)} + E^{(2)}\Psi_0 \\ &\lambda^{(n)} : \widehat{H}_0\Psi^{(n)} + \widehat{V}\Psi^{(n-1)} = \sum_{i=0}^{n} E^{(i)}\Psi^{(n-i)} \end{aligned} \tag{2.29}$$

Equation (2.29) shows how the 1st order perturbation energy depends on the 0th order energy, the 2nd order depends on the 1st, and so on. Although MPn theory can be used to systematically increase the accuracy of the calculated correlation energy, there is no guarantee that the calculations will converge to a finite value. For systems that are multi-reference, such as molecules with degenerate ground states, MPn calculations tend to give erroneous results[47]. In general, the MPn methods are only used up to the 4th order perturbation[47]. For our mercury calculations we do not explicitly use the MPn family of methods, however, some methods such as CCSD(T), include MPn calculations.

Another family of *ab initio* methods accounting for electron correlation are the Coupled Cluster (CC) methods. The concept of CC methods is to include all corrections of a given type (**S**inglet, **D**oublet, **T**riplet, **Q**uadruples, etc.) to an infinite order to the reference HF wavefunction via an excitation operator[47]. Mathematically the CC operator is expressed as

$$\widehat{T} = \widehat{T}_1 + \widehat{T}_2 + \widehat{T}_3 + \ldots + \widehat{T}_N \tag{2.30}$$

where $\widehat{T}$ is the excitation operator, $\widehat{T}_1$ is the operator for the Singly excited states, $\widehat{T}_2$ for the Doubly excited states, etc. The $\widehat{T}_1$ and $\widehat{T}_2$ can act of the reference HF wave function as follows:

$$\begin{aligned} \widehat{T}_1\Phi_0 &= \sum_{i}^{occ}\sum_{a}^{vir} t_i^a \Phi_i^a \\ \widehat{T}_2\Phi_0 &= \sum_{i<j}^{occ}\sum_{a<b}^{vir} t_{ij}^{ab} \Phi_{ij}^{ab} \end{aligned} \tag{2.31}$$

where Φ_0 is the HF reference wave function and t_i are the amplitudes. The amplitudes are equivalent to the CI expansion coefficients (Equation (2.27)). The terms $\widehat{T}_1\Phi_0$ and

$\widehat{T}_2\Phi_0$ thus represent all the possible Singly and Doubly excited states of the reference wave, where the number of states is limited by the size of the basis set. The CC wave function is defined as

$$\Psi_{CC} = e^{\hat{T}}\Phi_0 \tag{2.32}$$

which then transforms the Schrödinger equation to

$$\widehat{H}e^{\hat{T}}\Phi_0 = E_{CC}e^{\hat{T}}\Phi_0 \tag{2.33}$$

Again, it is impossible to include an infinitely large $\widehat{T}_N$ operator, which in theory would provide the exact correlation energy. The CC methods are therefore usually truncated to some excitation level (i.e., S, D, T, or Q). For our mercury calculations, we used a hybrid truncated CC method with single and doublet excitations (CCSD) and a non-iterative triplet contribution evaluated by 4th order MBPT added to the CCSD results (CCSD(T))[47]. Dubbed the "gold standard" as one of main *ab initio* methods accounting for electron correlation, CCSD(T) provides good accuracy at a moderate computational cost. Table 2.1 shows a comparison of the computational cost as a function of basis set for the CI, MPn, and CC methods.

Table 2.1 Comparison of CPU Scaling as a Function of Basis Set

Scaling	Method		
	CI	MP	CC
N_{basis}^5	CIS	MP2	
N_{basis}^6	CISD	MP3	CCSD
N_{basis}^7		MP4	CCSD(T)
N_{basis}^8	CISDT	MP5	
N_{basis}^9		MP6	
N_{basis}^{10}	CISDTQ	MP7	CCSDTQ

Note: Table is adapted from Jensen
Source: [47].

In terms of accuracy the discussed methods follow the following trend[47]: HF << MP2 < CISD < CCSD < MP4 < CCSD(T) < CCSDTQ. For our calculations of mercury molecules the CCSD(T) method is one of the main methods we use.

2.5 The Basis Set Approximation

The *ab initio* methods discussed are, in one way or another, derivatives of the HF method for solving the Schrödinger equation. As demonstrated, the HF method is a technique used to determine the energy of a Slater determinant, which in turn is a matrix of spin-orbitals that give the anti-symmetric property of the wave function. The question remains as to how to build the initial trial wave function that is used for all the HF and Post-HF methods? Because the wave function can be expanded as a linear combination of spin-orbitals, the spin-orbitals can also be expanded as a linear set of basis functions or atomic orbitals. In electronic structure calculations there are two main types of basis functions used: Slater-Type Orbitals (STOs) and Gaussian-Type Orbitals (GTOs). In spherical coordinates these basis functions are

$$\phi_i = \sum_i c_i \chi_i \tag{2.35}$$

$$\chi^{STO}_{\zeta,n,l,m}(r,\theta,\varphi) = NY_{l,m}(\theta,\varphi)r^{n-1}e^{-\zeta r} \tag{2.36}$$

$$\chi^{GTO}_{\zeta,n,l,m}(r,\theta,\varphi) = NY_{l,m}(\theta,\varphi)r^{2n-2-l}e^{-\zeta r^2} \tag{2.37}$$

where N is a normalization constant, $Y_{l,m}(\theta,\varphi)$ are spherical harmonic functions, n and l are the principal and angular quantum numbers, and ζ is the orbital exponent. STOs are usually more accurate than GTOs, however GTOs are easier to integrate and generally preferred over STOs[49]. The best available basis sets for our mercury-containing molecules in our work are constructed from GTOs.

After deciding on the type of basis set to use, the next step is to determine the size of the basis set for accurate electronic structure calculations. The classification of basis sets is as follows. Single Zeta (SZ) basis sets contain the minimum number of basis functions to describe a neutral atom. For a Hydrogen atom, the SZ basis set would contain a single s-function. Double Zeta (DZ) basis sets contain twice the number of basis functions relative to a SZ. Triple Zeta (TZ) basis sets contain three times the number of basis functions, Quadriple Zeta (QZ) four times, and so on. In addition to increasing the size of the basis set, the basis sets can be augmented with functions that capturing physics that the GTOs do not explicitly account for. These can include the addition of polarization or diffuse functions, both of which are important for mercury calculations. Furthermore, the basis sets can be designed to be correlation consistent (cc) which include basis functions that are parametrized to account for some of the correlation energy.

In theory, an infinitely large basis set can be systematically constructed to reach the complete basis set (CBS) limit. The CBS limit gives the best possible calculation for a particular method of choice. However, an infinitely large basis set is impossible to build and very large basis sets (5Z, 6Z, 7Z, etc) are computationally prohibitive for all but the smallest of systems. An alternative approach for reaching the CBS limit is to use a basis set extrapolation scheme, which in theory approaches the CBS energy.

In our calculations, single point CCSD(T) energies were extrapolated to the CBS limit using a 3-point mixed Gaussian exponential formula[47] with the CCSD(T)/AVDZ, CCSD(T)/AVTZ, and CCSD(T)/AVQZ energies as:

$$E(n) = E_{CBS} + Ae^{-(n-1)} + Be^{-(n-1)^2} \qquad (2.38)$$

where A and B are fitting parameters. Solving for E_{CBS} using n=2 for ADVZ, n = 3 for AVTZ, and n = 4 for AVQZ, the $E_{CBS}(2,3,4)$ extrapolated energy is calculated as:

$$E_{CBS}(2,3,4) = \frac{(1+e^2)E_2 - (e+e^3+e^5)E_3 + e^6E_4}{(e-1)(\mathrm{e}^5-\mathrm{e}^2-1)} \qquad (2.39)$$

E_2, E_3, and E_4 are the CCSD(T)/AVDZ, CCSD(T)/AVTZ, and CCSD(T)/AVQZ energies, respectively.

2.6 Relativistic Considerations

The methods and basis sets described have been derived or developed using the non-relativistic Schrödinger equation. The central theme in relativity is that the speed of light is a constant relative to all inertial reference frames. The mass of a particle can therefore be described as

$$m = \frac{m_0}{\sqrt{1 - \frac{v^2}{c^2}}} \tag{2.40}$$

where m_0 is the non-relativistic rest mass, v is the velocity of the particle, and c is the speed of light. For very large atoms, such as Hg, electrons very close to the nucleus have velocities at a significant fraction of the speed of light. This velocity-dependence of the electron mass can cause the s and p orbitals near the nucleus to shrink relative to the non-relativistic orbitals. These smaller s and p orbitals can now screen the effect of the nucleus more, causing an expansion of the d and f orbitals. These cumulative effects can therefore affect the nature of the chemical bonds formed. Another consequence of relativity is the spin-orbit coupling effect. As a thought exercise, if we consider the electron as the reference frame, then from the viewpoint of the electron it would seem that the nucleus is moving about electron, similar to how to the sun seems to rotate about the earth, although we know this is not the case. This relative motion of the nucleus then produces a magnetic field that is dependent on the number of protons of the nucleus (Z). If the magnitude of the magnetic field becomes large enough, then it can change the interaction energy between the nucleus and electron. The Spin-orbit interaction causes a splitting of what would otherwise be a single energy level. Generally, the larger the atom (more protons) the larger the spin-orbit interaction will become.

There are several approaches for considering relativist effects. The first approach is working with the Dirac equation (relativistic Schrödinger equation) and the full four component relativistic wave function. However, these equations are very complicated and expensive to solve. Another approach is to modify the Hamiltonian and include one- and two-electron perturbation-like operators accounting for relativistic effects. Examples of these operators are

$$\begin{aligned}\widehat{H}_e^{SO} &= \frac{g_e\mu_B}{4mc^2}\sum_{i=1}^{N_{elec}}\left[\widehat{s}_i\bullet(\widehat{F}_i\times\widehat{p}_i-\widehat{p}_i\times\widehat{F}_i)\right]\\ \widehat{H}_{ee}^{SO} &= -\frac{g_e\mu_B}{4mc^2}\sum_{i=i}^{N_{elec}}\sum_{i\neq j}^{N_{elec}}\left[\frac{\widehat{s}_i\bullet(\widehat{r}_{ij}\times\widehat{p}_i)}{r_{ij}^3}\right]\end{aligned} \qquad (2.41)$$

where $\widehat{H}_e^{SO}$ and $\widehat{H}_{ee}^{SO}$ are the one and two electron spin-orbit operators, respectively. But again, these calculations are very expensive and there is no guarantee that a convergent solution will be found.

A third approach, and the approach we use for our mercury calculations, is to include relativistic effects with the use of an effective core potential (ECP). The ECPs replace the inner core electrons leaving the valence and outer semi-core electrons for explicit treatment with a correlation consistent basis set. The ECPs are parameterized based on the results of atomic all-electron calculations where all of the electrons are explicitly correlated for a single atom. The idea is that the ECP should in theory capture the relativistic effects of the core electrons in a cost effective manner.

2.7 Basis Sets and ECPs Used

For the molecules in this study, ECPs of the Stuttgart/Köln type were used for Hg[52], Br[53], and I[54]. These ECP's are two-component relativistic pseudopotentials (scalar-relativistic (mass-velocity and Darwin terms) and spin–orbit (SO) terms) that replace the inner core electrons leaving the valence and outer semi-core electrons for explicit treatment with a correlation consistent basis set. The ECP parameters are extracted from relativistic numerical (basis set free) all electron four component multi-configuration Dirac–Hartree–Fock (MCDHF) calculations[52]. The ECP used for Hg is the ECP60MDF[52] which replaces the inner 60 electrons, for Br the ECP used is ECP10MDF[53] which replaces the 10 most inner electrons, and for I the ECP is ECP28MDF[54] where the inner 28 electrons are replaced.

The remaining $5s^2$ $5p^6$ $5d^{10}$ $6s^2$ electrons for Hg[55], $3s^2$ $3p^6$ $4s^2$ $3d^{10}$ $4p^5$ for Br[53], and $4s^2$ $4p^6$ $5s^2$ $4d^{10}$ $5p^5$ electrons for I[54] are treated with triple zeta quality correlation consistent basis set augmented with diffuse functions. These basis sets are denoted in the literature as aug-cc-pVnZ (n = D, T, or Q) or AVnZ for short. It is implied that the AVnZ basis set for Hg, Br, and I includes the ECP. The AVnZ basis sets without an ECP were used for the remaining atoms in the molecules in this dissertation (H'[56], C [57], Cl [58], F [57], O [57], N [57], and S [57])

2.8 Error Cancellation from Work Reactions

Accurate thermochemistry, with errors less than 1 kcal/mol, for the mercury molecules in this study require additional corrections in addition to the use of an ECP. These corrections account for physics that are not accurately calculated by the computational method, basis set, and ECP used. Some examples include core-valence electron correlation, corrections for the lamb shift, and additional corrections for spin-orbit coupling that is not captured by the ECP. A rigorous approach to for determining these effects is however, very computationally expensive and costly to complete across a wide range of molecules. Instead of explicitly including additional corrections to the energies from the computational method, an alternative approach less expensive approach would be to use isodesmic and isogyric work reactions.

In the isodesmic / isogryic work reactions, the enthalpy of reaction (ΔH_{rxn}) is calculated for a hypothetical reaction such as BrHgOBr + H_2O → BrHgOH + HOBr using enthalpies calculated from the same computational method for all molecules in the reaction. In this example, BrHgOBr is the target molecule and H_2O, BrHgOH, HOBr are reference species with well established ΔH^0_f values from either experimental or high-level computational data. Using the calculated ΔH_{rxn}, ΔH^0_f for molecule BrHgOCl is calculated using the reference species as follows

$$\Delta H_{rxn} = \sum H_{product} - \sum H_{reactant} \tag{2.42}$$

$$\Delta H^0_f\,(BrHgOBr, 298K) = \Delta H^0_f(BrHgOH) + \Delta H^0_f\,(HOBr) - \Delta H^0_f\,(H_2O) - \Delta H_{rxn}(298K) \tag{2.43}$$

The advantage of the work reaction approach is that it eliminates errors associated with the computational method of choice. For example, the BrHg–OBr bond length from a CCSD(T)/AVQZ calculation is 1.9995[59]. Including a correction a spin-orbit coupling and core-valence correlation correction reduces the BrHg–OBr bond length to 1.9816. This corresponds to a decrease in the BrHg–OBr bond energy from 56.05 to 53.08 kcal/mol. A similar decrease is also observed for the Br–HgOBr bond length and energies[59]. If we assume that a similar decrease would occur for the Br–Hg and Hg–O bonds in BrHgOH, then when the heat of reaction is calculated (Equation (2.42)), the errors relative to the CCSD(T)/AVQZ calculation for Br–Hg and Hg–O should cancel out. The result is therefore the true or exact energy of the target molecule. With the work reaction approach another advantage is that a lower level of theory, such as a smaller basis set or DFT instead of *ab initio* methods, can in essence also be used because any error associated with the methodology should also be cancelled via Equation (2.42). As will be shown in Chapter 3, this represents significant computational cost savings and allows for the study of significantly more molecules relative to the higher level methods.

Ideally, isodesmic work reactions must be constructed to conserve equal number of each bond type on both sides of the reaction. As first described by Pople and co-workers, isodesmic reactions pose no restrictions on bond order or nearest neighbor interactions and should cancel out errors associated by bond types with relatively simple methods[60]. For Hg-species we are limited by the available reference data and could not always find an isodesmic reaction scheme. Where isodesmic reactions are not possible, we used a series of isogyric work reactions where the number of electron pairs conserved.

We also utilize an atomization reaction scheme[61] (ARM-2) which uses experimental heats of formation for isolated atoms at 298K. The first step in ARM-2 is to calculate the heat of reaction (ΔH_{rxn}) for a molecule going to its constituent atoms at 298K, all at the same level of theory. Heats of formation from high-level computations or experimental data of the constituent atoms at 298K are then used to calculate the enthalpies of a molecule as

$$\Delta H^0_f\,(\text{Molecule, 298K}) = \sum \Delta H^0_f\,(\text{Atom, 298K}) - \Delta H_{rxn}(298\text{K}) \tag{2.44}$$

where $\Delta H_{rxn}(298\text{K})$ is the heat of reaction calculated in the first step. The ARM-2 is particularly useful for thermodynamic property estimates when accurate values of reference species are not available or computational resources are limited.

2.9 Density Functional Theory

The premise of density functional theory (DFT) is based on the proof by Hohenberg and Kohn[62] that the ground state energy can be determined by the electron density, ρ. Once ρ is known, then the wave function can be determined and all the properties of a given system. The ground state energy is therefore a functional of the electron density i.e., $E_0 = E[\rho]$. Unlike wave function methods, where for an N-electron system there are 4N variables (3 spatial coordinates and 1 spin coordinate), there is only one electron density described by one set of spatial coordinates (e.g., x, y, z), independent of the total number of electrons. DFT methods therefore scale as N_{basis}^3 or N_{basis}^4 depending on the DFT method used. This represents a computational cost savings of about a factor of 1,000 relative to the *ab initio* methods commonly used. The Hohenberg and Kohn theorem shows that ρ can be used to determine E_0, however, it does not show how to calculate E_0 from ρ.

The first attempt to determine E_0 from ρ is Kohn-Sham[63] method, which is the basis of the DFT methods used throughout this dissertation. In Kohn-Sham DFT, the energy of a system, where the electrons are correlated, is calculated with respect to a non-interacting system with no electron correlation. The difference in the kinetic and potential energies between the interacting and non-interacting is defined as

$$E_{XC}[\rho] = (T[\rho] - T_s[\rho]) + (V_{ee}[\rho] - V_c[\rho]) \tag{2.45}$$

where the subscript s denotes the non-interacting system, $T[\rho]$ is the kinetic energy, $V_{ee}[\rho]$ is the interacting electron energy, $V_c[\rho]$ is the classic coulomb expression between two electrons, and $E_{XC}[\rho]$ is called the exchange-correlation energy. The problem with solving for $E_{XC}[\rho]$ is that $T[\rho]$ and $V_{ee}[\rho]$ are also unknown functionals.

This is the main issue with DFT methods. There is no universal approach for solving $E_{XC}[\rho]$ and, as a result, there is no universal DFT method that works for every system.

Appropriate selection of a DFT method is based on previous experience and on a case by case basis. In developing DFT functionals, there are three general approaches for achieving chemical accuracy. Functionals can either be parameterized to fit a robust set of experimental data, constrained to fulfill well-known universal physical constraints, or a combination of the two. Parameterized functionals offer high accuracy when applied to systems represented by the fitted data, however caution is needed for molecules with properties outside the scope of the parametrization databases. Constrained functionals should in practice offer accuracy over all systems at the cost of less accuracy compared to functionals parameterized for specific systems.

The DFT methods used throughout this dissertation are M06-2X and PBE1PBE, the latter is also known in the literature as PBE0.

M06-2X is a parametrized global hybrid meta-generalized gradient-approximations (hybrid meta-GGA) functional part of the M06 family of functionals developed by the Truhlar group[93]. GGA functionals make the exchange and correlation energies depend on the first derivate electron density as well as the local electron density as given by the local spin density approximation (LSDA). Global hybrid GGA functionals replace a constant percentage of the local exchange by Hartree-Fock (HF) exchange. HF exchange is the energy of a Slater determinant built from Kohn-Sham orbitals solved using the HF self-consistent field (SCF) method. This is not the same as the HF exchange energy from the SCF method since Kohn-Sham orbitals are used.

Adding HF exchange is an improvement over GGA and LSDA functionals because it removes some of the self-interaction energy. That is, the Coulomb and Exchange self-interaction energies cancel each other out in HF theory. Hybrid meta-GGAs include additions to the functional form of GGA functional such as second derivatives of the spin densities or second derivatives of the spin-labeled non-interacting kinetic energy densities[94]. For M06-2X the hybrid exchange-correlation energy is given as

$$E_{XC}^{M06-2X} = \frac{X}{100} E_{XC}^{HF} + \left(1 - \frac{X}{100}\right) E_{X}^{DFT} + E_{C}^{DFT} \tag{2.46}$$

where E_{XC}^{HF} is the nonlocal HF exchange energy, X is the percentage of HF exchange, E_{X}^{DFT} is the local DFT exchange energy, and E_{C}^{DFT} is the local DFT correlation energy. For M06-2X the percentage of HF exchange is 54% and the expressions for E_{X}^{DFT} and E_{C}^{DFT} can be found in Zhao and Truhlar[93].

PBE0[95-97] is a hybrid GGA functional that is constructed to satisfy physical constraints whereas M06-2X is parameterized only for non-metals. In PBE0 the exchange-correlation energy is given as

$$E_{XC}^{PBE0} = E_{XC}^{GGA} + a_1\left(E_{X}^{HF} - E_{X}^{GGA}\right) \tag{2.47}$$

where E_{XC}^{GGA} is the Pardew, Ernzerhof, and Burke (PBE) GGA exchange-correlation functional and a_1 is a mixing coefficient set to 25%. From our previous studies[44] and that of the group of Dibble[64], M06-2X and PBE0 have shown to give reliable structures and accurate thermochemistry for Hg molecules .

An ultrafine pruned integration grid consisting of 99 radials shells and 990 points/shell was used for all DFT/AVTZ calculations. Geometry optimizations were done at the DFT level with a very tight convergence criterion, setting the root meat squared value of the force to $1x10^{-6}$.

2.10 Calculation of Ion-Molecule Reaction Rates

Chapter 4 of this dissertation is concerned with ion-molecule reactions with mercury molecules and a reagent ions. In order to determine the reaction rate constants, average dipole orientation (ADO) theory was used to calculate the high pressure limit value of ion-molecule collision reaction rate constant. The ADO rate constant expression is given by [65, 66]:

$$k_{ADO} = (2\pi q / \mu^{1/2})[\alpha^{1/2} + C\mu_D(2/\pi k_B T)^{1/2}] \tag{2.48}$$

where q is the charge of the ion, μ is the reduced mass of the reactants, k_B is the Boltzmann constant, α are the isentropic components of the polarizability tensor, and μ_D is the dipole moment. Both α and μ_D are determined from M06-2X/AVTZ calculations of the neutral molecule. *C* is a parameter ranging between 0 and 1 describing the effectiveness of the charge "locking in" the dipole. For a constant temperature, *C* is given by the expression $C = f(\mu_D / \sqrt{\alpha})$. If $\mu_D = 0$, then C = 0 and k_{ADO} reduces to the Langevin rate constant:

$$k_{ADO} = k_{LAN} = (2\pi q / \mu^{1/2})\alpha^{1/2} \tag{2.49}$$

2.11 Software Used

Ab initio and Density Functional Theory calculations were carried out using Revision C.01 of the Gaussian 09 program[67].

CHAPTER 3

THERMODYNAMICS OF OHGX, XHGOH, XHGOCL, XHGOBR, HOHGY GASEOUS OXIDIZED MERCURY MOLECULES FROM ISODESMIC, ISOGYRIC, AND ATOMIZATION WORK REACTIONS (X = HALOGEN, Y = OH, OCL, OBR)

3.1 Abstract

Isogyric, isodesmic, and atomization reactions were used to determine the standard enthalpies of formation (ΔH^0_f) for a series of OHgX, XHgOH, XHgOCl, XHgOBr, HOHgY molecules (X = Halogen, Y = OH, OCl, OBr) from single point CCSD(T)/AVnZ//M06-2X/AVTZ (n = D, T, Q) energies extrapolated to the complete basis set limit using a 3-point mixed Gaussian exponential scheme. Standard enthalpies of formation from isogyric and isodesmic work reactions are in–good agreement with experimental data and values from higher-level calculations, but at significantly reduced computation time. The established template work reaction scheme and methodology can potentially be extended for Hg species outside the scope of this work. The standard error in the ΔH^0_f for the studied molecules averaged over several isodesmic/isogyric work reactions is 1.67 kcal/mol or less. The X–Hg–Y bond dissociation energies (BDE) were determined from the ΔH^0_f and used as a metric of the molecular stability. The BDE decreases from F to I for the X–HgOH and OHg–X series. The trend is reversed for X–HgOCl and X–HgOBr where the BDE increases from F to Br, but decreases with I. All the studied molecules have significant BDE's in the range of 50-90 kcal/mol. Assuming that the concentrations of atomic halogens, OH, OCl, or OBr are reasonably high near the

vicinity of a mercury emission source, the studied molecules can be produced and exist long enough to affect the mercury oxidation-reduction rate and impact the global mercury budget**.**

3.2 Introduction

Understanding the exact molecular identity of GOM is of critical importance. Due to the trace level concentrations of GOM the exact molecular identity of GOM is unknown and a current subject of debate. It is here where computational methods can help address the GOM molecular identity problem by calculating accurate thermochemistry of GOM molecules and assessing their relative stability from their bond dissociation energies.

State of the art computational methods for GOM species use single point CCSD(T) energies extrapolated to the complete basis set (E_{CBS}) and include additive corrections accounting for core-valence correlation (ΔE_{CV}), scalar relativistic effects (ΔE_{SR}), spin-orbit coupling corrections (ΔE_{SO}), and corrections for the Lamb shift (ΔE_{Lamb}). These rigorous calculations are, however, very computationally expensive and costly to complete across a wide range of molecules. In our approach, we use isodesmic and isogyric work reactions as a method of correcting for errors associated with the computational methodology. Our methodology is almost a factor of 20 times less CPU intensive, allowing for the study of significantly more GOM molecules at a comparatively low computational cost.

The use of isodesmic and isogyric work reactions is highly dependent on the available references enthalpies. This is a significant limitation for mercury calculations with this method because there are very few mercury reference molecules available. We begin building our GOM thermochemistry for small GOM molecules from work reactions with enthalpies available from the literature. We then use these molecules as references for the larger GOM species. We then compare results from work reactions using only literature reference data with those using our calculated values as the reference. We also compare our calculations to established experimental data[19] and the rigorous calculations by the groups of Peterson [68, 69] and Dibble[59].

Some GOM species of interests are those that can potentially be formed from reactions with halogen radicals (F, Cl, Br, I), hydroxyl (OH), and halogen oxides radicals (ClO, BrO). The selection of the reacting molecules was based on the following criterion. Cl and F are present in significant concentrations in coal[43]. Bromine is considered among the main oxidants for Hg in the atmosphere[12] as part of a two stage oxidation mechanism. Bromine can also be used as a Hg emissions control technology[45, 46] oxidizing mercury in the flue gas. Iodine can also be an effective Hg oxidizer under combustion conditions[35]. ClO and BrO are highly reactive radicals important in tropospheric chemistry[39, 70]. OH is a very important and reactive radical in both atmospheric and combustion chemistry.

The thermochemistry of the GOM species calculated in this work can serve as the foundation for future kinetic studies with the goal of improving the reaction mechanism in global transport models used to provide a better understanding of the global mercury budget. We hypothesize that deviations of the current state of the art global Hg prediction models from experimental field observations[12] are due to lack of thermochemical and speciation information.

3.3 Results and Discussion

3.3.1 Assessment of Computational Methodology

A template work reaction scheme for OHgX and XHgOY (X = halogen, OH, Y = halogen or H) molecules is shown in Table 3.1.

Table 3.1 Template Work Reactions used in Calculations of Heats of Formation

No. of Atoms	Template work reaction	Reaction type
Triatomic	**•OHgX** + HX →HgX_2 + •OH	Isogyric
	•OHgX + H_2 →HX + •OH	Isogyric
	•OHgX + •HgY →•OHgY + •HgX	Isodesmic
Tetraatomic	**XHgOH** + •OH →•OHgX + H_2O	Isodesmic
	XHgOY + HY → HgX_2 + CH_3OY	Isogyric
	XHgOY + H_2O → XHgOH + HOY	Isogyric
	XHgOY + CH_3OH → XHgOH + CH_3OY	Isodesmic
Pentaatomic	**HOHgOY**+ HY → HOHgY + HOY	Isogyric
	HOHgOY+ H_2O→ $Hg(OH)_2$ + HOY	Isodesmic
	HOHgOY+ CH_3OH → $Hg(OH)_2$ + CH_3OY	Isodesmic

Several isogyric and isodesmic reactions schemes were developed for the tri-atomic, tetra atomic, and penta atomic GOM molecules. Standard enthalpies of formation for the OHgX, XHgOH and XHgOY species were calculated by averaging over the work reactions for each species. The same level of theory was used for every molecule in a specific reaction. Tables 3.2 and 3.3 show the values for the reference species used in the reactions.

Table 3.2 Reference Heats of Formation for Molecules with Mercury

Molecule	ΔH^0_f (298K) (kcal/mol)	Molecule	ΔH^0_f (298K) (kcal/mol)
Hg	14.67[19]	HgO	69.49[a,][20][,c]
HgF	0.7 [19]	HgOH	9.38[b]
HgCl	18.75 [19]	HgF_2	-70.18[19]
HgBr	24.9 [19]	$HgCl_2$	-34.96 [19]
HgI	31.9 [19]	$HgBr_2$	-20.42 [19]
OHgCl	16.8 [a,] [68]	HgI_2	-3.86 [19]
OHgBr	26.14 [a,] [68]	BrHgOCl	-2.20[59]
OHgI	32.39 [a,] [68]	BrHgOBr	0.9 [59]

[a] Values converted from 0 K to 298K for use in this study. [b] Calculated using error cancelling work reactions. [c] It is noted that using the gas phase $\Delta_f H^o_{298}$ values for atomic oxygen O^{3p} and elemental gas phase Hg^o, this molecule is not stable under standard atmospheric conditions, O is 59.6, Hg is 14.7 = 74.3, Hg–O bond energy is 4.8 kcal mol^{-1}.

Table 3.3 Reference Heats of Formation for Non-Mercury Molecules

Molecule	ΔH^0_f (298K) (kcal/mol)	Molecule	ΔH^0_f (298K) (kcal/mol)
H	52.10 [71]	HBr	-8.67 [71]
F	18.98 [71]	HI	6.33 [71]
Cl	28.99 [71]	OH	9.319 [71]
Br	26.73 [71]	HOCl	-18.36 [71]
I	25.52 [71]	HOBr	-14.78 [71]
CH_4	-17.54 [71]	H_2O	-57.79 [71]
CH_3	35.00 [71]	CH_2FOH	-101.9 [72]
C_2H_6	-20.07 [71]	CH_3F	-55.99 [71]
C_2H_5	28.65 [71]	CH_3Cl	-19.59 [71]
O	59.56 [71]	CH_3Br	-8.2 [71]
OH	9.32 [71]	CH_3I	3.57 [71]
OCl	24.31 [71]	CH_3OH	-48.02 [71]
OBr	29.54 [71]	CH_3OCl	-15.41 [73]
HF	-65.32 [71]	CH_3OBr	-10.66[a]
HCl	-22.06 [71]	CH_2Cl_2	-22.83 [73]

[a] Value calculated by using work reactions 1, 3, 4, 5, and 7 of Jung et al. [73] with F atoms changed to Br. Value shown is from $E_{CBS}(2,3,4)$ calculations averaged over the modified work reactions

We note that there is interdependency across some of the isodesmic / isogyric work reactions that could lead to a systematic accumulation of error. This is most evident in our calculations for $Hg(OH)_2$, HOHgOCl, and HOHgOBr where ΔH^0_f for $Hg(OH)_2$ depend on the values of XHgOH, and HOHgOCl and HOHgOBr depend on $Hg(OH)_2$ and XHgOH. For example, the isogyric work reaction HOHgOCl + HCl → ClHgOH + HOCl requires knowledge of the ΔH^0_f for ClHgOH. Since ΔH^0_f for ClHgOH was also calculated using several work reaction schemes, any error associated with this calculation would propagate to ΔH^0_f for HOHgOCl. Detailed results calculated using isodesmic or isogyric reactions using DFT (M06-2X/AVTZ) and single point CCSD(T)/DFT data Extrapolated to the Complete Basis Set Limit ($E_{CBS}(2,3,4)$) using a mixed Gaussian-Exponential extrapolation with AVDZ, AVTZ, and AVQZ basis sets are presented in Table 3.4.

Table 3.4 Heats of Formation for HOHgY (Y = OH, OCl, and OBr) Averaged over Multiple Work Reactions. Isodesmic Reactions are Marked with an Asterisk *. E_{CBS}(2,3,4) Values are Recommended

Work Reaction	**M06-2X/ AVTZ**	**E_{CBS}(2,3,4)**
	ΔH_F (298K) (kcal/mol)	
$Hg(OH)_2 \rightarrow 2H + 2O + Hg$ **(ARM-2[a])**	-49.95	-55.56
$Hg(OH)_2 + HgCl_2 \rightarrow ClHgOH + ClHgOH$ *	-37.74	-56.68
$Hg(OH)_2 + HgBr_2 \rightarrow BrHgOH + BrHgOH$ *	-57.61	-57.13
$Hg(OH)_2 + HgF_2 \rightarrow FHgOH + FHgOH$ *	-54.94	-55.10
AVG/STDEV	**-50.10 +/- 10.78**	**-56.30 +/- 1.07**
$HOHgOCl \rightarrow H + 2O + Hg + Cl$ **(ARM-2[a])**	-15.64	-19.80
$HOHgOCl + HBr \rightarrow BrHgOH + HOCl$	-17.79	-20.83
$HOHgOCl + H_2O \rightarrow Hg(OH)_2 + HOCl$ *	-17.73	-20.67
$HOHgOCl + CH_3OH \rightarrow Hg(OH)_2 + CH_3OCl$ *	-19.25	-20.99
$HOHgOCl + HCl \rightarrow ClHgOH + HOCl$	-9.09	-20.80
AVG/STDEV	**-15.97 +/- 4.64**	**-20.82 +/- 0.13**
$HOHgOBr \rightarrow H + 2O + Hg + Br$ **(ARM-2[a])**	-9.85	-21.06
$HOHgOBr + H_2O \rightarrow Hg(OH)_2 + HOBr$ *	-15.04	-16.91
$HOHgOBr + CH_3OH \rightarrow Hg(OH)_2 + CH_3OBr$ *	-14.26	-16.42
$HOHgOBr + HBr \rightarrow BrHgOH + HOBr$	-15.10	-17.07
AVG/STDEV	**-14.8 +/- 0.47**	**-16.8 +/- 0.34**

[a] This reaction is not included in the calculations of the average value.

In order to reduce the accumulation of error from our calculations we varied the species in the work reactions as much as possible. Considering the same example, ΔH^0_f for HOHgOCl can also be calculated using BrHgOH and $Hg(OH)_2$ as one of the reference species in the work reaction. Since standard error for ΔH^0_f HOHgOCl averaged over all the work reactions is 0.13 kcal/mol (see Table 3.4) then the values of ΔH^0_f for BrHgOH and $Hg(OH)_2$ should also be accurate. If either of BrHgOH or $Hg(OH)_2$ had a significant error in their ΔH^0_f values, then the standard deviation for HOHgOCl would increase. A parametric study where the standard errors of the GOM species are reduced by iterating across the work reactions increasing the precision could in practice be done but is outside the current scope of this work.

With the different ΔH^0_f work reaction schemes established, we proceed to analyze their accuracy relative to reference values and assess the computational methodology. Figure 3.1 shows the deviations of ΔH^0_f from experimental and high-level computational reference data.

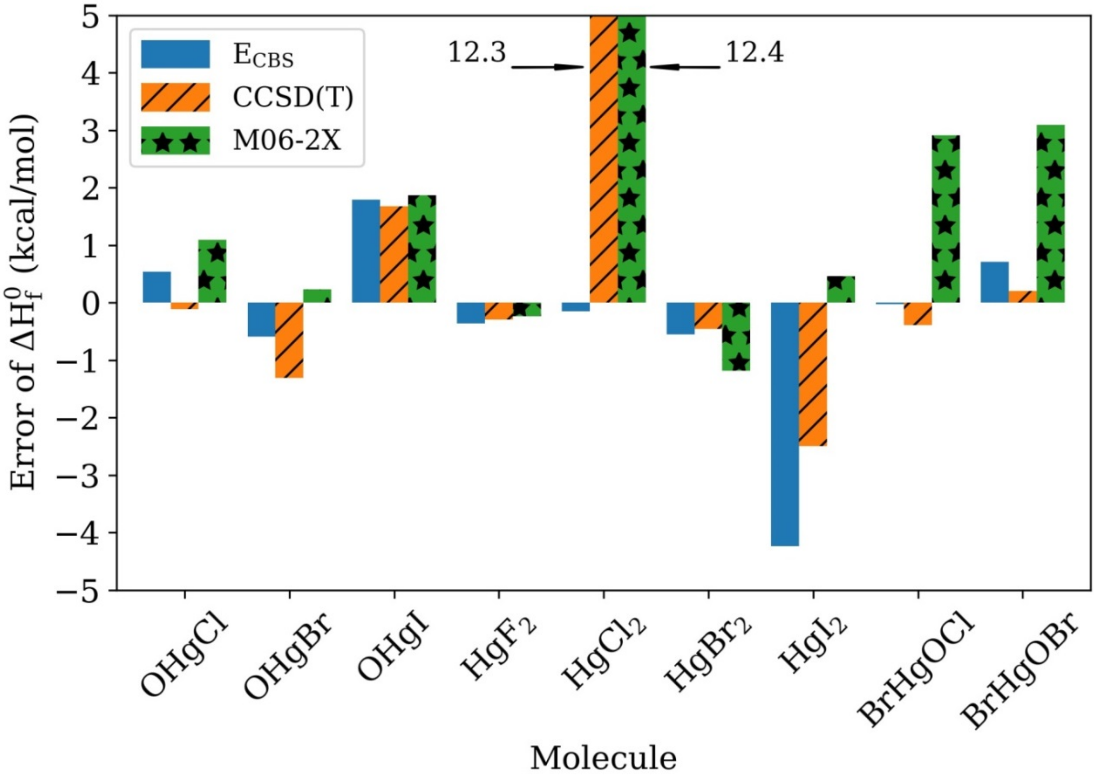

Figure 3.1 Deviation of standard enthalpies of formation from literature reference values calculated using isodesmic and isogyric work reactions across multiple methods.

The deviation for OHgCl[69], OHgBr[69] and OHgI[68] was calculated using the values of the group of Peterson as the reference. Their calculations involved using correlation consistent AVnZ (n = 3 or T, 4 or Q, and 5) basis sets, including a small core energy consistent relativistic ECP for Br and Hg, and an extrapolation to the CBS limit averaging energies from 3-point mixed Gaussian-exponential formula[50, 74] (n = 3, 4, 5) and from a 2-point extrapolation formula [75, 76] (n = 4, 5). Note, at the time of Peterson's calculations for OHgCl and OHgBr the Stuttgart/Köln ECP was not yet available for Hg. Instead, the ECP used was that of Häussermann et al.[77] which is a quasi-relativistic ECP derived from two component MCDHF calculations. For OHgI, the Stuttgart/Köln PP was used. In our calculations, the largest basis set used is AVQZ.

Peterson's calculations for open-shell molecules were performed using restricted open shell Hartree-Fock (HF) calculations but unrestricted open-shell calculations for the coupled cluster part (ROHF/UCCSD(T)). In our calculations, we used unrestricted open shell calculations for the HF and CCSD(T) parts. The frozen-core approximation was used in both Peterson's and our calculations. Peterson determined the equilibrium geometry from a potential energy surface of the molecules generated from numerous single point calculations in the vicinity of an approximate equilibrium geometry[78]. A polynomial function was then fit to the calculated energies and the equilibrium geometry determined. In addition, their calculations included additive corrections to the E_{CBS} energy accounting for core-valence correlation (ΔE_{CV}), scalar relativist effects (ΔE_{SR}), spin-orbit coupling corrections (ΔE_{SO}), and the Lamb shift (ΔE_{Lamb}). In our calculations, we do not explicitly account for these corrections, but rather use the isodesmic / isogyric reactions as the method of error cancellation.

For HgF_2, $HgCl_2$, $HgBr_2$, and HgI_2 data from the Chase et. al. monograph[19] is used for the reference values. Data in Table 3.5 is intended to demonstrate the internal consistency in our calculations. It compares enthalpy data from the literature on ΔH^0_f for the HgX_2 species with the error balancing work reactions. These work reactions only use our calculated ΔH^0_f for the mercury molecules used as the reference species. The ΔH^0_f data for HgF_2, $HgCl_2$, and $HgBr_2$ calculated from these work reactions using the $E_{CBS}(2,3,4)$ methodology are in excellent agreement with the experimental reference values. The exemption is HgI_2, where results from the M06-2X method is in closer agreement to reference values.

Table 3.5 Heats of Formation at 298K for HgF_2, $HgCl_2$, $HgBr_2$, and HgI_2 Averaged over Multiple Work Reactions. Isodesmic Reactions are Marked with an Asterisk *. E_{CBS}(2,3,4) Values are Recommended

Work Reaction	**M06-2X/ AVTZ**	**E_{CBS}(2,3,4)**
	ΔH_F (298K) (kcal/mol)	
$HgF_2 + HOHgOCl \rightarrow FHgOCl + FHgOH$ *	-68.87	-68.94
$HgF_2 + HOHgOBr \rightarrow FHgOBr + FHgOH$ *	-72.33	-72.48
$HgF_2 + Hg(OH)_2 \rightarrow FHgOH + FHgOH$ *	-70.05	-70.21
Literature value, -70.18 [77]		
AVG/STD	**-70/42 +/- 1.76**	**-70.54 +/- 1.79**
$HgCl_2 + HOHgOCl \rightarrow ClHgOCl + ClHgOH$ *	-25.77	-35.09
$HgCl_2 + HOHgOBr \rightarrow ClHgOBr + ClHgOH$ *	-25.68	-35.08
$HgCl_2 + Hg(OH)_2 \rightarrow ClHgOH + ClHgOH$ *	-16.21	-35.15
Literature value, -34.96 [78]		
AVG/STD	**-22.56 +/- 5.49**	**-35.11 +/- 0.04**
$HgBr_2 + HOHgOCl \rightarrow BrHgOCl + BrHgOH$ *	-21.56	-20.87
$HgBr_2 + HOHgOBr \rightarrow BrHgOBr + BrHgOH$ *	-21.6	-20.89
$HgBr_2 + Hg(OH)_2 \rightarrow BrHgOH + BrHgOH$ *	-21.64	-21.16
Literature value, -20.42 [19]		
AVG/STD	**-21.60 +/- 0.04**	**-20.97 +/- 0.16**
$HgI_2 + HOHgOCl \rightarrow IHgOCl + IHgOH$ *	-4.72	-9.33
$HgI_2 + HOHgOBr \rightarrow IHgOBr + IHgOH$ *	-3.93	-8.53
$HgI_2 + Hg(OH)_2 \rightarrow IHgOH + IHgOH$ *	-1.54	-6.45
Literature value, -3.86 [19]		
AVG/STD	**-3.40 +/- 1.66**	**-8.10 +/- 1.49**

Accurate thermochemistry for BrHgOCl and BrHgOBr was calculated by Jiao and Dibble[59] using a similar methodology and basis sets to that of Peterson[68, 69] but with significant deviations in the geometry optimization and SO calculations and without any ΔE_{Lamb} corrections. The geometry optimization was done with CCSD(T)/VTZ, CCSD(T)/AVTZ, CCSD(T)/AVQZ calculations using an algorithm for CCSD(T) analytical gradients[79]. ΔE_{SO} corrections were calculated using the restricted active space state interaction (RASSI) method with complete active space second-order perturbation theory (CASPT2). ΔE_{SO} was calculated as the difference between the lowest spin−orbit state RASSI/CASPT2 and the lowest spin-free state RASSI/CASPT2. By not including any ΔE_{Lamb} corrections, the calculated bond energies can be too large by 0.4 to 0.8 kcal/mol[59].

The *ab initio* calculations of Peterson and Dibble are state of the art with any limitations on the computations likely due to the limits of the computational resources. Compared to the extrapolated CBS energy ($E_{CBS}(3,4,5)$) the combined contributions to the bond energy from the additional corrections are comparatively small, at most decreasing the bond energy by 4.5 kcal/mol or 8-13%[59, 68, 69]. The largest corrections are for the Hg-I species which contain the heaviest atoms studied and should have the largest spin-orbit coupling effects. In theory these calculations can potentially be improved upon by systematically increasing the computational rigor. For example, for the ΔE_{SR} corrections a higher nth order DKn (n = 2, 3, …) Hamiltonian[80] can be used which systematically lowers the energy. Jiao and Dibble showed that the difference of the ΔE_{SR} correction calculated using a DK3 versus a DK2 Hamiltonian is at most an increase of 0.1 kcal/mol. It is unlikely that using a higher order DK Hamiltonian will drastically change the results. From a practical computational perspective, Peterson's and Dibble's calculation can be considered the current state of the art. Highlighting these details, we now access the accuracy of our work reaction approach.

Comparing across the $E_{CBS}(2,3,4)$, CCSD(T)/AVTZ//M06-2X/AVTZ, and the M06-2X/AVTZ methods used in this study, $E_{CBS}(2,3,4)$ is on average the best performing of these three methods. The calculated $E_{CBS}(2,3,4)$ values are in excellent agreement with deviations less than 1 kcal/mol from the reference values for OHgCl, OHgBr, HgF_2, $HgCl_2$, $HgBr_2$, BrHgOCl, and BrHgOBr. The $E_{CBS}(2,3,4)$ calculations deviate from the reference values by 1.8 and 4.2 kcal/mol, respectively for OHgI and HgI_2.

The single point CCSD(T)/AVTZ calculations generally perform well, however, for OHgI, $HgCl_2$, and HgI_2 the errors are larger than 1 kcal/mol (2, 12.4, -2.4 kcal/mol, respectively). The M06-2X/AVTZ calculations also offer good performance, especially for the low computational cost, however, for OHgI, $HgCl_2$, BrHgOCl and BrHgOBr the errors are significantly over 1 kcal/mol (1.9, 12.4, 2.9, and 3.1 kcal/mol, respectively. The stark deviation for $HgCl_2$ is quite surprising in both of these methods. As the atoms in the GOM species get heavier, we would expect a slight increase in the error. Cl is among the lighter of the halogens, so the poor performance with $HgCl_2$ calculations was unexpected. It seems that the $E_{CBS}(2,3,4)$ methodology converges the calculations since for the same work reactions for $HgCl_2$ the error is only 0.14 kcal/mol. In a few cases, the single point CCSD(T)/AVTZ energies and M06-2X/AVTZ perform better than $E_{CBS}(2,3,4)$ as is the case for OHgCl and HgI_2. We cannot explain why in these cases the performance of $E_{CBS}(2,3,4)$ is the lowest of the three. Overall, we recommend using the $E_{CBS}(2,3,4)$ extrapolation methodology for determining the thermochemistry since it systematically converges towards a value. Utilizing this computation methodology, we can now evaluate the performance of each of the work reactions.

Table 3.6 Heats of Formation for OHgF, OHgCl, OHgBr, and OHgI Averaged over Multiple Work Reactions. Isodesmic Reactions are Marked with an Asterisk *. Work Reactions Using only Literature Reference Values are Highlighted with a Dagger †. E_{CBS}(2,3,4) Values are Recommended

Work Reaction	**M06-2X/AVTZ**	**E_{CBS}(2,3,4)**
	ΔH_F (298K) (kcal/mol)	
OHgF → O + Hg + F **(ARM-2[a])**	-0.54	-2.48
OHgF + HF → HgF_2 + OH [a, †]	1.71	-0.09
OHgF + H_2 → HF + HgOH	-4.21	-4.02
OHgF + HgI → OHgI + HgF*, †	-3.03	-3.09
OHgF + HgCl → OHgCl + HgF *, †	-2.83	-2.90
OHgF + HgBr → OHgBr + HgF *, †	-3.01	-2.85
AVG/STDEV	**-3.24 +/- 0.56**	**-3.18 +/- 0.48**
OHgCl → O + Hg + Cl **(ARM-2[a])**	18.36	17.80
OHgCl + HCl → $HgCl_2$ + OH †	17.33	18.01
OHgCl + H_2 → HCl + HgOH	18.81	17.03
Ref. value, OHgCl, ΔH_F°= 16.8[b]		
AVG/STDEV	**18.07 +/- 1.05**	**17.52 +/- 0.69**
OHgBr → O + Hg + Br **(ARM-2[a])**	26.76	21.03
OHgBr + HBr → $HgBr_2$ + OH †	26.85	26.23
OHgBr + H_2 → HBr + HgOH	25.88	24.87
Ref. value, OHgBr, ΔH_F°= 26.14[b]		
AVG/STDEV	**26.37 +/- 0.69**	**25.55 +/- 0.96**
OHgI → O + Hg + I **(ARM-2[a])**	36.14	26.76
OHgI + HI → HgI_2 + OH †	33.03	32.74
OHgI + H_2 → HI + HgOH	34.54	34.16
OHgI + HgF → OHgF + HgI *	34.37	34.43
OHgI + HgCl → OHgCl + HgI *, †	34.76	34.75
OHgI + HgBr → OHgBr + HgI *, †	34.59	34.80
Ref. value, OHgI, ΔH_F°= 32.39[c]		
AVG/STDEV	**34.26 +/- 0.70**	**34.18 +/- 0.84**

[a] This reaction is not included in calculation of the average value. [b] Values adapted from Balabanov and Peterson, ΔH^0_f converted from 0 K to 298K [69]. [c] Value adapted from Shepler et al. value shown is at 298K [68].

Table 3.6 shows the heats of formation for OHgF, OHgCl, OHgBr, and OHgI calculated from each of the work reactions at the M06-2X/AVTZ and E_{CBS}(2,3,4) levels of theory .

Two isogyric work reactions are used for OHgCl and OHgBr. We varied the non-target species radical in these isogyric work reactions (OH and HgOH). The isogyric work for OHgCl reaction with HgOH is within 0.23 kcal/mol of the reference value, whereas for OHgBr, the reaction with OH is within 0.09 kcal/mol. Although there is some small difference, both isogyric work reactions are in excellent agreement with the reference values, within chemical accuracy of 1 kcal/mol.

A combination of isogyric and isodesmic work reactions are used for OHgI. The isogyric reaction with OH is the closest to the reference value, being within 0.35 kcal/mol for OHgI. The reference values used for OHgF, OHgCl, and OHgBr were those calculated in this study for the OHgI isodesmic reactions. Comparing the heat of formation from the isogyric reaction with OH to the isodesmic reactions with HgI, the isogyric reaction with HgI_2 is between 1.3 to 2 kcal/mol lower in energy from the M06-2X/AVTZ and E_{CBS}(2,3,4) calculations, respectively. From evaluation of the reference species used in the OHgI reaction set, it could be possible that the reference for HgI_2 is 1 kcal/mol too low. Using a reference value of -2.86 kcal/mol (instead of -3.86 kcal/mol) shifts the ΔH^0_f of OHgI calculated from $OHgI + HI \rightarrow HgI_2 + OH$ to -33.74 (for E_{CBS}(2,3,4)), which in within chemical accuracy (1 kcal/mol) of the isodesmic reactions. HgI_2 is used as a reference species for IHgOH (see Table 8) and by using -2.86 kcal/mol as the reference, the standard deviation of the work reactions for IHgOH is lowered to

0.94 from 1.5 kcal/mol. Again, a parametric study optimizing the precision of the calculated $\Delta H^0{}_f$ is not the direct goal of this work. We highlight that work reactions could potentially be used as tool to check the accuracy of computational or experimental $\Delta H^0{}_f$ data. Note, in work reactions where HgI_2 was used, we kept -3.86 kcal/mol as the reference value.

A combination of isodesmic and isogyric work reactions was used for the work reactions on BrHgOCl and BrHgOBr, as shown in Tables 9 and 10, our calculated $\Delta H^0{}_f$ is within 0.03 and 0.79 kcal/mol of the reference value for BrHgOCl and BrHgOBr respectively the best reaction is the isodesmic reaction. For BrHgOCl is: BrHgOCl + H_2O → HOHgBr + HOCl which is within 0.08 kcal/mol of the reference value. The best work reaction for BrHgOBr is the isodesmic reaction BrHgOBr + H_2O → HOHgBr + HOBr which is within 0.39 kcal/mol reference value. Considering that BrHgOCl and BrHgOCl are among the largest species calculated in this study, the excellent agreement with the literature values from highly correlated *ab initio* calculations highlights the effectiveness of our work reaction approach.

We also used an atomization[80] reaction method (ARM-2) in addition to the isodesmic and isogyric work reaction schemes. Figure 3.2 shows the deviation of $\Delta H^0{}_f$ from reference values using ARM-2.

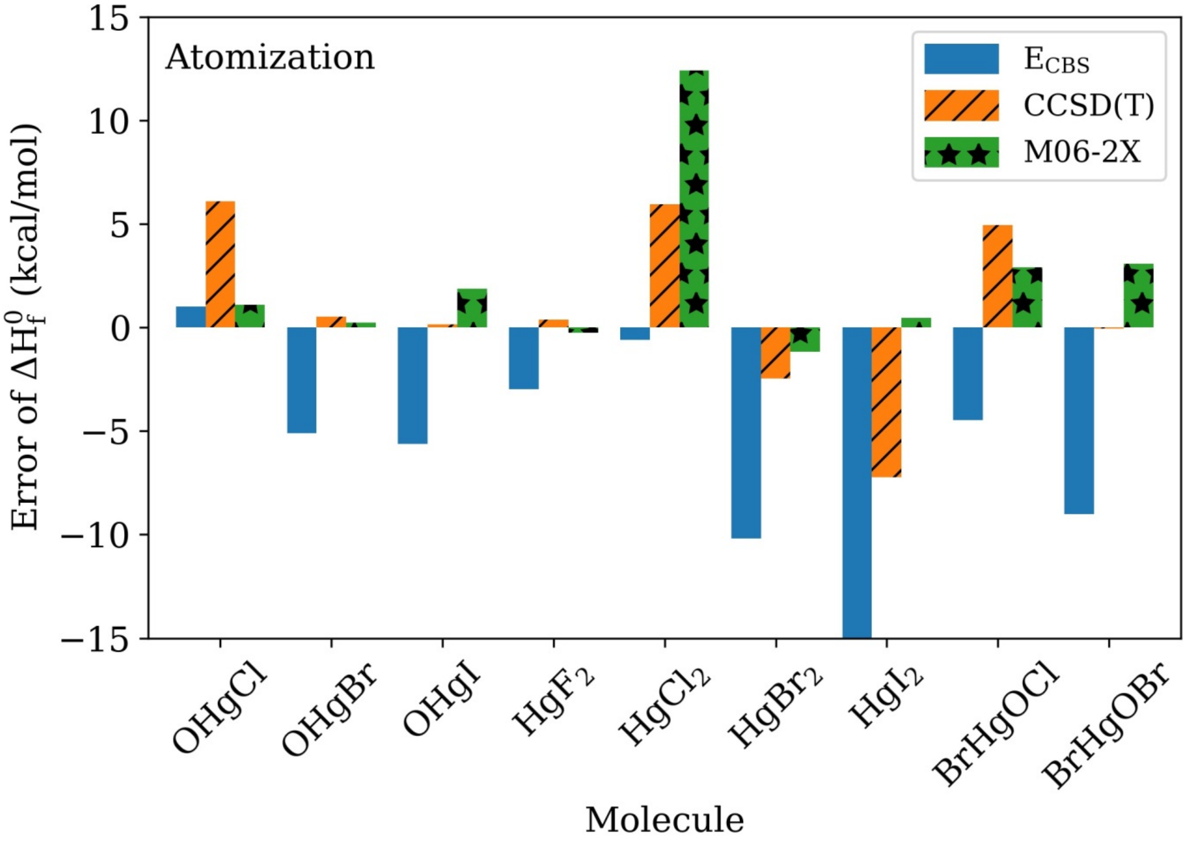

Figure 3.2 Deviation of standard enthalpies of formation from reference values calculated using atomization work reactions across the three methods.

Although atomization reactions have some cancellation of error (e.g., spin-orbit coupling in X–Hg–Y bonds could be cancelled by that from X• and Y•) the calculation errors are significantly more dependent on the computational method. The poor performance of the ARM-2 method for Hg species with Br and I atoms could be a result of the non cancellation of error in the atomization reactions, as there is less cancelation of error, compared to isodesmic or isogyric reactions. The accuracy is expected to decrease as the constituent atoms in the GOM species increase in size. An interesting observation is that for the atomization reactions, the $E_{CBS}(2,3,4)$ methodology for ARM-2 on average performs worse than single point CCSD(T) and M06-2X calculations. For GOM species with Hg as the only heavy atom, atomization reactions have potential as an inexpensive method for estimation of the thermochemical properties.

We note that isogyric and isodesmic work reactions are highly dependent on the accuracy of the reference specie heats of formation. Any errors associated with the reference species from the literature could also contribute to the ΔH^0_f error calculated from the work reactions. With the work reaction templates established, as the reference values improve over time then so will our calculations. The use of isodesmic or isogyric reactions is nonetheless an excellent tool to more rapidly identify thermochemical properties over a wide range of species, assuming access to accurate thermochemical data for the reference species is available.

The final analysis done on our isodesmic and isogyric reaction methodology was an assessment of the computational cost. The largest basis set used in our calculations was the AVQZ. The work of Peterson and Dibble used the AV5Z basis sets as the largest type. If we assume that the CCSD(T)/AVnZ single point calculations as the most expensive part, then we can compare across calculations. Table 7 shows the number of basis functions (N_{basis}) for select species and a ratio of the AV5Z/AVQZ computational cost.

Table 3.7 Basis Functions for Select Species and Relative CCSD(T) CPU Cost

Molecule	**Number of Basis Functions**			**Relative CPU Cost**
	AVTZ	AVQZ	AV5Z	AV5Z/AVQZ
OHgCl	189	307	463	17.7
OHgBr	184	299	455	18.9
OHgI	189	304	460	18.2
HgF_2	180	295	451	19.5
$HgCl_2$	188	303	459	18.3
$HgBr_2$	198	313	469	17.0
HgI_2	198	319	475	16.2
BrHgOCl	239	388	591	19.0
BrHgOBr	244	393	596	18.4

CCSD(T) calculations scale as N_{basis} to the seventh power, (N_{basis}^7). The ratio of N_{AV5Z}^7/N_{AVQZ}^7 thus represents the increase in computational cost in going from the AVQZ to the AV5Z basis set. As seen in Table 3.7, this amounts to an increase of slightly less than a factor of 20. Although we calculate energies for a significant number of added molecules in the work reaction analysis (e.g., one calculation for each species in the reaction), the most expensive calculations are for the GOM species. References species in the work reactions, can also be re-used for other GOM molecule calculations, and some CPU time is saved as our reference species database grows. We also do not include additional corrections to the $E_{CBS}(2,3,4)$ energies so some CPU time can also be saved here. DFT methods would represent a significant lower cost alternative in place of the CCSD(T) calculations since they scale as N_{basis}^3 or N_{basis}^4. The problem with use of DFT methods is finding the right functional that works for the GOM molecules and the other species in the work reaction.

3.3.2 Thermodynamics of Hg Species from Isodesmic and Isogyric Work Reactions

With the accuracy of our work reaction scheme established, we discuss the thermodynamics of the OHgX, XHgOH, XHgOCl, and XHgOBr (where X = Halogen) molecules calculated in this study. Figure 3.3a shows the ΔH^0_f for these GOM species from the $E_{CBS}(2,3,4)$ calculations. We also include ΔH^0_f for HgX_2 from experimental data as a basis for comparison. For GOM species where computational data is available (e.g., the non HgX_2 species shown in Figure 1) we show the results of our calculations where replicates were done. The results are presented by increase in the halogen atomic number and by use of OH, OCl, and OBr.

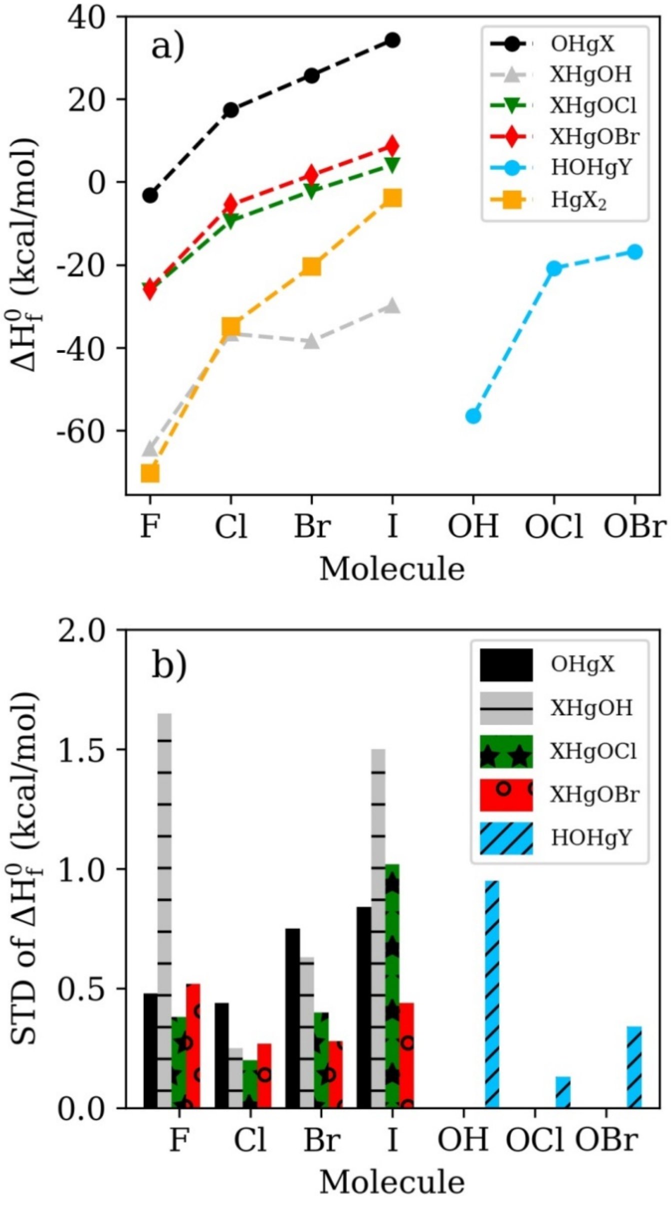

Figure 3.3 (a) Standard enthalpies of formation, GOM species calculated from $E_{CBS}(2,3,4)$ and work reactions; (b) Standard Deviation (σ) of ΔH^0_f calculated over multiple work reactions. X = Halogen, Y = OH, OCl, or OBr.

The reference HgX_2 enthalpy data follow a monotonically increasing trend with decreasing electronegativity of the halogen. The enthalpy data of the OHgX, XHgOH, XHgOCl, and XHgOBr also tend to follow monotonically increasing trend with decreasing electronegativity of the halogen. A slight divergence of this trend is observed for XHgOH, where ΔH^0_f is close to 2 kcal/mol higher for ClHgOH than for BrHgOH. The standard deviation (STD) of ΔH^0_f averaging over the work reactions is shown in Figure 3b, where the error in ΔH^0_f is less than 1 kcal/mol except for FHgOH and IHgOH, where the STD is 1.65 and 1.5 kcal/mol, respectively.

Calculated enthalpies of formation from the work reactions for OHgF (Table 4 above) are in general agreement with the exception of one reaction: $OHgF + HF \rightarrow HgF_2 + OH$, which is 3 kcal/mol higher than the calculated average. A plausible reason the enthalpy from this isogyric reaction is significantly different from the other reactions of OHgF, is that the OH product bonding does not reflect similar bonding to the O–Hg bonding in the OHgF reactant. We note that the other reference species with hydrogen bonds (HF, HgF_2, and OH) are used elsewhere show good agreement in calculations from other work reactions used for molecules such as HOHgF and FHgOBr. The work reaction $OHgF + HF \rightarrow HgF_2 + OH$ was therefore not included in the calculation of the average heat of formation of OHgF. It is interesting to note that for OHgCl, OHgBr, and OHgI using a template reaction of the same type ($OHgX + HX \rightarrow HgX_2 + OH$) gives ΔH^0_f that are close to the data from Peterson[68, 69] and co-workers. For these molecules, the $OHgX + HX \rightarrow HgX_2 + OH$ work reaction is included in the average value of ΔH^0_f from the work reactions.

Table 3.8 Heats of Formation for HOHgY (Y = F, Cl, Br, and I) Averaged over Multiple Work Reactions. Isodesmic Reactions are Marked with an Asterisk *. Work Reactions Using only Literature Reference Values are Highlighted with a Dagger †. E_{CBS}(2,3,4) Values are Recommended

Work Reaction	**M06-2X/ AVTZ**	**E_{CBS}(2,3,4)**
	ΔH_F (298K) (kcal/mol)	
$FHgOH \rightarrow H + O + Hg + F$ **(ARM-2[a])**	-61.40	-65.40
$FHgOH + HF \rightarrow HgF_2 + H_2O$ †	-61.47	-62.92
$FHgOH + CH_3F \rightarrow HgF_2 + CH_3OH$ †	-62.05	-63.26
$FHgOH + CH_2Cl_2 \rightarrow HgCl_2 + CH_2FOH$ †	-63.05	-64.84
$FHgOH + OH \rightarrow OHgF + H_2O$ *	-66.86	-66.51
AVG/STDEV	**-63.36 +/- 2.43**	**-64.38 +/- 1.65**
$ClHgOH \rightarrow H + O + Hg + Cl$ **(ARM-2[a])**	-42.72	-36.21
$ClHgOH + HCl \rightarrow HgCl_2 + H_2O$ †	-46.57	-36.41
$ClHgOH + CH_3Cl \rightarrow HgCl_2 + CH_3OH$ †	-44.98	-36.55
$ClHgOH + OH \rightarrow OHgCl + H_2O$ *,†	-46.38	-36.90
$ClHgOH + CH_3OBr \rightarrow ClHgOBr + CH_3OH$ *,	-48.15	-36.44
$ClHgOH + CH_3OCl \rightarrow ClHgOCl + CH_3OH$ *,	-47.59	-36.24
AVG/STDEV	**-46.74 +/- 1.22**	**-36.51 +/- 0.25**
$BrHgOH \rightarrow H + O + Hg + Br$ **(ARM-2[a])**	-34.55	-42.69
$BrHgOH + HBr \rightarrow HgBr_2 + H_2O$ †	-37.31	-37.90
$BrHgOH + OH \rightarrow OHgBr + H_2O$ *,†	-38.62	-38.58
$BrHgOH + CH_3OCl \rightarrow BrHgOCl + CH_3OH$ *	-39.91	-37.97
$BrHgOH + CH_3OBr \rightarrow BrHgOBr + CH_3OH$ *	-39.43	-39.24
AVG/STDEV	**-38.82 +/- 1.14**	**-38.42+/- 0.63**
$IHgOH \rightarrow H + O + Hg + I$ **(ARM-2[a])**	-24.95	-36.76
$IHgOH + HI \rightarrow HgI_2 + H_2O$ †	-30.52	-30.83
$IHgOH + H_2O \rightarrow Hg(OH)_2 + HI$	-28.90	-28.22
$IHgOH + OH \rightarrow OHgI + H_2O$ *,†	-28.87	-28.89
$IHgOH + CH_3I \rightarrow HgI_2 + CH_3OH$		-31.33
AVG/STDEV	**-29.43 +/- 0.95**	**-29.82 +/- 1.5**

[a] Reaction is not included in the calculations of the average value.

Details of the work reactions for the XHgOH species, are given in Table 6. For FHgOH the work reaction FHgOH + OH → OHgF + H_2O deviates by 2.13 kcal/mol from the average ΔH^0_f value. Although this work reaction is isodesmic, this reaction deviates the most from those for FHgOH.

A similar explanation as above – the calculation of OH bonding in HOHgF is significantly different than the calculated OH bonding in H_2O. Hence, the error associated with the •O–H compared to the HO–HgF bond from the computational method is not well cancelled in the reaction calculation. The same reaction template for ClHgOH and BrHgOH is, however, in much better agreement with the average ΔH^0_f calculated from the work reaction. Since Cl and Br are not as electronegative as F, then the polarity differences in OHgCl, OHgBr, and OH are not are as different and the work reaction cancels out the error better.

The isodesmic work reaction ClHgOH + CH_3OBr → ClHgOCl + CH_3OH for ClHgOH uses ClHgOCl as one of the references species in one of the five work reactions. In our work reaction scheme ClHgOCl is calculated using ΔH^0_f for ClHgOH in several of the work reactions (Table 3.8), in what could be considered a circular reasoning problem. Since the ΔH^0_f calculated from ClHgOH + CH_3OBr → ClHgOCl + CH_3OH is in excellent agreement with work reactions without ClHgOCl, including work reactions with only experimental reference values, we conclude that our calculated ΔH^0_f for ClHgOCl should be accurate.

Similar logic applies to BrHgOH and ClHgOBr where these species are partially interdependent. As another accuracy test for our calculations, in the isodesmic work reaction BrHgOH + CH_3OBr → BrHgOBr + CH_3OH the reference value for BrHgOBr used was from the calculations of Dibble[61]. If we use our calculated value for BrHgOBr in the same work reaction, we calculate a ΔH^0_f of -38.53 kcal/mol, which is in very good agreement with the results from the other work reactions for BrHgOH.

Detailed results from the work reactions for XHgOCl, XHgOBr, $Hg(OH)_2$, and HOHgOCl, HOHgOBr (X = halogen) are presented across Tables 3.9, 3.10, and 3.4. Combinations of isodesmic and isogyric work reactions are used for the species above. Some of these molecules are used as references species in our calculated values for FHgOH, ClHgOH, and BrHgOH. Calculated ΔH^0_f averaged across the work reactions for a particular species are in very good agreement with each other with standard deviations of less than 1 kcal/mol.

Table 3.9 Heats of Formation at 298K for XHgOCl (X = F, Br, Cl; and I) Averaged over Multiple Work Reactions. Isodesmic Reactions are Marked with an Asterisk *. Work Reactions Using only Literature Reference Values are Highlighted with a Dagger †. E_{CBS}(2,3,4) Values are Recommended

Work Reaction		**M06-2X/ AVTZ**	**E_{CBS}(2,3,4)**
		ΔH_F (298K) (kcal/mol)	
FHgOCl → F + Hg + O + Cl	**(ARM-2[a])**	-25.74	-28.36
FHgOCl + HF → HgF_2 + HOCl †		-21.35	-25.82
FHgOCl + H_2O → FHgOH + HOCl *		-23.54	-26.57
	AVG/STDEV	**-22.44 +/- 1.55**	**-26.20 +/- 0.53**
ClHgOCl → 2Cl + Hg + O	**(ARM-2[a])**	-7.48	-9.13
ClHgOCl + HCl → $HgCl_2$ + HOCl †		-6.88	-9.27
ClHgOCl + H_2O → ClHgOH + HOCl *		3.23	-9.34
ClHgOCl + CH_3OH → ClHgOH + CH_3OCl *		1.70	-9.65
	AVG/STDEV	**-0.65 +/- 5.45**	**-9.42 +/- 0.2**
BrHgOCl → Br + Hg + O + Cl	**(ARM-2[a])**	0.22	-6.66
BrHgOCl + HBr → $HgBr_2$ + HOCl †		1.92	-1.81
BrHgOCl + H_2O → BrHgOH + HOCl *		0.86	-2.28
BrHgOCl + CH_3OH → BrHgOH + CH_3OCl *		-0.66	-2.60
Literature value, BrHgOCl, $\Delta H_F°$ = -2.2[b]			
	AVG/STDEV	**0.71 +/- 1.3**	**-2.23 +/- 0.4**
IHgOCl → I + Hg + O + Cl	**(ARM-2[a])**	9.44	-1.22
IHgOCl + HI → HgI_2 + HOCl †		8.32	4.78
IHgOCl + H_2O → IHgOH + HOCl *		9.88	3.33
	AVG/STDEV	**8.95 +/- 0.89**	**3.90 +/- 1.42**

[a] Reaction is not included in the calculations of the average value. [b] From Jiao and Dibble, value at 298K[59].

Table 3.10 Heats of Formation at 298K for XHgOBr (X = F, Br, Cl; and I) Averaged over Multiple Work Reactions. Isodesmic Reactions are Marked with an Asterisk *. Work Reactions Using only Literature Reference Values are Highlighted with a Dagger †. $E_{CBS}(2,3,4)$ Values are Recommended

Work Reaction	**M06-2X/ AVTZ**	**$E_{CBS}(2,3,4)$**
	ΔH_F (298K) (kcal/mol)	
$\mathrm{FHgOBr \rightarrow F + Hg + O + Br}$ **(ARM-2[a])**	-20.18	-29.78
$\mathrm{FHgOBr + HF \rightarrow HgF_2 + HOBr}^{\dagger}$	-23.11	-26.44
$\mathrm{FHgOBr + H_2O \rightarrow FHgOH + HOBr}$ *	-23.64	-25.52
$\mathrm{FHgOBr + HBr \rightarrow FHgBr + HOBr}$	-23.65	-25.57
AVG/STDEV	**-23.46 +/- 0.31**	**-25.84 +/- 0.52**
$\mathrm{ClHgOBr \rightarrow Cl + Hg + O + Br}$ **(ARM-2[a])**	-1.93	-10.57
$\mathrm{ClHgOBr + HCl \rightarrow HgCl_2 + HOBr}^{\dagger}$	-4.43	-5.68
$\mathrm{ClHgOBr + H_2O \rightarrow ClHgOH + HOBr}$ *	5.67	-5.74
$\mathrm{ClHgOBr + CH_3OH \rightarrow ClHgOH + CH_3OBr}$ *	6.45	-5.26
AVG/STDEV	**2.56 +/- 6.07**	**-5.56 +/- 0.27**
$\mathrm{BrHgOBr \rightarrow 2Br + Hg + O}$ **(ARM-2[a])**	5.84	-8.11
$\mathrm{BrHgOBr + HBr \rightarrow HgBr_2 + HOBr}^{\dagger}$	4.44	1.76
$\mathrm{BrHgOBr + H_2O \rightarrow BrHgOH + HOBr}$ *	3.38	1.29
$\mathrm{BrHgOBr + CH_3OH \rightarrow BrHgOH + CH_3OBr}$ *	4.16	1.77
Literature value, BrHgOBr, ΔH_F°= 0.9[b]		
AVG/STDEV	**3.99 +/- 0.55**	**1.61 +/- 0.28**
$\mathrm{IHgOBr \rightarrow I + Hg + O + Br}$ **(ARM-2[a])**	15.06	-2.66
$\mathrm{IHgOBr + HI \rightarrow HgI_2 + HOBr}^{\dagger}$	10.83	8.36
$\mathrm{IHgOBr + H_2O \rightarrow IHgOH + HOBr}$	11.15	8.97
AVG/STDEV	**10.99 +/- 0.22**	**8.66 +/- 0.44**

[a] Reaction is not included in the calculations of the average value. [b] From Jiao and Dibble, value at 298K [59].

A metric of the accuracy of our calculations can be assessed by the good agreement between the work reactions using our calculated species as reference values and work reactions using only literature values as references. In addition, by significantly varying the reference species used, such as by mixing Carbon and Hg species across multiple work reactions, we can further assess the accuracy of our calculations. If two distinct work reactions yield heats of formation for the target Hg-species within chemical accuracy (1 kcal/mol) of each other, suggests that the values are accurate.

3.3.3 Thermodynamics of Hg Species from Atomization Reactions ARM-2

Figure 3.4 shows the error of the ΔH^0_f calculated using ARM-2 relative to the $E_{CBS}(2,3,4)$ calculations using isodesmic and isogyric work reactions. The difference between ARM-2 and $E_{CBS}(2,3,4)$ for OHgF, OHgCl, FHgOH, ClHgOH, $Hg(OH)_2$, HOHgOCl, FHgOCl, and ClHgOCl is within 1 kcal/mol or less. Noting that there is no attempt in error cancelation in the ARM-2 methodology, the ARM-2 results for these species are in excellent agreement.

There is a second set of mercury species, where the difference between ARM-2 and $E_{CBS}(2,3,4)$ from the work reactions is upwards of 5 kcal/mol. These involve a Br, I atoms or an OBr group: OHgBr, OHgI, BrHgOH, IHgOH, HOHgOBr, FHgOBr, ClHgOBr, IHgOBr, BrHgOCl, and IHgOCl The largest disagreement is observed for IHgOBr where the difference is 11.3 kcal/mol. It is possible that the disagreement between ARM-2 and $E_{CBS}(2,3,4)$ from the work reaction schemes is either a larger spin-orbit coupling interaction due to the extended bonding of the outer orbitals (i.e., Br and I) or the use of more than one ECP.

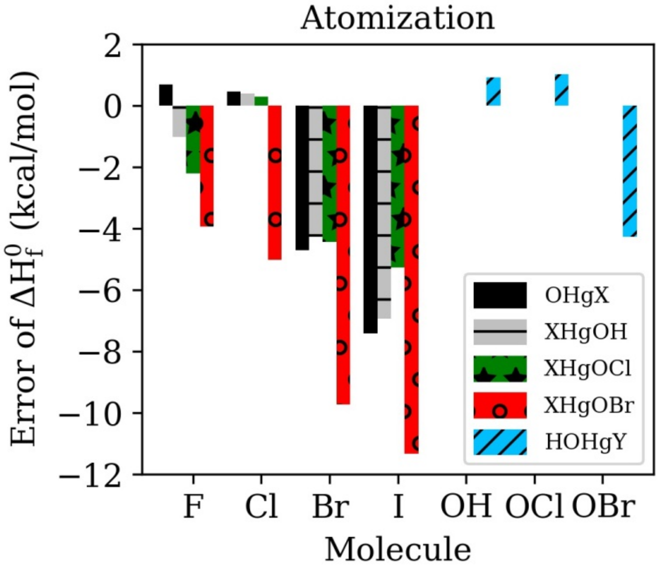

Figure 3.4 Deviation of ΔH^0_f calculated from atomization reactions (ARM-2) relative to the values from E_{CBS}(2,3,4) calculations.

The Stuttgart/Köln ECP was used and derived with a similar methodology to the Hg ECP for both Br and I atoms. Although the ECP does include some relativistic effects, as noted earlier, several added corrections are still recommended. The net difference between ARM-2 and the work reactions is, however, still larger than the net contributions of the extra corrections. The OHgBr scalar relativistic, core-valence and ECP corrections, for example, have a cumulative effect of decreasing the CBS energy by -1.18 kcal/mol[69]. In our calculations the difference between ARM-2 and the work reactions is 4.7 kcal/mol. If we assume a 1.18 kcal/mol improvement due to the corrections, then there are ~3 kcal/mol that are still unaccounted for. The cumulative effect is -1.55 kcal/mol[69] for OHgCl and the difference between ARM-2 and the work reactions is 0.04 kcal/mol. The cumulative effect is -1.12 kcal/mol for OHgI, where the difference between our schemes is 7.8 kcal/mol. It is noted that differences in the zero-point energy calculations are not accounted for; but even if we assume a 1 kcal/mol error here, there is still a significant energy difference between ARM-2 and the work reactions for molecules where more than one ECP is used. We are not implying that the use of ECP is erroneous. ECP have been used in Hg thermodynamic calculations and clearly give accurate results for Hg species[31, 59, 64, 68, 69]. At the time it is unclear why this difference exists, but we feel that in cases where ARM-2 and the isodesmic/isogyric work reactions are in agreement is not a mere coincidence.

Regardless of the correct reason for the disagreement, achieving accurate thermodynamics considering the large atomic size of Hg from a straightforward and computationally inexpensive atomization reaction scheme is of value. Based on our results, the ARM-2/$E_{CBS}(2,3,4)$ atomization reaction scheme can potentially be used to explore the thermodynamics between Hg and any H, F, O, and Cl combination. Although more testing is needed, based on atomic sizes and number of electrons involved, the ARM-2 atomization reaction scheme in theory can also be used for combinations of Hg molecules of the first 3 rows of the periodic table including C and N.

3.3.4 Bond Dissociation Energies for Hg Species and Potential Implications

The knowledge of the standard heats of formation, for the atoms and diatomics, allows us to calculate the X–Hg–Y bond dissociation energies (BDE). The BDE’s were calculated using our calculated ΔH^0_f and reference values from the Chase et al.[69] monograph or the ATcT[68] tables (see Tables 3.2 and 3.3). Figure 3.5 shows the BDE’s for all of the GOM species in this study.

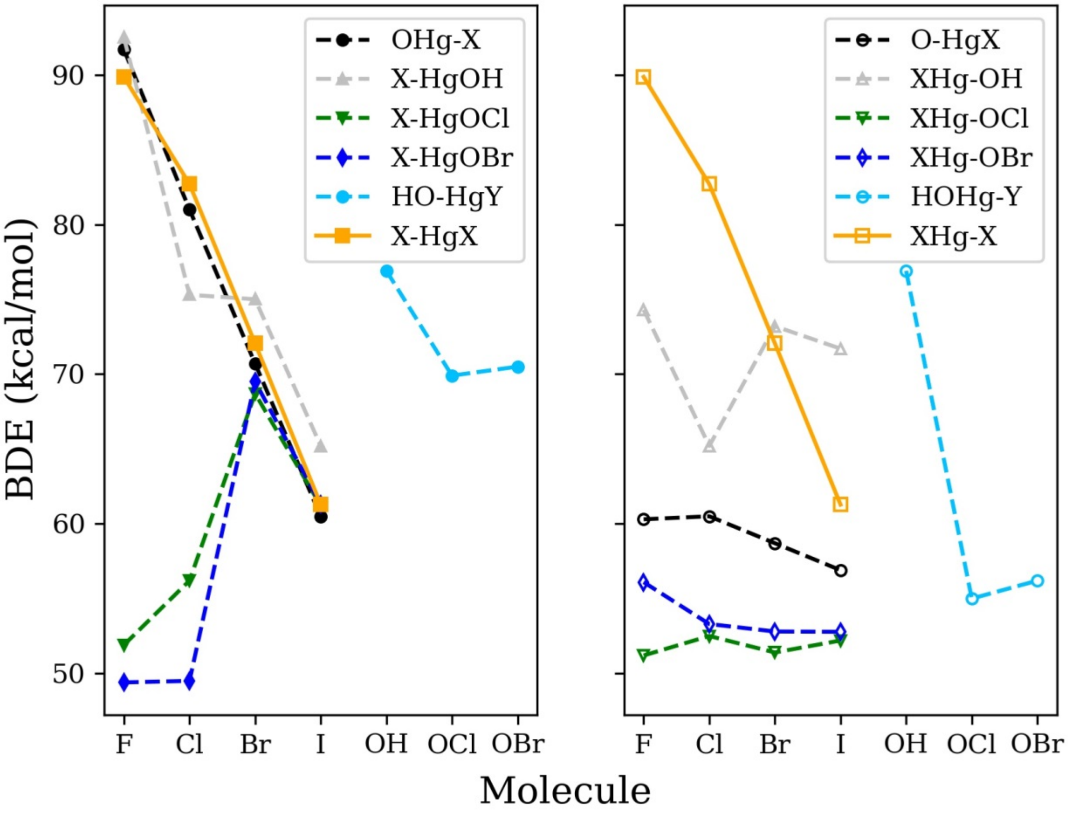

Figure 3.5 Bond dissociation energies (BDE) in kcal/mol for GOM species calculated from ΔH^0_f X = Halogen, Y = OH, OCl, or OBr.

Observations

- The XHg–X BDE calculated from reference data[59] monotonically decreases from F to I.
- The OHg–Y BDE decrease monotonically from F to I for the OHgY species.
- The BDE's of O–HgY monotonically decrease from Cl to I, with F having an almost equal BDE to Cl.
- The X–HgOH BDE for XHgOH decreases monotonically from F to I.
- The XHg–OH BDE decreases from F to Cl, increases from Cl to Br, and then decrease from Br to I.
- The HOHg–OCl and HOHg–OBr BDE's are very similar.
- The BDE's of X–HgOCl decreases from F to Cl, increases from Cl to Br, and then decreases from Br to I.
- The BDE's of X–HgOBr show a similar behavior with the exception of F–HgOBr and Cl–HgOBr being almost equal in value.
- The BDE's of XHg–OCl are similar in all cases with an average value of 51.8 +/- 0.57 kcal/mol.
- The BDE's for XHg–OBr are similar for ClHg–OBr, BrHg–OBr, and IHg–OBr with average values of 53 +/- 0.23 kcal/mol. The exception is FHg–OBr bonding is slightly stronger by ~ 3 kcal/mol.

Table 3.11 lists the exact BDE's including BDE's from the literature.

Table 3.11 Bond Dissociation Energies (BDE) at 298K in kcal/mol Determined from Calculated $E_{CBS}(2,3,4)$ Heats of Formation. Reference Values are in Parenthesis

XHgY	BDE(XHg + Y)	BDE(X + HgY)
OHgF	91.69	60.3
OHgCl	81.0 (79.7[a])	60.5 (62.2[a])
OHgBr	70.7 (70.4[a])	58.7 (59.7[a])
OHgI	60.5 (62.2[b])	56.9 (58.0[b])
FHgOH	92.5	74.3
ClHgOH	75.3	65.2
BrHgOH	75.0	73.2
IHgOH	65.2	71.7
$Hg(OH)_2$	76.9	
HOHgOCl	55.0	69.9
HOHgOBr	56.2	70.5
FHgOCl	51.2	51.9
ClHgOCl	52.5	56.2
BrHgOCl	51.4 (51.4[c])	68.7
IHgOCl	52.2	61.2
FHgOBr	56.1	49.4
ClHgOBr	53.3	49.5
BrHgOBr	52.83 (53.8[c])	69.5
IHgOBr	52.78	61.3

[a] From Balabanov and Peterson, value at 0 K[69]. [b] From Shepler et al., value at 0 K from [68]. [c] From Jiao and Dibble, value at 298K [59].

Where BDE data is available, our results are in very good agreement. With knowledge of the BDE's, we can now analyze how the GOM species in this study can potentially affect the established Hg chemistry models.

The gas phase oxidation of Hg^0 to GOM is thought to occur as a two-stage process as follows[12]:

$Hg^0 + X \rightarrow HgX$ R1

$HgX \rightarrow Hg^0 + X$ R2

$HgX + Y \rightarrow YHX$ R3
$HgX + Y \rightarrow Hg^0 + XY$ R4

Reactions R1 and R3 in this mechanism form the two-stage process and R2 and R4 are the competing or reverse reactions. Hg chemistry shows an interesting behavior in that the first Hg–X bond formed is significantly weaker than the second XHg–X/Y bond. The long-term stability of a GOM species is therefore predicated by the formation of the second Hg–X/Y bond. Using the reference values from Table 2 and 3 and heats of formation for HgOCl and HgOBr calculated using a work reaction scheme (see Table 3.12), we calculated the first stage HgX/Y molecules relevant to the molecules in this study.

Table 3.12 Heats of Formation at 298K for HgOH, HgOBr and HgOCl Averaged over Multiple Work Reactions. Isodesmic Reactions are Marked with an Asterisk (*). Work Reactions Using only Literature Reference Values are Highlighted with a Dagger (†). $E_{CBS}(2,3,4)$ Values are Recommended

Work Reaction	**M06-2X/ AVTZ**	**$E_{CBS}(2,3,4)$**
	ΔH_F (298K) (kcal/mol)	
$HgOH + HCl \rightarrow HgCl + H_2O$ †	11.69	9.76
$HgOH + HBr \rightarrow HgBr + H_2O$ †	12.00	11.41
$HgOH + HF \rightarrow HgF + H_2O$ †	12.26	9.9
$HgOH + CH_3F \rightarrow HgF + CH_3OH$ †	11.68	9.57
$HgOH + CH_3Cl \rightarrow HgCl + CH_3OH$ †	11.7	9.63
$HgOH + CH_3Br \rightarrow HgBr + CH_3OH$ †	12.42	9.00
AVG/STDEV	**11.96 +/- 0.32**	**9.87 +/- 0.81**
$HgOBr + CH_3OH \rightarrow HgOH + CH_3OBr$	45.06	44.96
$HgOBr + HgCl_2 \rightarrow HgCl + ClHgOBr$	43.37	44.47
$HgOBr + HgBr_2 \rightarrow HgBr + BrHgOBr$	42.27	43.81
AVG/STDEV	**43.57 +/- 1.40**	**44.41 +/- 0.57**
$HgOCl + CH_3OH \rightarrow HgOH + CH_3OCl$	40.32	39.45
$HgOCl + HgCl_2 \rightarrow HgCl + ClHgOCl$	40.18	40.16
$HgOCl + HgBr_2 \rightarrow HgBr + BrHgOCl$	39.25	39.58
AVG/STDEV	**39.91 +/- 0.58**	**39.73 +/- 0.38**

Table 3.13 Heats of Reaction for Possible First Stage of the Gaseous Hg^0 Oxidation Mechanism

$Hg + X \rightarrow HgX$	**ΔH_{rxn} (298K) (kcal/mol)**
$Hg + F \rightarrow HgF$ [a]	-32.95
$Hg + Cl \rightarrow HgCl$ [a]	-24.91
$Hg + Br \rightarrow HgBr$ [a]	-16.50
$Hg + I \rightarrow HgI$ [a]	-8.29
$Hg + OH \rightarrow HgOH$ [a,b]	-14.11
$Hg + OCl \rightarrow HgOCl$ [a,b]	0.75
$Hg + OBr \rightarrow HgOBr$ [a,b]	0.20

[a] Literature reference values are used for $Hg^{ref.}$ [19], F^{ref} [71], $Cl^{ref.}$ [71], $Br^{ref.}$ [71], $I^{ref.}$ [71], $OH^{ref.}$ [71], $OCl^{ref.}$ [71], $OBr^{ref.}$ [71], $HgF^{ref.}$ [19] and $HgCl^{ref.}$ [19]. [b] $E_{CBS}(2,3,4)$ reference values used for HgOH, HgOCl, and HgOBr (see Table 12).

Data in Table 3.13 illustrate that reactions of Hg^0 with F, Cl, Br, I, and OH are exothermic, but reactions with OCl and OBr are thermalyl neutral or slightly endothermic. It is therefore unlikely that molecules OCl and OBr will initiate elemental mercury oxidation or serve as initial reaction species in the process of GOM formation via the formation of HgOCl or HgOBr radicals. It is thought that reactions with Cl and Br are among the main pathways for the first stage. Since reaction with F is by far the most exothermic, under circumstances where there is a source of F available, such as during the combustion of coal[33], reactions with F can be an important initial pathway. Based on the thermodynamics, reactions with OH can also be a potential pathway for the first oxidation stage of Hg^0. The Hg–OH BDE is closer to ~ 2 kcal/mol weaker than Hg–Br, making HgOH a shorter lived species. The reaction with iodine atom can also work, however, the Hg–I bond is a factor of two weaker than Hg–Br or Hg–Cl.

Once the HgX species forms, it can then form a stable GOM compound by further reacting with any of F, Cl, Br, I, OH, OCl, and OBr as all of these reactions are exothermic. As shown earlier, the GOM species in this study have significant bond strengths in the range of 50 to 90 kcal/mol and if formed they should have a comparable lifetime to $HgCl_2$ and $HgBr_2$ (ClHg–Cl and BrHg–Br the BDE are 82.7 and 72.1 kcal/mol, respectively).

Recently, Dibble[81] has highlighted the importance of BrHgOH as a GOM species that can impact the global mercury budget. Dibble's calculations show that BrHgOH can form from BrHgO• via a hydrogen abstraction reaction from sp^3-hydridized carbons from organic compounds, such as CH_4 or C_2H_6. Given the abundance of organic compounds in the atmosphere and combustion flue gas, BrHgOH and by extension XHgOH, can have a major impact on the estimates of the global mercury budget. Using our calculated ΔH^0_f for XHgOH and XHgO, along with the reference values from Table 3.3, we calculated ΔH_{rxn} for the reactions $OHgX + CH_4 \rightarrow XHgOH + CH_3$ and $OHgX + C_2H_6 \rightarrow XHgOH + C_2H_5$. The results of these calculations at the $E_{CBS}(2,3,4)$ level of theory are presented in Table 3.14.

Table 3.14 Heats of Reaction[a] at 298K of XHgOH Formed via Hydrogen Abstraction from CH_4 and C_2H_6 at the $E_{CBS}(2,3,4)$ Level of Theory

Reaction	**$E_{CBS}(2,3,4)$**
	ΔH_{rxn} (298K) (kcal/mol)
Reactions with CH_4	
$OHgF + CH_4 \rightarrow FHgOH + CH_3$	-8.67
$OHgCl + CH_4 \rightarrow ClHgOH + CH_3$	-1.50
$OHgBr + CH_4 \rightarrow BrHgOH + CH_3$	-11.44
$OHgI + CH_4 \rightarrow IHgOH + CH_3$	48.17
Reactions with C_2H_6	
$OHgF + C_2H_6 \rightarrow FHgOH + C_2H_5$	-12.48
$OHgCl + C_2H_6 \rightarrow ClHgOH + C_2H_5$	-5.31
$OHgBr + C_2H_6 \rightarrow BrHgOH + C_2H_5$	-15.25
$OHgI + C_2H_6 \rightarrow IHgOH + C_2H_5$	44.36

[a] Reference heats of formation for OHgX, CH_4, CH_3, C_2H_6, and C_2H_5 are available in Tables 2 and 3. For XHgOH our calculated values in Table 3.8 are used as the reference.

As seen in Table 3.14, OHgF, OHgBr, OHgCl are able to abstract a hydrogen from either CH_4 or C_2H_6 forming their respective XHgOH species. The reactions of OHgI are strongly endothermic, making the formation of IHgOH via a hydrogen abstraction reaction an unlikely pathway. Of the molecules studied, the HOHgX (X = F, Cl, Br and OH) species should be the most likely exist over the XHgOCl or XHgOBr species since there are multiple formation pathways. XHgOH can form either an HgX or HgOH intermediate in stage one followed by a subsequent reaction with X or OH. XHgOH can also form via a hydrogen abstraction reaction between OHgX and a hydrocarbon.

3.4 Conclusions

Thermochemical properties (standard heats of formation, bond dissociation energies) of OHgX, XHgOH, HOHgOBr, $Hg(OH)_2$, HOHgOCl, XHgOBr, and XHgOCl (X = Halogen) were calculated using a series of isodesmic, isogyric, and atomization work reactions at 298K. Thermochemical properties calculated from the isodesmic and isogyric work reactions for the Hg species are in very good agreement with experimental data and the data from high-level *ab initio* calculations. Our work reaction approach allows for the study of significantly more molecules at a comparatively low computational cost. Standard heats of formation from the atomization reaction scheme are comparable to results from the work reactions for Hg species without any Br and I atoms. The bond dissociation energies of the second Hg–X/Y bond formed are significant and in the range of 50-90 kcal/mol. According to our calculations, the molecules studied should be considered in Hg modeling studies as the bond energies are comparable to the ClHgY and BrHgY species included in global GOM transport models.

CHAPTER 4

TOWARDS DIRECT MOLECULAR ANALYSIS OF ATMOSPHERIC OXIDIZED MERCURY

4.1 Abstract

Mercury is a persistent environmental pollutant entering the atmosphere mostly in elemental form and leaving in oxidized form. Its oxidation mechanism is poorly constrained because of the nearly non-existent knowledge of the molecular identities of the atmospheric gaseous oxidized mercury (GOM), severely hindering the evaluation of mercury deposition to the terrestrial environment. Here we present the development of a direct approach for detection of GOM, using ion drift - chemical ionization mass spectrometry (ID-CIMS). In this approach, GOM reacts in a drift tube at a 1-2 Torr pressure with an appropriate reagent ion to form well-defined product ions, which are detected by a quadrupole mass spectrometer equipped with a counting electron multiplier. We used $HgCl_2$ and $HgBr_2$ as model GOMs and $SF_6^–$, $CO_3^–$, $CO_4^–$, and $NO_3^–(HNO_3)$ as reagent ions, which were chosen based on the quantum chemical investigation of several possible reaction mechanisms, including charge transfer, ion transfer, and ion-molecule clustering. The model GOM react selectively with all reagent ions through one or more of the above mechanisms, with nearly equal efficiencies, in agreement with the results of the Average Dipole Orientation calculations of ion-molecule rate constants. We expect $NO_3^–(HNO_3)$ to be most useful in atmospheric applications because this ion is least affected by ubiquitous atmospheric chemicals, such as water. The current limit of detection of the

low-pressure ID-CIMS to $HgCl_2$ is about 1 part per trillion (at atmospheric pressure) with a 1 minute integration time, but it can be further reduced by 2-3 orders by utilizing chemical ionization at atmospheric pressure.

4.2 Experimental Studies of Ion-Molecule Reactions

Credit to the experimental measurements goes to Matt Cooper, John Antley, and Dr. Alexei Khalizov. For clarity, a summary of their measurements is provided in this dissertation.

Ion-molecule reactions were investigated using ion drift - chemical ionization mass spectrometry (ID-CIMS)[33]. In ID-CIMS, neutral molecules react with appropriate reagent ions in a drift tube to form well-defined product ions, which are detected by a mass spectrometer. In our experiments, neutral molecules were introduced in a flow of helium from a glass inlet, which contained a plug of fiberglass wool impregnated with $HgCl_2$ and $HgBr_2$. Reagent ions were generated by passing a trace amount of an appropriate precursor in a carrier gas through the corona discharge established between a stainless needle and a stainless tube. The voltage drop across the discharge gap was around 500 V and the current was limited by two 2-MΩ resistors, one at each side of the gap. The SF_6– reagent ion was generated from the SF_6/N_2 gas mixture, along with a small amount of amount of SF_5^- (SF_6–:SF_5^- = 10:1). The CO_3^- and $CO_2{\cdot}O_2^-$ reagent ions (1:1) were produced from the CO_2/O_2 mixture. The $NO_3^-(HNO_3)$ reagent ion was generated from the HNO_3/N_2 mixture, along with small amounts (less than 10%) of NO_3^- and $NO_3^-(HNO_3)_2$. The purpose of the drift tube was to control ion trajectories, ion clustering, and ion-molecule reaction time. In the presence of a 10-40 V cm^{-1} electric field at a 1-2 Torr pressure, the ions were contracted in a relatively narrow beam (2 mm) and the ion-molecule reaction time in the drift tube ranged between 0.5 and 1.5 millisecond, depending on the gas flow velocity, gas pressure, and electric field strength[82]. A collimated ion beam entered a vacuum chamber through a 0.3 mm pinhole, where the ions were detected with a quadrupole mass spectrometer. The chamber was differentially pumped using two Agilent TwisTorr 304 FS turbo pumps. The mass spectrometer was Extrel (19 mm quadrupole, 880 kHz oscillator, 5221 Command System, 2-1000 amu mass range) with a DeTech 402A-H electron multiplier and a counting pre-amplifier (MTS-100, Advanced Research Instruments).

4.3 Results and Discussion

4.3.1 Selection of Reagent Ions for ID-CIMS

Reagent ions SF_6–, CO_2•O_2–, and CO_3– were selected because of their use in prior studies for the detection of trace atmospheric gases. SF_6– was used for the detection of $ClNO_3$, O_3, NO_2, N_2O_5, and SO_2[83-85]. SF_6– reacts via charge and ion transfer mechanisms, depending on the trace gas it reacted with. Reagent ion CO_3– was used for the detection of SO_2, H_2SO_4, and HNO_3 using CIMS[85-87]. The CO_2•O_2– (CO_4-) complex was used for HNO_3 and HCOOH detection using an ion-molecule reaction mass spectrometry system [87, 88]. The HNO_3•NO_3– reagent ion was used for the detection of H_2SO_4[89].

4.3.2 GOM product ions geometries

Presented in Figure 4.1 are the structures of the product ions from reactions of $HgCl_2$ with the reagent ions $SF_6–$, $CO_3–/CO_2•O_2–$, and $HNO_3•NO_3–$. In all cases, the negatively charged ion coordinates with the Hg atom. Compared to free molecule, $HgCl_2$ as part of the complex is nonlinear (125 to 155 degrees; neutral $HgCl_2$ is linear) and has a longer Hg–Cl bond length (2.39 to 2.59 Å; neutral $HgCl_2$ is 2.28 Å). In cases where more than one atom is added to $HgCl_2$ the lowest energy structure was found by rotating the ion either in plane or perpendicular to the plane of $HgCl_2$. If more than one converging structure was found, the structure with the lowest energy was used. Although a more rigorous approach would be to scan the dihedrals and angles in incremental step sizes of 10 degrees and repeat the process until the lowest energy structure is found, this approach is problematic because Hg-containing molecules have a tendency of forming linear angles, which cause optimization errors during intermittent steps.

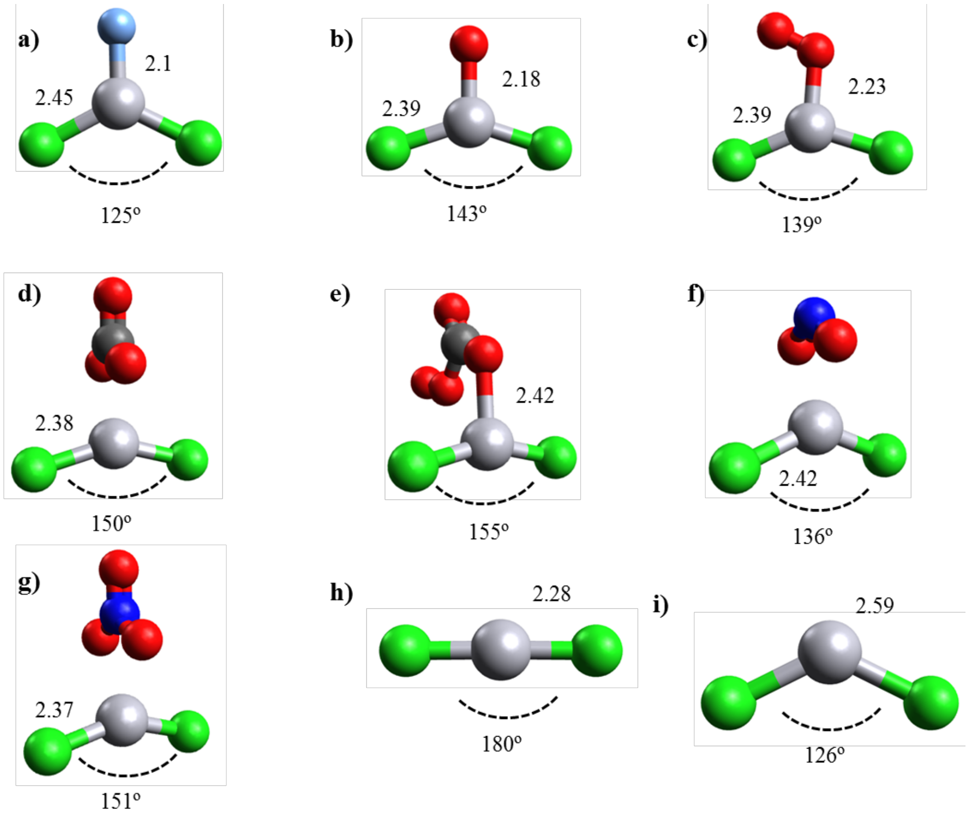

Figure 4.1. Structures of product ions produced in the reactions of $HgCl_2$ with several different reagent ions. Geometries were optimized at the M06-2X/AVTZ level of theory. (a) $HgCl_2$•F–, (b) $HgCl_2$•O–, (c) $HgCl_2$•O_2–, (d) $HgCl_2$•CO_3–, (e) $HgCl_2$•(CO_2•O_2–), (f) $HgCl_2$•NO_2–, (g) $HgCl_2$•NO_3– , (h) $HgCl_2$ and (i) (h) $HgCl_2$–. Bond lengths are shown in units of Å.

4.3.3 Electron Affinities

Electron affinities (EA) are used to screen which reagents ions are likely to react via a charge transfer reaction. Table 4.1 shows the EA of $HgCl_2$ and selected product species, which can form in reaction of $HgCl_2$ and with parent reagent ions. The EA is as $-\Delta H_{rxn}$. The DFT methods are within 0.03 to 0.27 eV of each other for the EA calculations. Neither DFT method is either consistently higher or lower than the other for the EA calculations. Compared to DFT, CCSD(T) EA results are lower in energy.

In order for charge transfer to occur, the EA of $HgCl_2$ must be greater than that of the reagent ion. SF_6– is therefore the only reagent ion that can react with $HgCl_2$ via a charge transfer reaction.

Table 4.1 Electron (EA) Affinities of in Units of eV at 298K, Obtained at the DFT (M06-2X/AVTZ and PBE0/AVTZ) and CCSD(T)/AVTZ//M06-2X/AVTZ Theory Levels

Reaction	**EA = - ΔH$_{rxn}$ (298K) (eV)**		
	M06-2X/AVTZ	**PBE0/AVTZ**	**CCSD(T)/AVTZ//M06-2X/AVTZ**
Electron Affinities			
$SF_6 \rightarrow SF_6$–	**1.47**	**1.63**	**1.23**
$SF_5 \rightarrow SF_5$–	4.24	3.99	4.12
$O_2 \rightarrow O_2$	2.01	2.04	1.70
$O_3 \rightarrow O_3$–	2.74	2.47	
$CO_3 \rightarrow CO_3$–	4.10	4.27	
CO_2•$O_2 \rightarrow CO_2$•O_2–	3.16	3.19	2.72
$HgCl_2 \rightarrow HgCl_2$–	**1.84**	**1.65**	**1.60**

4.3.4 Reaction of $HgCl_2$ with SF_6–

Measured mass spectra of the reagent and product ions generated in the reaction of SF_6– with $HgCl_2$ are shown in Figures 4.2a and 4.2b, respectively. The reagent ions SF_6– and SF_5^- were identified by the peaks at 146 and 127 amu, respectively. SF_5– is formed as by product from the corona discharge ionization of SF_6. A typical signal intensity of SF_6– was about 20 MHz. The only product ion detected was $HgCl_2F$–, observed as a multiplet between 266 and 276 amu with a peak intensity of 5.8 kHz. The multiple peaks are caused by six abundant stable isotopes in mercury (198, 199, 200, 201, 202, and 204) and two in chlorine (m/z 35 and 37). Recorded mass spectra are in excellent agreement with predicted isotope distributions for $HgCl_2$•F–.

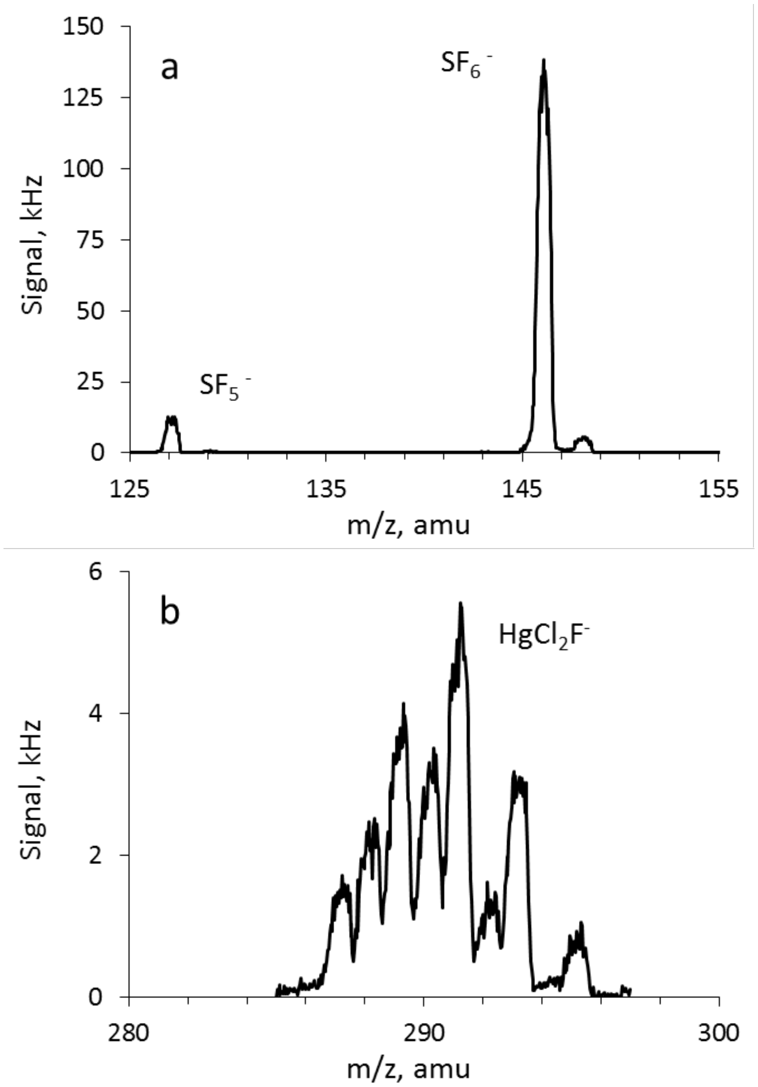

Figure 4.2 Mass spectra of (a) reagent ions generated through corona discharge in SF_6/N_2 and (b) corresponding ion product $HgCl_2$•F^-. The displayed mass spectrum of reagent ions was obtained using a lower multiplier voltage to extend the multiplier lifespan.

Table 4.2a shows the enthalpies of reaction and proposed mechanism of the formation of SF_6– and SF_5– in the corona discharge in a mixture SF_6 and N_2. Table 4.2b shows the enthalpies of reaction forming $HgCl_2F$– starting from reagent ion SF_6–. We categorize the reactions in Table 2b into two distinct sets: (1) reactions with neutral $HgCl_2$ and (2) reactions with anion $HgCl_2$–, which can be formed from neutral $HgCl_2$. Exothermic reactions are given in bold font.

Table 4.2a Reaction Enthalpies of the Formation SF_6– and SF_5^- Through Corona Discharge of a Mixture SF_6/N_2 Calculated at Three Different Theory Levels at 298K

Reaction	**ΔH_{rxn} (298K) (kcal/mol)**		
	M06-2X/ AVTZ	**PBE0/ AVTZ**	**CCSD(T)/AVTZ// M06-2X/AVTZ**
SF_6 + e– → SF_6–	33.88	37.68	28.37
SF_6 + e– → SF_5– + F	4.10	2.77	5.81
SF_6 + e– → SF_5 + F–	25.77	19.98	24.55

Table 4.2b Enthalpies of $HgCl_2$ Reactions in the SF_6 System, Calculated at Three Different Theory Levels at 298K

Reaction	**ΔH_{rxn} (298K) (kcal/mol)**			**k_{ADO} (10^{-10} cm^3 $molecule^{-1}$ s^{-1})**
	M06-2X/ AVTZ	**PBE0/ AVTZ**	**CCSD(T)/AVTZ// M06-2X/AVTZ**	**M06-2X/ AVTZ**
Reactions with neutral $HgCl_2$				
$HgCl_2$ + SF_6– → $HgCl_2$•F– + SF_5	4.12	1.85	**-0.85**	5.72
$HgCl_2$ + SF_6– → $HgCl_2$– + SF_6	**-0.46**	**-8.55**	**-8.46**	**5.72**
$HgCl_2$ + SF_5^- → $HgCl_2$•F– + SF_4	3.28	0.85	0.48	5.99
$HgCl_2$ + SF_5^- → $HgCl_2$– + SF_5	53.84	55.24	58.28	5.99
Reactions with anion $HgCl_2$–				
$HgCl_2$– + SF_6 → $HgCl_2$•F– + SF_5	4.58	10.40	7.61	5.21
$HgCl_2$– + SF_5 → $HgCl_2$•F– + SF_4	**-50.56**	**-54.39**	**-57.80**	**5.83**
$HgCl_2$– + SF_4 → $HgCl_2$•F– + SF_3	-1.83	1.41	-1.96	7.07
$HgCl_2$– + SF_3 → $HgCl_2$•F– + SF_2	**-31.99**	**-38.41**	**-41.44**	**7.57**

Among the reactions of neural $HgCl_2$, the most exothermic process is $HgCl_2$ + SF_6– → $HgCl_2$– + SF_6, followed by $HgCl_2$ + SF_6– → $HgCl_2$•F– + SF_5, which is slightly endothermic according DFT but slightly exothermic according to the CCSD(T). Among the reactions of anion $HgCl_2$–, $HgCl_2$– + SF_5 → $HgCl_2$•F– + SF_4 is the most exothermic followed by $HgCl_2$– + SF_3 → $HgCl_2$•F– + SF_2. Reaction $HgCl_2$– + SF_6 → $HgCl_2$•F– + SF_5 is endothermic according to both DFT and CCSD(T) calculations. $HgCl_2$– + SF_4 → $HgCl_2$•F– + SF_3 is slightly endothermic according the M06-2X but slightly exothermic according to PBE0.

Based on our computational results, there are two possible mechanisms for the formation of $HgCl_2F$– from SF_6–. The first pathway is a two-step mechanism where the first step is a charge transfer reaction where SF_6– gives an electron to $HgCl_2$ forming $HgCl_2$–. This is supported by the reaction $HgCl_2$ + SF_6– → $HgCl_2$– + SF_6 being exothermic and the EA of $HgCl_2$ being larger than that of SF_6. Once $HgCl_2$– is formed, it can react with a neutral SF_n (n = 5 or 3) species forming the detected $HgCl_2$•F^-. Assuming that neutral SF_5 is available in quantities proportional to anion SF_5^-, it is likely that the dominant pathway is the reaction of SF_5 rather than with SF_3 as SF_5– is detected in significant quantities. A second mechanism for $HgCl_2$•F– formation is a one-step reaction of between neutral $HgCl_2$ and SF_6– or SF_5–. For these reactions the calculations DFT methods are endothermic but and the single point CCSD(T)/M06-2X energy is exothermic.

For the GOM and SF_n molecules the spin multiplicities are as follows: $HgCl_2$, $HgCl_2$•F– SF_6, SF_2, and SF_4 are closed shell singlets; $HgCl_2$– , SF_6–, SF_5 and SF_3 are open shell doublets. A common feature of the exothermic reactions in Table 2b is that the SF_n product formed is in the singlet state. Mercury products could be either in the singlet or doublet state, so a conclusion can be drawn that the SF_n reactions are mediated by the product state of SF_n. One exemption to this is the reaction $HgCl_2 + SF_5– \rightarrow HgCl_2•F– + SF_4$ where the reaction is closer to being thermoneutral rather than exothermic.

According to thermodynamic calculations, the two-step mechanism ($HgCl_2 + SF_6– \rightarrow HgCl_2– + SF_6$ and $HgCl_2– + SF_5 \rightarrow HgCl_2•F– + SF_4$) and the one step mechanism ($HgCl_2 + SF_6– \rightarrow HgCl_2•F– + SF_5$) are both viable pathways for the formation of $HgCl_2•F–$ via the reaction with $SF_6–$. A kinetic calculation is required to elucidate which of the two mechanisms can form $HgCl_2•F–$ during experimentally constrained reaction time inside the drift tube while producing no detectable $HgCl_2–$. The reaction times were computed as a function of the $HgCl_2$, $SF_6–$, and SF_5 concentrations for both the two-step and one-step mechanism as follows:

- The initial concentration of $HgCl_2$ is 1 x 10^8 molecules/cm^3
- The initial concentration of SF_6^- and final concentration of $HgCl_2•F^-$ were estimated from the measured product ion signals as 6.0 x 10^9 and 3.0 x 10^6 molecules/cm^3, respectively.
- The neutral concentration SF_5 is assumed to equal the concentration of the anion SF_5^-. Based on the product ion signals, the $[SF_5^-]$ is estimated as $[SF_6^-]$ / 6 = 1.0 x 10^9 molecules/cm^3.
- k_{ADO} is used as the rate constants for all reactions.
- The initial concentrations of $[HgCl_2\text{-}]$, $[SF_6]$, $[SF_4]$, and $[HgCl_2•F^-]$ were set to zero.

- For a pressure of 1.8 Torr, an initial flow rate of 500 sccm, a drift tube length of 15 cm, and an electric field of 9 V/cm, the residence time in the drift-tube was calculated as 1.2 ms.

Using these initial conditions, the rate equations for the one-step ($HgCl_2$ + SF_6– → $HgCl_2$•F– + SF_5) and two-step ($HgCl_2$ + SF_6– → $HgCl_2$– + SF_6 and $HgCl_2$– + SF_5 → $HgCl_2$•F– + SF_4) mechanism were solved numerically and the results are shown in Figures 4.3 and 4.4, respectively. Based on these calculations, the time required for the concentration of $HgCl_2$•F^- to reach the final measured concentration of 3.0 x 10^6 molecules/cm^3 is 8.9 ms and 196 ms, for the one-step and two-step mechanisms, respectively. Considering that the residence time in the drift tube is 1.2 ms, it unlikely that the there is enough time for $HgCl_2$•F– to form via the two-step mechanism. We note that in order to match the experimental $HgCl_2$•F– concentration of 3.0 x 10^6 molecules/cm^3 within 1.2 ms, an initial concentration of 40.0 x 10^9 for SF_6– is required. This change in [SF_6–] also reduces the time for the two-step mechanism from 196 to 19 ms, which is still significantly more than the residence time in the drift tube. Considering that using k_{ADO} is an estimate for the rate constant and that the concentrations of SF_6–, SF_5–, and $HgCl_2$•F– are experiment-based estimates, the results are nonetheless in good agreement. Furthermore, according to Figure 4.4, a significant concentration of $HgCl_2$– should have been formed in the two-step mechanism, contrary to the experimental observations. The calculations also show that in both cases only a small fraction of $HgCl_2$ is converted, confirming the validity of Equation (1.9) (equation in Chapter 1 for the concentration of ions based on the initial rate).

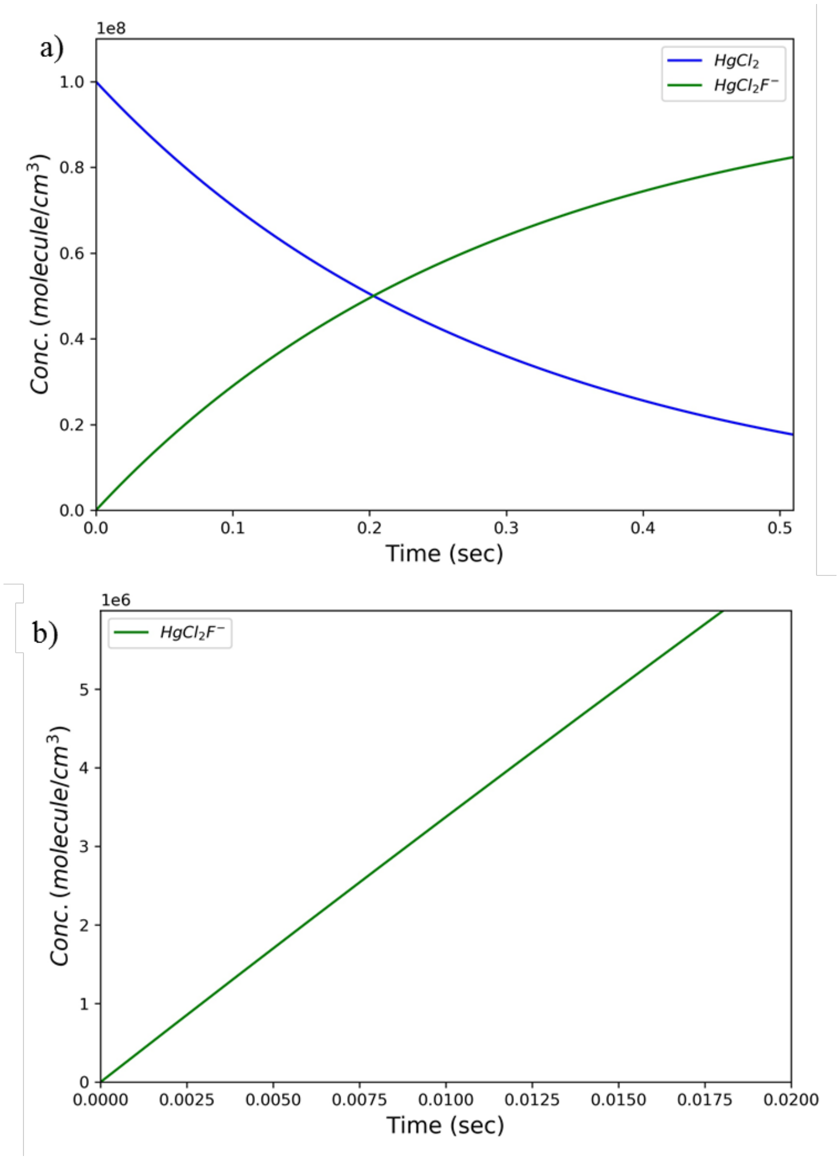

Figure 4.3 Concentrations of $HgCl_2$ and $HgCl_2$•F– for the one-step reaction mechanism.

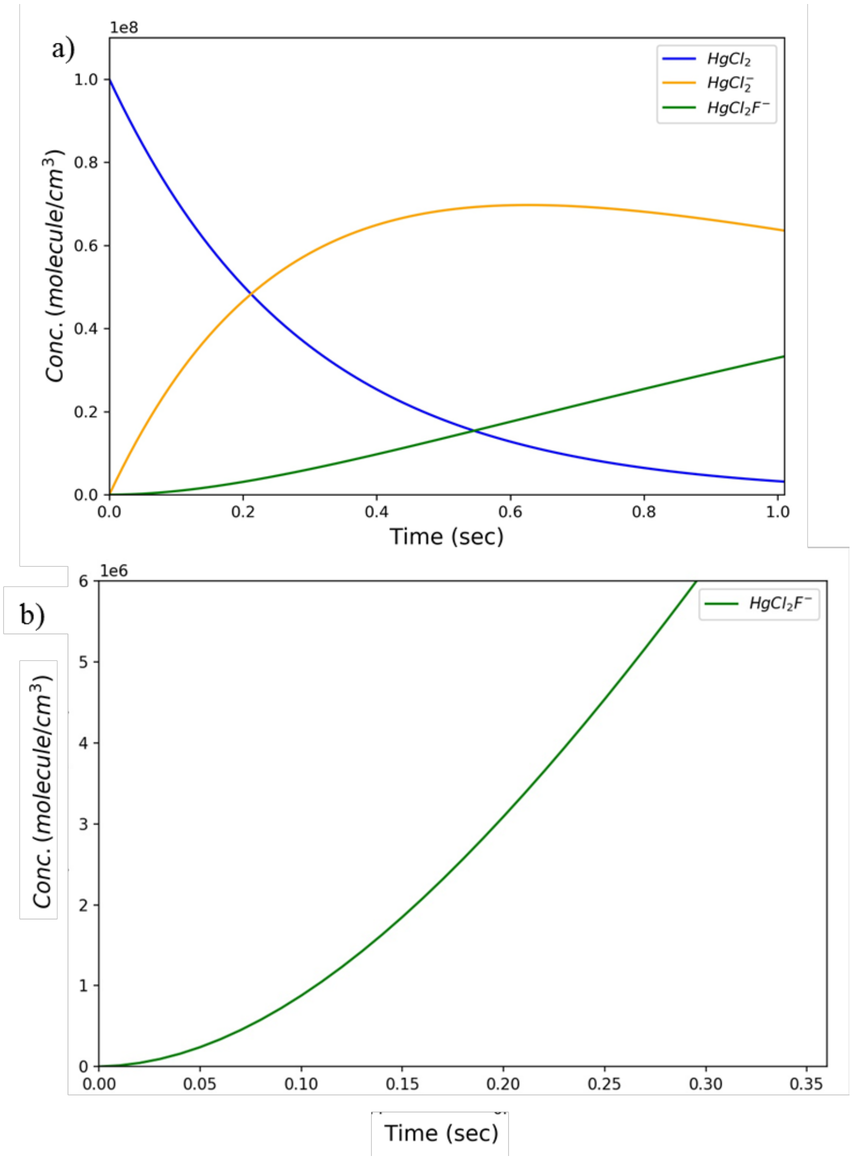

Figure 4.4 Concentrations of $HgCl_2$, $HgCl_2$–, and $HgCl_2$•F–, for the two-step reaction mechanism.

4.3.5 Reactions $HgCl_2$ + CO_3– and $HgCl_2$ + CO_2•O_2–

Figure 4.5a shows mass spectrum of ions generated by corona discharge in CO_2/O_2, including NO_2–, O_2–(H_2O) , O–$(H_2O)_2$, CO_3–, CO_2•O_2–, and CO_2•O_2–(H_2O), as identified by the peaks at m/z 46, 50, 53, 60, 76, and 94 amu, respectively. The strongest signals are for CO_3– and CO_2•O_2– with corresponding peak intensities of 120 kHz and 95 kHz, respectively (the displayed mass spectrum of reagent ions was obtained using a lower multiplier voltage; the actual peak intensities were about 10 MHz). A mechanism explaining the formation of CO_3^- and $CO_2{\bullet}O_2^-$ from CO_2/O_2 is given in Table 4.3a.

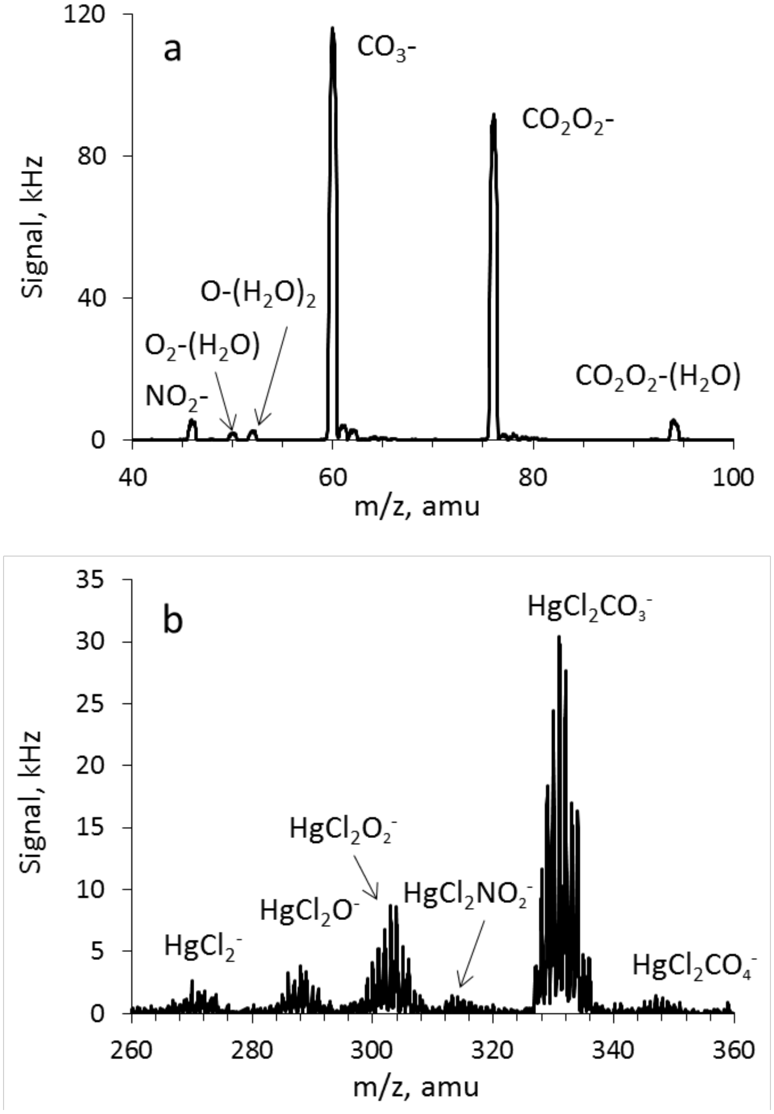

Figure 4.5 Mass spectra of (a) reagent ions generated through corona discharge in CO_2/O_2 and (b) corresponding ion products produced in reactions with $HgCl_2$. The displayed mass spectrum of reagent ions was obtained using a lower multiplier voltage to extend the multiplier lifespan.

Table 4.3a Reaction Enthalpies of the Formation CO_3– and CO_2•O_2– from Corona Discharge of a Mixture CO_2/O_2 Calculated at Three Different Theory Levels at 298K.

Reaction	ΔH_{rxn} (298K) (kcal/mol)		k_{ADO} (10^{-10} cm^3 $molecule^{-1}$ s^{-1})
	M06-2X/ AVTZ	PBE0/ AVTZ	M06-2X/ AVTZ
e– + O_2 → O_2-	46.33	47.15	
e– + O_2 + O_2 → O– + O_3	-4.91	5.42	
O_2– + O_2 → O_4–	-41.19	-47.68	7.48
O– + O_2 → O_3–	-75.57	-80.26	9.17
O_4– + O → O_3– + O_2	-80.21	-86.25	5.65
CO_2 + O_3- → CO_3– + O_2	12.30	10.97	8.17
CO_2 + O– → CO_3– + O_2	-63.26	-69.28	11.43
CO_3– + O → CO_2 + O_2–	-92.55	-96.53	5.69
CO_2 + O_2– → CO_2•O_2–	-26.56	-26.44	9.10
CO_2 + O_2– → CO_2•O_2–	14.63	21.23	7.67
CO_2•O_2– + O → CO_3– + O_2	-82.53	-96.51	5.56

Note: Mechanism is Taken from Amelynck, Fussen, and Arjis
Source: [86]

The first step in the formation of CO_3– and CO_2•O_2– is the ionization and subsequent reactions of O_2 producing O–, O_2–, O_3–, and O_4–. Although according to the mechanism, both O_3– and O_4– can form, they are not experimentally detected in our system. Therefore, O_3– and O_4– are not important product ions pertinent to the formation of CO_3– and CO_2•O_2– and subsequent reactions with $HgCl_2$. The product anions O– and O_2– react with CO_2 producing CO_3^- and CO_2•O_2^-. According to the thermodynamics, there are 3 pathways (CO_2 + O_3- → CO_3– + O_2, CO_2 + O– → CO_3– + O_2, and CO_2•O_2– + O → CO_3– + O_2) forming CO_3- and 2 pathways (CO_2 + O_2– → CO_2•O_2–and CO_2 + O_2– → CO_2•O_2–) forming CO_2•O_2–. Once formed, both CO_3– and CO_2•O_2– can further react with neutral O and produce O_2– and CO_3–. We note that the mechanism presented does not have a reaction producing neutral O, however, it is possible that O can form directly from the dissociation of O_2 due excess energy available from the corona discharge. A plausible concentration of O could be similar to anion O– which is a direct O_2 ionization by-product via $e– + O_2 + O_2 \rightarrow O– + O_3$.

The measured spectra also show the ions O_2– (H_2O), O– $(H_2O)_2$ and $CO_2{\bullet}O_2$–(H_2O). These can form when O– and O_2– from corona discharge ($e– + O_2 \rightarrow O_2$-and $e– + O_2 + O_2 \rightarrow O– + O_3$) react with trace H_2O molecules in the system. Similarly, $CO_2{\bullet}O_2$–(H_2O) can form via the $CO_2{\bullet}O_2$- + H_2O reaction.

Table 4.3b Reaction Enthalpies of the Formation of $HgCl_2{\bullet}O$–, $HgCl_2{\bullet}O_2$–, $HgCl_2{\bullet}CO_3$–, and $HgCl_2{\bullet}(CO_2{\bullet}O_2$–) in kcal/mol from Reagent Ions O_2–, $CO_2{\bullet}O_2$– and CO_3– Calculated at Three Different Theory Levels at 298K

Reaction	**ΔH_{rxn} (298K) (kcal/mol)**			**k_{ADO} (10^{-10} cm^3 molecule^{-1} s^{-1})**
	M06-2X/ AVTZ	**PBE0/ AVTZ**	**CCSD(T)/AVTZ// M06-2X/AVTZ**	**M06-2X/ AVTZ**
$HgCl_2$ + O– → $HgCl_2{\bullet}O$–	-46.63	-64.75	-39.77	14.3
$HgCl_2$ + O– → $HgCl_2$– + O	-9.90		-6.13	14.3
$HgCl_2$– + O → $HgCl_2{\bullet}O$–	-33.73		-33.64	
$HgCl_2$ + O_2– → $HgCl_2{\bullet}O_2$–	-36.39	-33.07	-34.29	10.4
$HgCl_2$ + CO_3– → $HgCl_2{\bullet}CO_3$–	-31.23	-24.79	-29.43	7.95
$HgCl_2{\bullet}CO_3$– → $HgCl_2$– + CO_3–	83.30	85.08	84.34	
$HgCl_2{\bullet}CO_3$– → $HgCl_2{\bullet}O$– + CO_2	50.86	29.33	51.42	
$HgCl_2$ + $CO_2{\bullet}O_2$– → $HgCl_2{\bullet}(CO_2{\bullet}O_2$–)	-26.41	-21.32	-25.48	7.23
$HgCl_2$ + $CO_2{\bullet}O_2$– → $HgCl_2{\bullet}O_2$– + CO_2	-9.83	-6.62	-10.86	7.23
$HgCl_2 + NO_2^- \rightarrow HgCl_2{\bullet}NO_2^-$	-42.25	-38.30		8.88

Figure 4.5b shows the mass spectra of the product ions produced in the reaction of $HgCl_2$ with the above reagent ions. These product ions include $HgCl_2$–, $HgCl_2{\bullet}O$–, $HgCl_2{\bullet}O_2$–, $HgCl_2{\bullet}NO_2$–, $HgCl_2{\bullet}CO_3$– and $HgCl_2{\bullet}(CO_2{\bullet}O_2$–) identified by the peaks at

265–275 amu, 285–295 amu, 295–310 amu, 315–323 amu, 325–335 amu, and 335–355 amu, respectively. In ascending order of the signal strength, the intensities are $HgCl_2$•(CO_2•O_2–) (2 kHz), $HgCl_2$•NO_2– (2 kHz), $HgCl_2$– (3 kHz), $HgCl_2$•O– (5 kHz), $HgCl_2$•O_2– (10 kHz), and $HgCl_2$•CO_3– (32 kHz). Table 3b shows the enthalpies of reaction for the formation of these product ions, in the order of ascending reagent ion size. All of the reactions are exothermic, with the most exothermic being $HgCl_2$ + O– → $HgCl_2$•O– and the least exothermic being $HgCl_2$ + CO_2•O_2– → $HgCl_2$•O_2– + CO_2. Between M06-2X and PBE0, the former produces more exothermic results with the exception of $HgCl_2$ + O– → $HgCl_2$•O–, where PBE0 is more exothermic by 18 kcal/mol. CCSD(T) calculations are less exothermic for $HgCl_2$ + O– → $HgCl_2$•O–, $HgCl_2$ + O_2– → $HgCl_2$•O_2–and $HgCl_2$ + CO_3– → $HgCl_2$•CO_3– compared to both DFT methods. For $HgCl_2$ + CO_3– → $HgCl_2$•CO_3–, CCSD(T) enthalpies are in between of both DFT methods and for $HgCl_2$ + CO_2•O_2– → $HgCl_2$•O_2– + CO_2, CCSD(T) calculations are more exothermic. All of the ions are an open shell doublet: O–, O_2–, CO_3–, $HgCl_2$•O–, $HgCl_2$•O_2–, $HgCl_2$•CO_3–, and $HgCl_2$•(CO_2•O_2–).

The reaction $HgCl_2$ + O– → $HgCl_2$•O– is the most exothermic and has the largest k_{ADO} rate constant. O– can also react with $HgCl_2$ by charge transfer, forming anion $HgCl_2$–. $HgCl_2$– can then react with O giving another pathway for the formation of $HgCl_2$•O– . For these specific pathways a source of O– is required. The mass spectra O– as oxygen anion dehydrate, O– $(H_2O)_2$. An alternative pathway could also be the reaction with O– $(H_2O)_2$, as O– $(H_2O)_2$ → $HgCl_2$•O– + $2H_2O$.

$HgCl_2$•O_2– can form via two pathways, the reaction of $HgCl_2$ with O_2^- or with CO_2•O_2^-. Of the two pathways, the latter is the most likely because CO_2•O_2^- is available in much larger quantities than O_2–. The O_2– signal at 32 amu is low (< 1 kHz) because most of O_2– is rapidly converted to CO_2•O_2– via $CO_2 + O_2– \rightarrow CO_2•O_2–$. A small fraction of $HgCl_2$•O_2^- can form through the reaction with the superoxide hydrate, $HgCl_2 + O_2– (H_2O) \rightarrow HgCl_2•O_2– + H_2O$.

Between $HgCl_2$•CO_3– and $HgCl_2$•(CO_2•O_2–), the signal strength of $HgCl_2$•CO_3^- is a factor of 15 larger, but the CO_3– and CO_2•O_2– signals are of comparable intensity. Both $HgCl_2$•CO_3– and $HgCl_2$•(CO_2•O_2–) form via one-step reactions directly from corresponding reagent ions, so it is perplexing that the $HgCl_2$•CO_3^- and $HgCl_2$•(CO_2•O_2–) signals are not also proportional to the signals of CO_3– and CO_2•O_2–. In order to understand this difference, we solved numerically for the $HgCl_2$•CO_3– and $HgCl_2$•(CO_2•O_2–) for reactions $HgCl_2 + CO_3– \rightarrow HgCl_2•CO_3–$, $HgCl_2 + CO_2•O_2– \rightarrow HgCl_2•(CO_2•O_2–)$, and $HgCl_2 + CO_2•O_2–\rightarrow HgCl_2•O_2– + CO_2$ as a function of time. The reaction $HgCl_2 + CO_2•O_2–\rightarrow HgCl_2•O_2– + CO_2$ in the system of equations because it competing with $HgCl_2 + CO_2•O_2– \rightarrow HgCl_2•(CO_2•O_2–)$ i.e., same reactants ($HgCl_2$ + CO_2•O_2–), but different products ions formed ($HgCl_2$•O_2– and $HgCl_2$•(CO_2•O_2–)). The initial concentrations (in molecules / cm^3) of $[HgCl_2] = 1 \times 10^8$, $[CO_3–] = 4.9 \times 10^9$, and $[CO_2•O_2–] = 3.9 \times 10^9$ were estimated from the reagent product ion signals. The results of these calculations are shown in Figure 4.6.

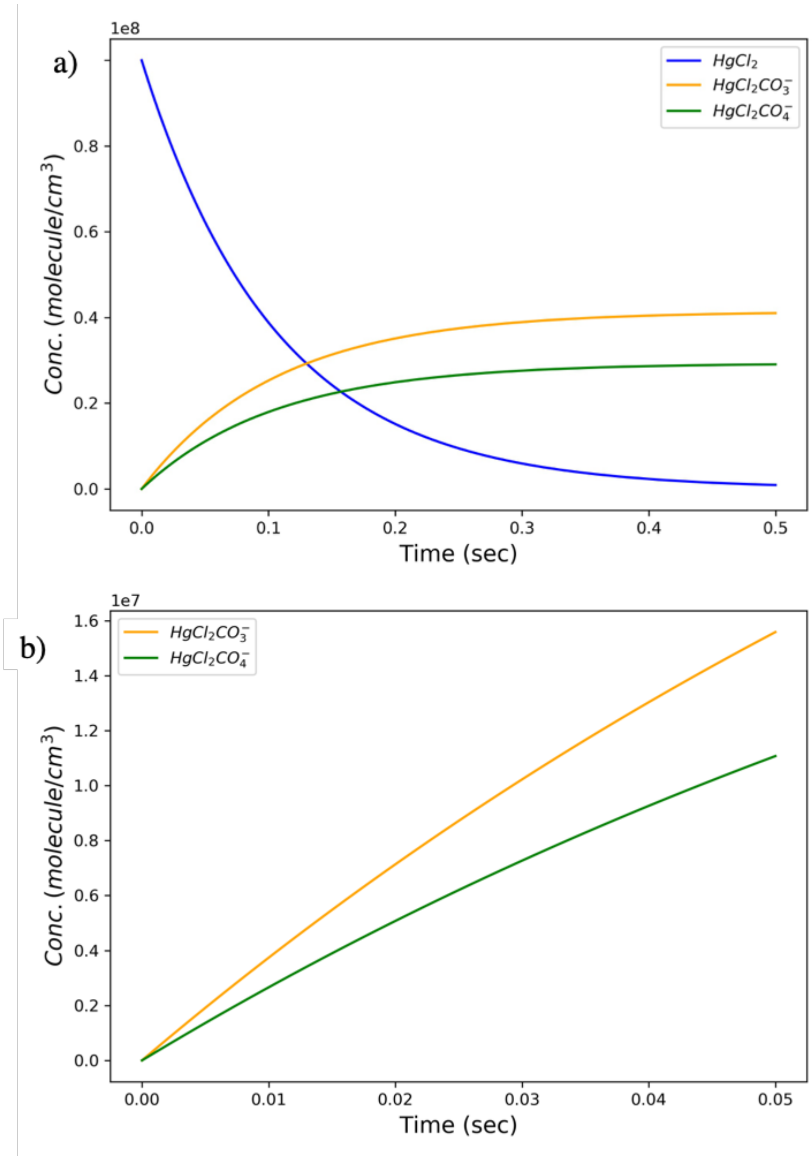

Figure 4.6 Concentrations of $HgCl_2•CO_3–$ and $HgCl_2•(CO_2•O_2–)$ for the $HgCl_2 + CO_2/O_2$ system.

As seen in Figure 4.6, because reactions $HgCl_2 + CO_2•O_2– \rightarrow HgCl_2•(CO_2•O_2–)$ and $HgCl_2 + CO_2•O_2– \rightarrow HgCl_2•O_2– + CO_2$ are competing, $HgCl_2•CO_3–$ is able form faster than $HgCl_2•(CO_2•O_2–)$. However, neither at 500 or 5 ms, the latter which is the residence time, is the calculated concentration of $HgCl_2•CO_3–$ close to a factor of 15 larger than $HgCl_2$•(CO_2•O_2–). The calculations are trending in the right direction, but there must be another explanation.

In the drift-tube, an electric field (-15 V/cm) is used to guide the ions towards the pinhole. In the pinhole region, the field is even stronger (-55 V/cm). The increase in the electric field increases the rate of molecular collisions and kinetic energy of the ions. The increase in kinetic energy therefore corresponds to an increase in the effective temperature. The effective temperature can be calculated as:

$$T_{eff} = \frac{V\lambda}{R} \tag{4.1}$$

where V is the electric field, λ is the mean free path of the molecules, and R is the ideal gas constants. Based on these fields and $\lambda = 2 \times 10^{-3}$ cm, the calculated effective temperatures are $T_{\text{drift-tube}} = 665$ K and $T_{\text{pinhole}} = 1914$ K for the drift-tube and pinhole regions, respectively. The Gibbs energy of reaction ($\Delta G = \Delta H - T\Delta S$) could therefore be significantly different at these temperatures because of the $T\Delta S$ term. Using a statistical mechanics approach for the entropy and enthalpy contribution, we calculated the ΔG_{rxn} as a function of temperature. The results of these calculations are presented in Figure 4.7.

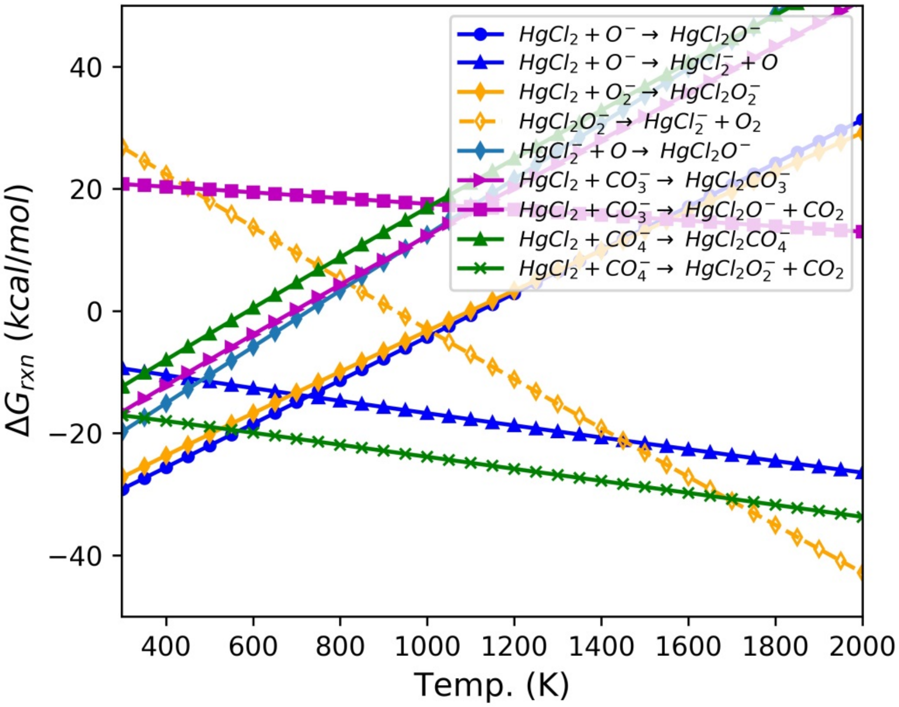

Figure 4.7 Free energies of reaction for the $HgCl_2$ and CO_2/O_2 system at 1.8 Torr.

The following observations can be made based on Figure 4.7:

- ΔG for $HgCl_2$ + O– → $HgCl_2$•O– monotonically **increases** between 298 and 2000 K, changing sign from negative to positive at **T ~ 1200 K.**

- ΔG for $HgCl_2$ + O– → $HgCl_2$- monotonically **decreases** between 298 and 2000 K, always remaining negative.

- ΔG for $HgCl_2$ + O_2– → $HgCl_2$•O_2- monotonically **increases** between 298 and 2000 K. At **T > 1200 K**, ΔG changes sign from negative to positive

- ΔG for $HgCl_2$ + CO_3– → $HgCl_2$•CO_3– monotonically **increases** between 298 and 2000 K. At **T > 700 K**, ΔG changes sign from **negative to positive**

- ΔG for $HgCl_2$ + CO_3– → $HgCl_2$•O– + CO_2 monotonically **decreases** between 298 and 2000 K. ΔG changes is **positive** at all temperatures.

- ΔG for $HgCl_2 + CO_2{\bullet}O_2^- \rightarrow HgCl_2{\bullet}(CO_2{\bullet}O_2^-)$ monotonically **increases** between 298 and 2000 K. At **T > 600 K** , ΔG changes sign from **negative to positive**

- ΔG for $HgCl_2 + CO_2{\bullet}O_2^- \rightarrow HgCl_2{\bullet}O_2^- + CO_2$ monotonically **decreases** between 298 and 2000 K. ΔG is **negative** at all temperatures.

According to our mechanism, the only reaction forming $HgCl_2{\bullet}CO_3^-$ is $HgCl_2 + CO_3^-$. However, at T > 700 K the complex $HgCl_2{\bullet}CO_3^-$ becomes unstable and decomposes into $HgCl_2{\bullet}O^- + CO_2$. Since $T_{\text{drift-tube}}$ = 665 K, then $HgCl_2{\bullet}CO_3$- can spontaneously form up until the pinhole region where the effective temperature is 1914 K. Similarly, $HgCl_2{\bullet}(CO_2{\bullet}O_2^-)$ likely forms directly in a reaction between $HgCl_2 + CO_2{\bullet}O_2^-$. For this reaction ΔG_{rxn} changes sign at T > 600 K, which is lower than the effective temperature in the drift tube. It is likely that any $HgCl_2{\bullet}(CO_2{\bullet}O_2^-)$ is either dissociating back into $HgCl_2 + CO_2{\bullet}O_2$- or being converted into something else as it travels throughout the drift tube, such as $HgCl_2{\bullet}O_2^-$. The reaction of $HgCl_2$ and $CO_2{\bullet}O_2^-$ can lead to $HgCl_2{\bullet}O_2^-$. Since the Gibbs energy of reaction for $HgCl_2 + CO_2{\bullet}O_2^- \rightarrow HgCl_2{\bullet}O_2^- + CO_2$ is negative at all temperatures studied, it is more likely that the dominant product for a reaction between $HgCl_2$ and $CO_2{\bullet}O_2^-$ will be $HgCl_2{\bullet}O_2^-$. In the pinhole region, a significant fraction of $HgCl_2{\bullet}CO_3^-$ and $HgCl_2{\bullet}(CO_2{\bullet}O_2^-)$ can dissociate. The presence of a strong electric field can also decompose $HgCl_2{\bullet}O^-$ and $HgCl_2{\bullet}O_2^-$ into $HgCl_2$ + O- and $HgCl_2 + O_2^-$, respectively.

4.3.6 Reaction $HgCl_2$ + $HNO_3 \bullet NO_3^-$

Corona discharge in the HNO_3 + N_2 gas mixture produces NO_3^-, $NO_3 \bullet HNO_3^-$, and $NO_3 \bullet (HNO_3)_2^-$ ions, identified by the peaks at 62, 125, and 189 amu, respectively (Figure 4a). The ratio of signal intensities depends on the concentration of HNO_3 and corona discharge voltage. At lower HNO_3 concentrations and higher voltages, there is less clustering with HNO_3 and NO_2^- may become the dominant ion.

The formation of NO_3^- and $NO_3 \bullet HNO_3^-$ starting from HNO_3 can be explained via the mechanism in Table 4a. HNO_3 is first ionized to NO_2^-, which subsequently reacts with another HNO_3 molecule forming NO_3^- and HNO_2. Nitrate ion NO_3^- can cluster with HNO_3 to form $NO_3 \bullet HNO_3^-$ and then further to form $NO_3 \bullet (HNO_3)_n^-$. The difference in the peaks observed in Figure 4.8a can be explained as follows. Increasing the HNO_3 concentration can drive reactions $NO_2^- + HNO_3 \rightarrow NO_3^- + HNO_2$, $HNO_3 + NO_3^- \rightarrow NO_3 \bullet HNO_3^-$, $NO_3 \bullet (HNO_3)_{n-1}^- + HNO_3 \rightarrow NO_3 \bullet (HNO_3)_n^-$ forward leading to increased $NO_3 \bullet (HNO_3)_n^-$ clusters. At high electric field strengths $NO_3 \bullet HNO_3^-$ can dissociate back to HNO_3 and NO_3^- since the NO_3–HNO_3^- bond strength is on the order of 30 kcal/mol. Therefore, in order to have more $NO_3 \bullet (HNO_3)_n^-$ clusters, a certain combination of electric field and HNO_3 concentration must be maintained. In most of the experiments, the field and HNO_3 concentration were adjusted to have $NO_3 \bullet HNO_3^-$ as the major reagent ion because it is unaffected by abundant water vapor and oxidized organics, unlike NO_3^-.

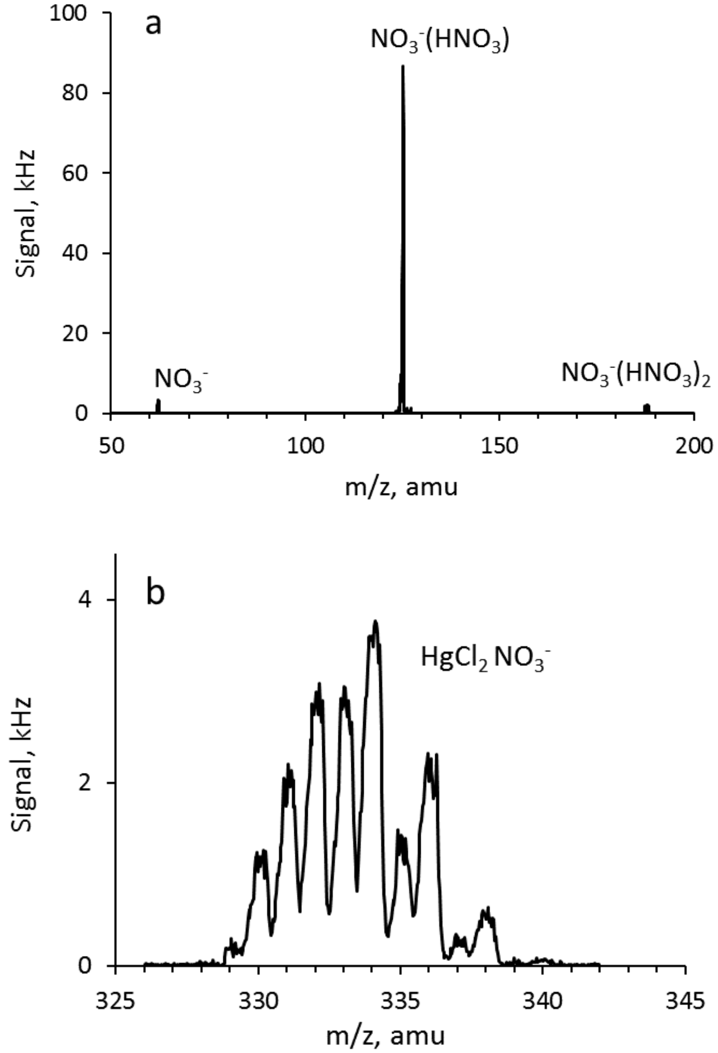

Figure 4.8 Mass spectra of (a) reagent ions generated through corona discharge in HNO_3/N_2 and (b) corresponding ion products generated in reactions with $HgCl_2$. The displayed mass spectrum of reagent ions was obtained using a lower multiplier voltage to extend the multiplier lifespan.

Table 4.4a Reaction enthalpies of the formation of NO_2–, NO_3– and NO_3•HNO_3– from corona discharge of HNO_3, calculated at three different theory levels at 298K .

Reaction	**ΔH_{rxn} (298K) (kcal/mol)**			**k_{ADO} (10^{-10} cm^3 $molecule^{-1}$ s^{-1})**
	M06-2X/ AVTZ	**PBE0/ AVTZ**	**CCSD(T)/AVTZ// M06-2X/AVTZ**	**M06-2X/ AVTZ**
HNO_3 + e– → NO_2– + OH				
NO_2– + HNO_3 → NO_3– + HNO_2	-16.98	-15.25		
HNO_3 + NO_3– → NO_3•HNO_3–	-32.62	-31.42		
NO_3•$(HNO_3)_{n-1}$– + HNO_3 → NO_3•$(HNO_3)_n$–				

Note: The mechanism is taken from Wlodeck, Luczynski, and Wincel
Source: [91].

Figure 4.8b shows that the only product ion formed in the reaction of HgCl2 with NO3- and HNO3*NO3- is$HgCl_2$•NO_3^-, identified by the peaks between 328 and 338 amu. When the concentration of HNO3 is low, NO_2– becomes the major reagent ion and it reacts with HgCl2 to form HgCl2*NO2-. Like NO3-, NO2- is subject to hydration. Table 4b shows reaction enthalpies for the formation of $HgCl_2$•NO_2^- and $HgCl_2$•NO_3^-. These reactions are exothermic, with M06-2X calculations being the most exothermic compared to PBE0 and CCSD(T). The reaction of $HgCl_2$ with NO_3•HNO_3- is endothermic according to DFT calculations but exothermic according to the CCSD(T)/AVTZ//M06-2X/AVTZ calculation.

Table 4.4b Reaction enthalpies of the formation of $HgCl_2$•NO_2^- and $HgCl_2$•NO_3 in kcal/mol calculated at three different theory levels at 298K

Reaction	**ΔH$_{rxn}$ (298K) (kcal/mol)**			**k_{ADO} (10^{-10} cm^3 molecule^{-1} s^{-1})**
	M06-2X/ AVTZ	**PBE0/ AVTZ**	**CCSD(T)/AVTZ// M06-2X/AVTZ**	**M06-2X/ AVTZ**
$HgCl_2$ + NO_3– →$HgCl_2$•NO_3–	-32.38	-27.25	-31.73	7.84
$HgCl_2$ + NO_3•HNO_3– → $HgCl_2$•NO_3^-– + HNO_3	0.24	3.91	-1.00	

According to our calculations, $HgCl_2$•NO_3- can form via direct reactions with NO_3- and NO_3^-•HNO_3. Of the reagent ions used in this study, NO_3•HNO_3^- has the potential to be the most practical. NO_3– efficiently clusters with water and highly oxygenated molecules[89] which could lower the reaction rate with $HgCl_2$. On the other hand, NO_3•HNO_3– reacts only with acidic species such as H_2SO_4, CH_3SO_3H (methanesulfonic acid), and $CH_2(COOH)_2$ (malonic acid) which are rarely present in significant concentrations[89].

4.4 Conclusions

Ion-molecule reactions relevant to the detection of GOM using ID-CIMS were investigating. A potential pathway forming $HgCl_2$•F- starting from reagent ion SF_6- was elucidated based on thermodynamic and kinetic considerations. $HgCl_2$•F- forms via a one-step mechanism via a reaction between $HgCl_2$ and SF_6–. Reactions of $HgCl_2$ from reagent ions CO_3– and CO_2•O_2– show the formation of several product ions $HgCl_2$•O–, $HgCl_2$•O_2–, $HgCl_2$•CO_3–, and $HgCl_2$•(CO_2•O_2–). $HgCl_2$•O–, $HgCl_2$•O_2– form from reactions with O– and O_2–, respectively. $HgCl_2$•CO_3–, and $HgCl_2$•(CO_2•O_2–). form from reactions with CO_3– and CO_2•O_2–, respectively. Due to the electric field in the drift tube and pin-hole regions, the effective temperatures are 655 K and 1933 K, respectively. This can decompose the product ions form, such as $HgCl_2$•(CO_2•O_2–) going into $HgCl_2$ + CO_2•O_2–. $HgCl_2$•NO_2– can form directly from reactions with NO_2–. $HgCl_2$•NO_3– can form either from NO_3– or from NO_3•HNO_3–.

For the atmospheric detection of GOM, consideration of the complex matrix of ambient air must be taken into account. Matrix effects could be considered as reactions with water (effect of relative humidity) as well as competition for the reagent ion among other trace species. Here, NO_3•HNO_3^- can be a useful reagent ion as it is unreactive with many other trace species. This question will be addressed in detail in a future work that will also include other reagent ions such as Cl_n^-, SO_2Cl^-, and I_n^- and other GOM species such as $HgBr_2$, BrHgOH, and ClHgOH. For instance, it is expected that iodide and its clusters do not react with HNO_3, NO_2, and O_3. Prior computational studies have shown that I_n^- is also insensitive to NO_x, SO_x, and H_2O, potentially making it an ideal reagent ion[44, 83].

APPENDIX A

ADDENDUM TO CHAPTER 3

This appendix provides the following additions to Chapter 3.

- Summary of the (ΔE_{CV}), scalar relativistic effects (ΔE_{SR}), spin-orbit coupling corrections (ΔE_{SO}), and the Lamb shift (ΔE_{Lamb}) corrections

- **Table A.1** Bond Dissociation Energies (BDE) at 298K in kcal/mol Determined from Calculated $E_{CBS}(2,3,4)$ Heats of Formation. Reference Values are in Parenthesis.

- **Table A.2** Heats of Formation at 298K for HgOH, HgOBr and HgOCl Calculated from Work Reactions using DFT (M06-2X/AVTZ) and Single Point CCSD(T)/DFT Calculations Extrapolated to the Complete Basis Set Limit ($E_{CBS}(2,3,4)$) using a Mixed Gaussian-Exponential extrapolation with AVDZ, AVTZ, and AVQZ Basis Sets.

- **Table A.3** Heats of Formation at 298K for CH_3OBr Calculated from Work Reactions using DFT (M06-2X/AVTZ) and Single Point CCSD(T)/DFT Calculations Extrapolated to the Complete Basis Set Limit ($E_{CBS}(2,3,4)$) using a Mixed Gaussian-Exponential extrapolation with AVDZ, AVTZ, and AVQZ Basis Sets.

- **Table A.4** Heats of Formation at 298K for HgF_2, $HgCl_2$, $HgBr_2$, and HgI_2 Calculated from Work Reactions using DFT (M06-2X/AVTZ) and Single Point CCSD(T)/DFT Calculations Extrapolated to the Complete Basis Set Limit (ECBS(2,3,4)) using a Mixed Gaussian-Exponential extrapolation with AVDZ, AVTZ, and AVQZ Basis Sets.

- **Table A.5** Molecular Properties for BrHgOBr, BrHgOCl, ClHgOBr, ClHgOCl, FHgOBr, and FHgOCl from M06-2X/AVTZ Calculations.

- **Table A.6** Molecular Properties for HgOBr, HgOCl, $Hg(OH)_2$, and HgOH from M06-2X/AVTZ Calculations.

- **Table A.7** Molecular Properties for ClHgOH, FHgOH, IHgOH, and BrHgOH from M06-2X/AVTZ Calculations.

- **Table A.8** Molecular Properties for HOHgOBr, HOHgOCl, IHgOBr, and IHgOCl from M06-2X/AVTZ Calculations.

Corrections to the CBS energies from Peterson and co-workers.

ΔE_{cv} was calculated as the difference in energy between a CCSD(T) calculation with core-valence electrons correlated and one calculation at the same level of theory using the frozen-core approximation. For the ΔE_{CV} calculations the aug-cc-p*w*CVTZ (**c**orrelation **c**onsistent **p**olarized ***weighted*** **c**ore–**v**alence basis sets **aug**mented with diffuse functions) basis sets, including a PP for Br and Hg, were used. The aug-cc-p*w*CVTZ basis sets were constructed by adding sets of primitive Gaussian functions to the aug-cc-pVTZ basis sets explicitly optimized for core-valence correlations using singles and doubles configuration interaction (CISD) calculations weighted by a factor designed for converging the core-core contribution and speeding up the core-valence contribution to the correlation energy compared to the aug-cc-pCVTZ basis sets [1]. An additional correction to the core-valence correlation (ΔE_{CV-f}) was considered because of the inclusion of the $4f^{14}$ electrons in the PP that are energetically above the 4th shell of the core electrons (electron configuration of Hg is $1s^2\,2s^22p^6\,3s^33p^63d^{10}\,4s^24p^64d^{10}\,5s^25p^64f^{14}5d^{10}\,6s^2$). The ΔE_{CV-f} correction was calculated as the difference between a pair of non-relativistic all electron CCSD(T) calculations where the valence and outer core electrons were correlated and a calculation where the $4f^{14}$ electrons were included in the correlation treatment. These calculations were carried out with an all-electron core-valance correlation consistent basis set optimized using all-electron CCSD(T) calculation with a Douglas-Kroll-Hess Hamiltonian (CCSD(T)-DK; basis set is denoted as aug-cc-pwCVTZ-DK or AVTZ-DK).

- ΔE_{SR} corrections, arising from the dependence of the electron mass on the velocity (mass-velocity correction) and the high-frequency oscillations of an electron around its mean position (Darwin correction), were calculated as the sum of the expectation values from the mass-velocity and Darwin terms of the Breit-Pauli Hamilitonian calculated using the CISD method using uncontracted aVTZ basis sets.

- Spin-orbit coupling (ΔE_{SO}) effects, arising from interactions between an electron's spin and the magnetic moment produced from the motion of the electrons about the nucleus, were calculated out using multireference configuration interactions (MRCI) using standard full valence active spaces and the AVTZ basis sets. The ΔE_{SO} correction was calculated as the difference between an MRCI calculation including the spin orbit operator in the Hamiltonian (SO-MRCI) and a MRCI calculation without the SO operator.
- The final correction for the lamb shift, ΔE_{Lamb} is a quantum electrodynamic effect (QED) decreasing the attractive force between the nucleus and electrons to due quantum mechanical electromagnetic field fluctuations when they electrons are very close to the nucleus [2]. Because of the decreased attractions, electrons closer to the nucleus (i.e., $2s_{1/2}$ subshell) can be slightly higher in energy than electrons further away (i.e., $2p_{1/2}$ subshell). For heavy atoms such as Hg, these effects can become more pronounced[3]. The lamb shift correction (only calculated for OHgI) was determined from a series of Gaussian functions[4] used to describe the self-energy and vacuum polarization terms calculated from a second order CCSD(T)-DK2/AVTZ-DK calculation carried out at the equilibrium geometry[5].

Table A.1 Bond Dissociation Energies (BDE) at 298K in kcal/mol Determined from Calculated $E_{CBS}(2,3,4)$ Heats of Formation. Reference Values are in Parenthesis

XHgY	**BDE(XHg + Y)**	**BDE(X + HgY)**
OHgF	91.69	60.3
OHgCl	81.0 (79.7[a])	60.5 (62.2[a])
OHgBr	70.7 (70.4[a])	58.7 (59.7[a])
OHgI	60.5 (62.2[b])	56.9 (58.0[b])
FHgOH	92.5	74.3
ClHgOH	75.3	65.2
BrHgOH	75.0	73.2
IHgOH	65.2	71.7
$Hg(OH)_2$	76.9	
HOHgOCl	55.0	69.9
HOHgOBr	56.2	70.5
FHgOCl	51.2	51.9
ClHgOCl	52.5	56.2
BrHgOCl	51.4 (51.4[c])	68.7
IHgOCl	52.2	61.2
FHgOBr	56.1	49.4
ClHgOBr	53.3	49.5
BrHgOBr	52.83 (53.8[c])	69.5
IHgOBr	52.78	61.3

[a] From Balabanov and Peterson, value at 0 K[69]. [b] From Shepler et al., value at 0 K from [68]. [c] From Jiao and Dibble, value at 298K[59].

Table A.2 Heats of Formation at 298K for HgOH, HgOBr and HgOCl Calculated from Work Reactions using DFT (M06-2X/AVTZ) and Single Point CCSD(T)/DFT Calculations Extrapolated to the Complete Basis Set Limit (E_{CBS}(2,3,4)) using a Mixed Gaussian-Exponential extrapolation with AVDZ, AVTZ, and AVQZ Basis Sets

Work Reaction	**M06-2X/ AVTZ**	**E_{CBS}(2,3,4)**
	ΔH_F (298K) (kcal/mol)	
HgOH + HCl → HgCl + H_2O	11.69	9.76
HgOH + HBr → HgBr + H_2O	12.00	11.41
HgOH + HF → HgF + H_2O	12.26	9.9
HgOH + CH_3F → HgF + CH_3OH	11.68	9.57
HgOH + CH_3Cl → HgCl + CH_3OH	11.7	9.63
HgOH + CH_3Br → HgBr + CH_3OH	12.42	9.00
AVG/STDEV	**11.96 +/- 0.32**	**9.87 +/- 0.81**
HgOBr + CH_3OH → HgOH + CH_3OBr	45.06	44.96
HgOBr + $HgCl_2$ → HgCl + ClHgOBr	43.37	44.47
HgOBr + $HgBr_2$ → HgBr + BrHgOBr	42.27	43.81
AVG/STDEV	**43.57 +/- 1.40**	**44.41 +/- 0.57**
HgOCl + CH3OH → HgOH + CH_3OCl	40.32	39.45
HgOCl + $HgCl_2$ → HgCl + ClHgOCl	40.18	40.16
HgOCl + $HgBr_2$ → HgBr + BrHgOCl	39.25	39.58
AVG/STDEV	**39.91 +/- 0.58**	**39.73 +/- 0.38**

Table A.3 Heats of Formation at 298K for CH_3OBr Calculated from Work Reactions using DFT (M06-2X/AVTZ) and Single Point CCSD(T)/DFT Calculations Extrapolated to the Complete Basis Set Limit (E_{CBS}(2,3,4)) using a Mixed Gaussian-Exponential extrapolation with AVDZ, AVTZ, and AVQZ Basis Sets

Work Reaction	**M06-2X/ AVTZ**	**E_{CBS}(2,3,4)**
	ΔH_F (298K) (kcal/mol)	
CH_3OBr + H_2O → CH_3OH + HOBr	-11.44	-11.15
CH_3OBr + H_2 → CH_4 + HOBr	-14.21	-11.01
CH_3OBr + H_2 → CH_3OH + HBr	-13.81	-10.71
CH_3OBr + CH_4 → CH_3OH + CH_3Br	-12.06	-9.77
AVG/STDEV	**-12.88 +/- 1.34**	**-10.66 +/- 0.62**

Table A.4 $\Delta Hf(298)$ HgF_2, $HgCl_2$, $HgBr_2$, and HgI_2 Calculated Work Reactions using DFT (M06-2X/AVTZ) and Single Point CCSD(T)/DFT Calculations Extrapolated to the Complete Basis Set Limit ($E_{CBS}(2,3,4)$) using a Mixed Gaussian-Exponential Extrapolation with AVDZ, AVTZ, and AVQZ Basis Sets

Work Reaction	**M06-2X/ AVTZ**	**ECBS(2,3,4)**
	ΔH_F (298K) (kcal/mol)	
HgF_2 + HOHgOCl → FHgOCl + FHgOH	-68.87	-68.94
HgF_2 + HOHgOBr → FHgOBr + FHgOH	-72.33	-72.48
HgF_2 + $Hg(OH)_2$ → FHgOH + FHgOH	-70.05	-70.21
Literature value, -70.18 [19]		
AVG/STD	**-70/42 +/- 1.76**	**-70.54 +/- 1.79**
$HgCl_2$ + HOHgOCl → ClHgOCl + ClHgOH	-25.77	-35.09
$HgCl_2$ + HOHgOBr → ClHgOBr + ClHgOH	-25.68	-35.08
$HgCl_2$ + $Hg(OH)_2$ → ClHgOH + ClHgOH	-16.21	-35.15
Literature value, -34.96 [19]		
AVG/STD	**-22.56 +/- 5.49**	**-35.11 +/- 0.04**
$HgBr_2$ + HOHgOCl → BrHgOCl + BrHgOH	-21.56	-20.87
$HgBr_2$ + HOHgOBr → BrHgOBr + BrHgOH	-21.6	-20.89
$HgBr_2$ + $Hg(OH)_2$ → BrHgOH + BrHgOH	-21.64	-21.16
Literature value, -20.42 [19]		
AVG/STD	**-21.60 +/- 0.04**	**-20.97 +/- 0.16**
HgI_2 + HOHgOCl → IHgOCl + IHgOH	-4.72	-9.33
HgI_2 + HOHgOBr → IHgOBr + IHgOH	-3.93	-8.53
HgI_2 + Hg(OH)2 → IHgOH + IHgOH	-1.54	-6.45
Literature value, -3.86 [19]		
AVG/STD	**-3.40 +/- 1.66**	**-8.10 +/- 1.49**

Table A.5 Molecular Properties for BrHgOBr, BrHgOCl, ClHgOBr, ClHgOCl, FHgOBr, and FHgOCl from M06-2X/AVTZ Calculations

BrHgOBr			
Cartesian Coordinates			
Hg	0.281045	0.272024	-0
O	-1.61974	0.921702	0.0
Br	-2.84143	-0.42606	0
Br	2.56927	-0.40639	0
Frequencies (cm-1)			
1	49.1192		
2	115.8267		
3	127.0928		
4	253.8606		
5	500.0135		
6	738.4763		
Rotational Constants (GHz)			
9.05180	0.41567	0.39742	

BrHgOCl			
Cartesian Coordinates			
Hg	-0.11459	-0.19847	0
O	-2.06969	-0.68327	0
Cl	-3.06136	0.67429	0
Br	2.221933	0.28234	0
Frequencies (cm-1)			
1	59.318		
2	115.2097		
3	168.4646		
4	256.3543		
5	523.6929		
6	814.0009		
Rotational Constants (GHz)			
13.47638	0.64126	0.61213	

ClHgOBr			
Cartesian Coordinates			
Hg	-0.63629	0.174364	0
O	1.209739	0.940796	0
Br	2.519621	-0.32214	0
Cl	-2.76245	-0.60004	0
Frequencies (cm-1)			
1	60.9704		
2	129.1574		
3	137.2385		
4	371.7622		
5	505.579		
6	742.5725		
Rotational Constants (GHz)			
12.35429	0.57888	0.55297	

ClHgOCl			
Cartesian Coordinates			
Hg	0.237185	0.139735	0
O	-1.67438	0.74066	-0
Cl	-2.74775	-0.55387	0
Cl	2.419529	-0.45226	-0
Frequencies (cm-1)			
1	72.0937		
2	131.8611		
3	177.647		
4	373.7149		
5	532.4379		
6	816.363		
Rotational Constants (GHz)			
16.56469	0.96333	0.91038	

FHgOBr			
Cartesian Coordinates			
Hg	-0.8259	0.07895	0
O	0.9457	0.9493	0
Br	2.34006	-0.2205	0
F	-2.5991	-0.688	0
Frequencies (cm-1)			
1	85.0978		
2	166.634		
3	170.207		
4	514.275		
5	621.511		
6	752.593		
Rotational Constants (GHz)			
17.75865	0.71003	0.68273	

FHgOCl			
Cartesian Coordinates			
Hg	-0.4337	0.06982	0
O	1.4055	0.79947	0
Cl	2.57555	-0.4092	0
F	-2.2592	-0.5583	0
Frequencies (cm-1)			
1	97.2344		
2	168.007		
3	200.949		
4	536.276		
5	625.694		
6	818.526		
Rotational Constants (GHz)			
22.00254	1.27193	1.20242	

Table A.6 Molecular Properties for HgOBr, HgOCl, $Hg(OH)_2$, and HgOH from M06-2X/AVTZ Calculations

HgOBr

Cartesian Coordinates

Hg	0	1.08447	0
O	0.93518	-0.897	0
Br	-0.2138	-2.2738	0

Frequencies (cm-1)

1	85.8185
2	306.067
3	661.882

Rotational Constants (GHz)

30.44992	0.76893	0.74999

HgOCl

Cartesian Coordinates

Hg	0	0.68039	
O	0.79732	-1.3862	
Cl	-0.3752	-2.5495	

Frequencies (cm-1)

1	109.582
2	295.052
3	756.477

Rotational Constants (GHz)

35.23442	1.44566	1.38868

$Hg(OH)_2$

Cartesian Coordinates

Hg	0	0.00089	0
O	-1.9613	-0.0731	0.08063
O	1.96134	-0.0731	-0.0806
H	-2.3499	0.54942	-0.5384
H	2.3499	0.54938	0.53841

Frequencies (cm-1)

1	151.974
2	180.123
3	189.493
4	588.9
5	646.172
6	926.311
7	934.812
8	3900.53
9	3902.02

Rotational Constants (GHz)

332.46539	3.74403	3.74320

HgOH

Cartesian Coordinates

Hg	0.0104	-0.2155	0
O	0.0104	1.88518	0
H	-0.9156	2.15497	0

Frequencies (cm-1)

1	427.995
2	822.349
3	3848.18

Rotational Constants (GHz)

632.36696	7.17980	7.09919

Table A.8 Molecular Properties for ClHgOH, FHgOH, IHgOH, and BrHgOH from M06-2X/AVTZ Calculations

ClHgOH			
Cartesian Coordinates			
Hg	-0.1932	0.00025	0
Cl	2.07681	0.0036	0
O	-2.1626	-0.1068	0
H	-2.5482	0.77318	0
Frequencies (cm-1)			
1	137.654		
2	138.545		
3	368.417		
4	611.817		
5	925.487		
6	3895.49		
Rotational Constants (GHz)			
658.78758	2.10858	2.10185	

FHgOH			
Cartesian Coordinates			
Hg	0.00486	0.00092	0
F	1.94269	0.00433	0
O	-1.9433	-0.1104	0
H	-2.3267	0.77049	0
Frequencies (cm-1)			
1	175.299		
2	177.181		
3	587.848		
4	654.087		
5	960.363		
6	3894.95		
Rotational Constants (GHz)			
658.07280	3.67539	3.65497	

IHgOH			
Cartesian Coordinates			
Hg	-0.8262	0.00026	0
I	1.73218	0.00107	0
O	-2.8137	-0.1063	0
H	-3.2013	0.77268	0
Frequencies (cm-1)			
1	112.718		
2	114.839		
3	197.646		
4	589.582		
5	894.887		
6	3896.15		
Rotational Constants (GHz)			
655.01273	0.77096	0.77005	

BrHgOH			
Cartesian Coordinates			
Hg	-0.5291	-5E-05	0
Br	1.865	0.002	0
O	-2.507	-0.1052	0
H	-2.8914	0.77528	0
Frequencies (cm-1)			
1	121.793		
2	123.046		
3	249.243		
4	601.527		
5	912.379		
6	3895.38		
Rotational Constants (GHz)			
656.70122	1.14865	1.14665	

Table A.9 Molecular Properties for HOHgOBr, HOHgOCl, IHgOBr, and IHgOCl from M06-2X/AVTZ Calculations

HOHgOBr

Cartesian Coordinates

Hg	0.82596	0.08274	0.00062
O	-0.9648	0.94853	0.00673
Br	-2.3527	-0.2264	-7E-05
O	2.62634	-0.6801	-0.109
H	2.97649	-0.8413	0.77099

Frequencies (cm-1)

1	83.817
2	132.016
3	170.324
4	171.165
5	504.877
6	626.47
7	747.051
8	941.619
9	3894.6

Rotational Constants (GHz)

17.70319	0.71248	0.68634

HOHgOCl

Cartesian Coordinates

Hg	-0.4314	0.07368	0.000911
O	1.42701	0.79636	0.010641
Cl	2.58793	-0.4204	-0.002304
O	-2.2844	-0.5463	-0.110505
H	-2.6243	-0.7482	0.765233

Frequencies (cm-1)

1	61.6185
2	100.847
3	169.256
4	201.67
5	526.156
6	631.021
7	815.262
8	942.245
9	3894.94

Rotational Constants (GHz)

21.55641	1.27957	1.21228

IHgOBr

Cartesian Coordinates

Hg	-0.0403	0.32848	0
O	-1.9777	0.90304	-0
Br	-3.1378	-0.4967	0
I	2.43155	-0.3042	0

Frequencies (cm-1)

1	43.2632
2	108.587
3	119.351
4	203.553
5	490.418
6	730.614

Rotational Constants (GHz)

7.65523	0.31802	0.30533

IHgOCl

Cartesian Coordinates

Hg	-0.4283	-0.2259	0
O	-2.4105	-0.6468	0
Cl	-3.3555	0.74282	0
I	2.08661	0.20037	0

Frequencies (cm-1)

1	52.9763
2	103.765
3	157.079
4	207.086
5	510.682
6	810.93

Rotational Constants (GHz)

12.25902	0.47011	0.45275

APPENDIX B

ADDENDUM TO CHAPTER 4

This appendix provides the following additions to Chapter 4.

- Comparison of stick spectrum and experimental measurements for $HgCl_2$•F–, $HgCl_2$•O–, $HgCl_2$•O_2–, $HgCl_2$•CO_3–, and $HgCl_2$•(CO_2•O_2–)n $HgCl_2$•NO_2^- and $HgCl_2$•NO_3.
- Cartesian coordinates, charge, and multiplicities for $HgCl_2$•F–, $HgCl_2$•O–, $HgCl_2$•O_2–, $HgCl_2$•CO_3–, and $HgCl_2$•(CO_2•O_2–)n $HgCl_2$•NO_2^- and $HgCl_2$•NO_3.

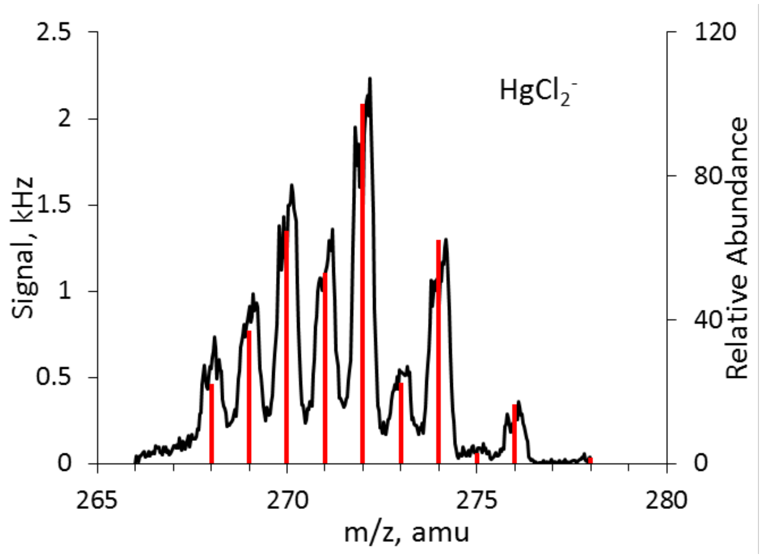

Figure B.1 Mass spectra of $HgCl_2^-$. The stick spectrum was calculated using isotope ratios of mercury and chlorine.

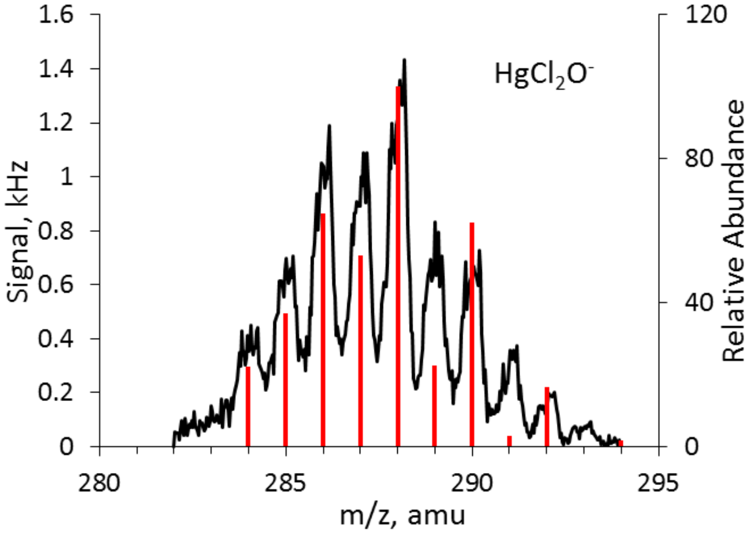

Figure B.2 Mass spectra of HgCl$_2$O$^-$. The stick spectrum was calculated using isotope ratios of mercury, chlorine, and oxygen.

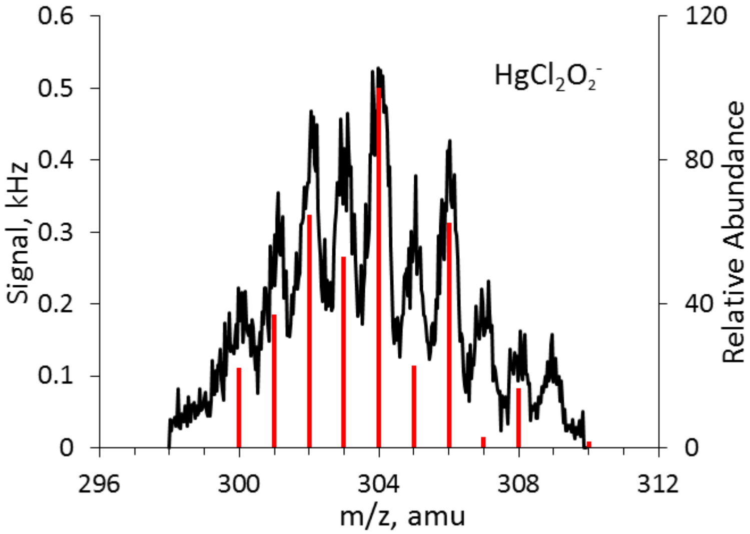

Figure B.3 Mass spectra of HgCl$_2$O$_2^-$. The stick spectrum was calculated using isotope ratios of mercury, chlorine, and oxygen.

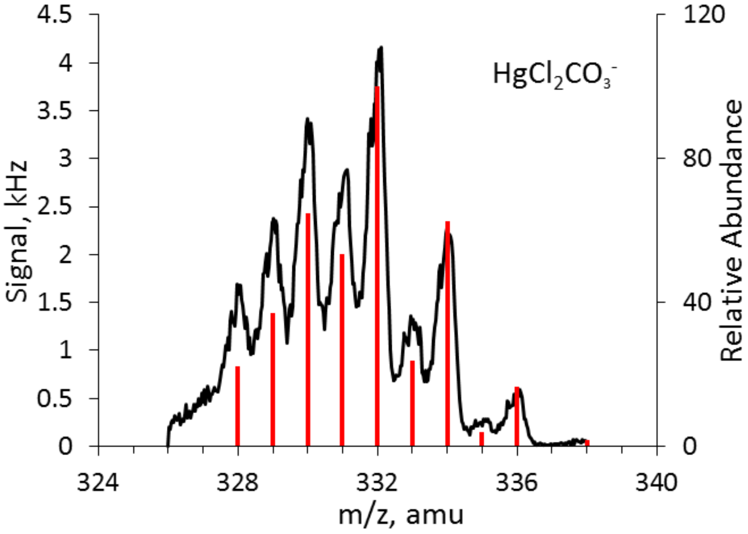

Figure B.4 Mass spectra of HgCl$_2$CO$_3^-$. The stick spectrum was calculated using isotope ratios of mercury, chlorine, oxygen, and carbon.

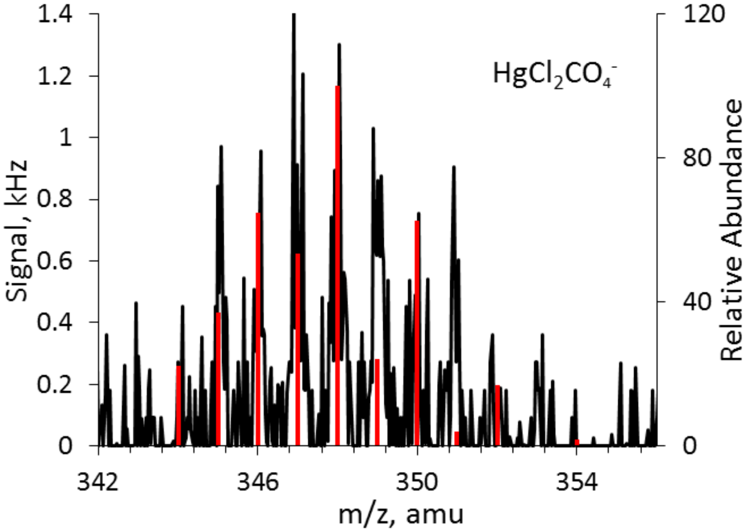

Figure B.5 Mass spectra of HgCl$_2$CO$_4^-$. The stick spectrum was calculated using isotope ratios of mercury, chlorine, oxygen, and carbon.

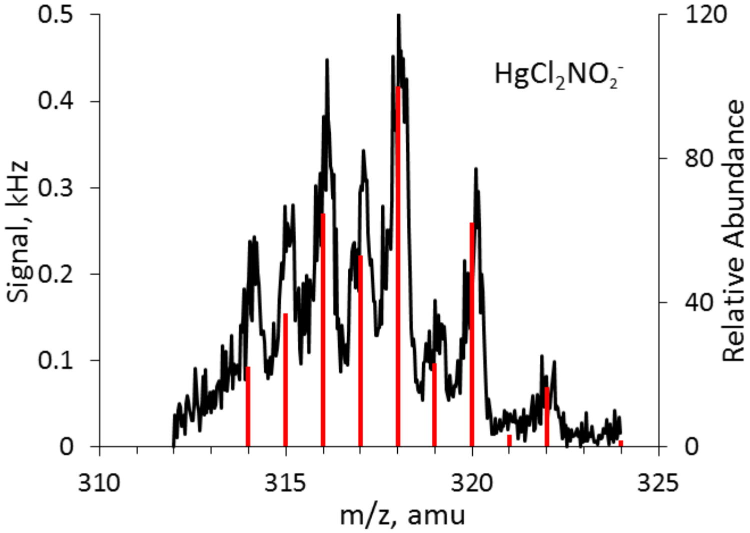

Figure B.6 Mass spectra of HgCl$_2$NO$_2^-$. The stick spectrum was calculated using isotope ratios of mercury, chlorine, oxygen, and nitrogen.

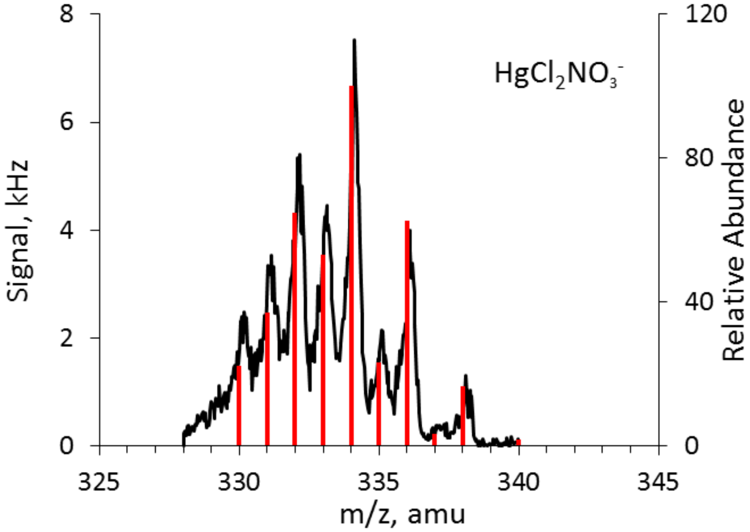

Figure B.7 Mass spectra of HgCl$_2$NO$_3^-$. The stick spectrum was calculated using isotope ratios of mercury, chlorine, oxygen, and nitrogen.

Table B.1 Charge, multiplicity and Cartesian coordinates for $HgCl_2•F^-$

$HgCl_2•F^-$			
Charge	-1		
Multiplicity	1		
Geometry in Cartesian Coordinates (X, Y, Z)			
Hg	0.05819	0	0.02956
Cl	-0.0569	0	2.4723
Cl	2.11891	0	-1.284
F	-1.7651	0	-1.0128

Table B.2 Charge, multiplicity and Cartesian coordinates for $HgCl_2•O^-$

$HgCl_2•O^-$			
Charge	-1		
Multiplicity	2		
Geometry in Cartesian Coordinates (X, Y, Z)			
Hg	0	0	0.06451
Cl	0	-2.274	-0.6788
Cl	0	2.27401	-0.6788
O	0	0	2.23995

Table B.3 Charge, multiplicity and Cartesian coordinates for $HgCl_2•O_2^-$

$HgCl_2•O_2^-$.			
Charge	-1		
Multiplicity	2		
Geometry in Cartesian Coordinates (X, Y, Z)			
Hg	0.0846	-0.0002	0.02145
Cl	-0.1264	0.00029	2.42337
Cl	1.79265	-0.0014	-1.6504
O	-2.0343	0.00115	-0.6764
O	-2.1598	0.0009	-1.9915

Table B.4 Charge, multiplicity and Cartesian coordinates for $HgCl_2 \bullet CO_3^-$

$HgCl_2 \bullet CO_3^-$			
Charge	-1		
Multiplicity	2		
Geometry in Cartesian Coordinates (X, Y, Z)			
Hg	0.02868	-0.0001	0.0107
Cl	-0.0834	-2E-05	2.38332
Cl	1.30033	0.00015	-1.996
O	-2.1397	1.11928	-0.6793
C	-2.6647	-0.001	-0.847
O	-2.139	-1.121	-0.6791
O	-3.92	-0.0014	-1.2479

Table B.5 Charge, multiplicity and Cartesian coordinates for $HgCl_2 \bullet CO_4^-$

$HgCl_2 \bullet CO_4^-$			
Charge	-1		
Multiplicity	2		
Geometry in Cartesian Coordinates (X, Y, Z)			
Hg	-0.6731	7E-06	0.03082
Cl	-1.1501	2.30182	-0.1195
Cl	-1.1502	-2.3018	-0.1195
O	1.36738	-4E-05	1.33969
C	2.40703	-4E-05	0.67158
O	3.58623	-4E-05	0.85474
O	1.95399	-3E-05	-0.8152
O	2.90676	-1E-05	-1.6833

Table B.6 Charge, multiplicity and Cartesian coordinates for $HgCl_2•NO_2^-$

	$HgCl_2•NO_2^-$		
Charge	-1		
Multiplicity	1		
Geometry in Cartesian Coordinates (X, Y, Z)			
Hg	0.01149	-0.1847	0
Cl	2.30319	-0.9653	0
Cl	-2.1907	-1.1928	0
O	-0.1118	2.03604	1.04807
N	-0.149	2.69803	0
O	-0.1118	2.03604	-1.0481

Table B7 Charge, multiplicity and Cartesian coordinates for $HgCl_2•NO_3^-$

	$HgCl_2•NO_3^-$		
Charge	-1		
Multiplicity	1		
Geometry in Cartesian Coordinates (X, Y, Z)			
Hg	0.00794	0	0.00184
Cl	-0.0035	6E-06	2.37257
Cl	1.14151	-6E-06	-2.0801
O	-2.1918	-1.0785	-0.5633
N	-2.8211	-3E-06	-0.7262
O	-2.1918	1.07849	-0.5633
O	-4.0001	-5E-06	-1.0314

REFERENCES

1. Carpi, A., *Mercury from combustion sources: A review of the chemical species emitted and their transport in the atmosphere.* Water, Air, and Soil Pollution, 1997. **98**: p. 241-254.
2. Lindqvist, O. and Rodhe, H., *Atmospheric mercury: A review.* Tellus, 1985. **37B**.
3. Pirrone, N., et al., *Global mercury emissions to the atmosphere from anthropogenic and natural sources.* Atmospheric Chemistry and Physics, 2010. **10**(13): p. 5951-5964.
4. Council, N.R., *Assessment of mercury in the enviroment: A report*. 1978, The National Academies Press: Washington, DC.
5. Council, N.R., *Toxicological effects of methylmercury*. 2000, The National Academies Press: Washington, DC.
6. Lei, H., et al., *Projections of atmospheric mercury levels and their effect on air quality in the united states.* Atmospheric Chemistry and Physics, 2014. **14**(2): p. 783-795.
7. Subir, M., Ariya, P.A., and Dastoor, A.P., *A review of uncertainties in atmospheric modeling of mercury chemistry i. Uncertainties in existing kinetic parameters – fundamental limitations and the importance of heterogeneous chemistry.* Atmospheric Environment, 2011. **45**(32): p. 5664-5676.
8. Ullrich, S.M., Tanton, T.W., and Abdrashitova, S.A., *Mercury in the aquatic environment: A review of factors affecting methylation.* Critical Reviews in Environmental Science and Technology, 2001. **31**(3): p. 241-293.
9. Hu, H., et al., *Oxidation and methylation of dissolved elemental mercury by anaerobic bacteria.* Nature Geoscience, 2013. **6**(9): p. 751-754.
10. Mergler, D., et al., *Methylmercury exposure and health effects in humans: A worldwide concern.* AMBIO, 2007. **36**(1): p. 3-11.
11. Zhang, L., et al., *Mercury transformation and speciation in flue gases from anthropogenic emission sources: A critical review.* Atmospheric Chemistry and Physics, 2016. **16**(4): p. 2417-2433.

12. Horowitz, H.M., et al., *A new mechanism for atmospheric mercury redox chemistry: Implications for the global mercury budget.* Atmospheric Chemistry and Physics, 2017. **17**(10): p. 6353-6371.

13. Zhang, Y., et al., *Biogeochemical drivers of the fate of riverine mercury discharged to the global and arctic oceans.* Global Biogeochem. Cycles, 2015. **29**: p. 854-864.

14. Schroeder, W.H., et al., *Arctic springtime depletion of mercury.* Nature, 1998. **394**(6691): p. 331-332.

15. Steffen, A., et al., *A synthesis of atmospheric mercury depletion event chemistry in the atmosphere and snow.* Atmospheric Chemistry and Physics, 2008. **8**: p. 1445-1482.

16. Lindberg, S.E., et al., *Dynamic oxidation of gaseous mercury in the arctic troposphere at polar sunrise.* Environmental Science & Technology, 2002. **36**(6): p. 1245-1256.

17. Lin, C.-J. and Pehkonen, S.O., *The chemistry of atmospheric mercury: A review.* Atmospheric Environment, 1999. **33**: p. 2067-2079.

18. Grade, M. and Hirschwald, W., *Energetics and stabilities of the iib/via-compounds at high-temperature equilibrium conditions.* Berichte der Bunsengesellschaft für physikalische Chemie, 1982. **96**: p. 899-907.

19. Chase, M.W., Jr., *Nist-janaf themochemical tables, fourth edition.* Journal of Physical and Chemical Reference Data, 1998. **Monograph 9**: p. 1-1951.

20. Shepler, B.C. and Peterson, K.A., *Mercury monoxide: A systematic investigation of its ground electronic state.* Journal of Physical Chemistry A, 2003. **107**(11): p. 1783-1787.

21. Tossell, J.A., *Calculation of the energetics for the oligomerization of gas phase hgo and hgs and for the solvolysis of crystalline hgo and hgs.* Journal of Physical Chemistry A, 2006. **110**(7): p. 2571-2578.

22. Peterson, K.A., Shepler, B.C., and Singleton, J.M., *The group 12 metal chalcogenides: An accurate multireference configuration interaction and coupled cluster study.* Molecular Physics, 2007. **105**(9): p. 1139-1155.

23. Landis, M.S., et al., *Behavior of mercury emissions from a commercial coal-fired power plant: The relationship between stack speciation and near-field plume measurements.* Environmental Science & Technology, 2014. **48**(22): p. 13540-8.

24. Deeds, D.A., et al., *Mercury speciation in a coal-fired power plant plume: An aircraft-based study of emissions from the 3640 mw nanticoke generating station, ontario, canada.* Journal of Geophysical Research: Atmospheres, 2013. **118**(10): p. 4919-4935.

25. Peterson, C., Alishahi, M., and Gustin, M.S., *Testing the use of passive sampling systems for understanding air mercury concentrations and dry deposition across florida, USA.* Science of the Total Environment, 2012. **424**: p. 297-307.

26. Gustin, M.S., et al., *Measuring and modeling mercury in the atmosphere: A critical review.* Atmospheric Chemistry and Physics, 2015. **15**(10): p. 5697-5713.

27. Saiz-Lopez, A., et al., *Photoreduction of gaseous oxidized mercury changes global atmospheric mercury speciation, transport and deposition.* Nature Communications, 2018. **9**(1): p. 4796.

28. Whalin, L., Kim, E.-H., and Mason, R., *Factors influencing the oxidation, reduction, methylation and demethylation of mercury species in coastal waters.* Marine Chemistry, 2007. **107**(3): p. 278-294.

29. Holmes, C.D., et al., *Global atmospheric model for mercury including oxidation by bromine atoms.* Atmospheric Chemistry and Physics, 2010. **10**(24): p. 12037-12057.

30. Huang, J., et al., *A review of passive sampling systems for ambient air mercury measurements.* Environmental Science: Processes & Impacts, 2014. **16**(3): p. 374-92.

31. Dibble, T.S., Zelie, M.J., and Jiao, Y., *Quantum chemistry guide to ptrms studies of as-yet undetected products of the bromine-atom initiated oxidation of gaseous elemental mercury.* Journal of Physical Chemistry A, 2014. **118**(36): p. 7847-54.

32. de Gouw, J. and Warneke, C., *Measurements of volatile organic compounds in the earths atmosphere using proton-transfer-reaction mass spectrometry.* Mass Spectrometry Reviews 2007. **26**(2): p. 223-257.

33. Fortner, E.C., Zhao, J., and Zhang, R.Y., *Development of ion drift-chemical ionization mass spectrometry.* Analytical Chemistry, 2004. **76**(18): p. 5436-5440.

34. Cao, Y., et al., *Impacts of halogen additions on mercury oxidation, in a slipstream selective catalyst reduction (scr), reactor when burning sub-bituminous coal.* Environmental Science & Technology, 2008. **42**(1): p. 256-261.

35. Auzmendi-Murua, I. and Bozzelli, J.W., *Gas phase mercury oxidation by halogens (cl, br, i) in combustion effluents: Influence of operating conditions.* Energy Fuels, 2016. **30**(1): p. 603-615.

36. Paquet, E. and Viktor, H.L., *Computational bethods for ab initio molecular dynamics.* Advances in Chemistry, 2018. **2018**: p. 14.

37. Wang, S., et al., *Active and widespread halogen chemistry in the tropical and subtropical free troposphere.* Proceedings of the National Academy of Sciences of the United States of America, 2015. **112**(30): p. 9281-6.

38. Xin Yang, et al., *Tropospheric bromine chemistry and its impacts on ozone: A model study.* Journal of Geophysical Research, 2005. **110**.

39. Schmidt, J.A., et al., *Modeling the observed tropospheric bro background: Importance of multiphase chemistry and implications for ozone, oh, and mercury.* J. Geophys Res.: Atmos., 2016. **121**(19): p. 11,819-11,835.

40. Hossaini, R., et al., *A global model of tropospheric chlorine chemistry: Organic versus inorganic sources and impact on methane oxidation.* Journal of Geophysical Research: Atmospheres, 2016. **121**(14): p. 14,271–14,297.

41. Kolker, A., Senior, C.L., and Quickm Jeffrey C, *Mercury in coal and the impact of coal quality on mercury emissions from combustion systems.* Applied Geochemistry, 2006. **21**(11): p. 1821-1836.

42. *What are the types of coal?* United States Geological Society, Washington, D. C. 2018 [cited 2018 Dec. 08]; Available from: https://www.usgs.gov/faqs/what-are-types-coal?qt-news_science_products=0#qt-news_science_products.

43. Granite, E.J., Pennline, H.W., and Senior, C.L., *Mercury control for coal-derived gas streams*. 2015, Weinheim, Germany: Wiley-VCH.

44. Auzmendi-Murua, I., Castillo, Á., and Bozzelli, J.W., *Mercury oxidation via chlorine, bromine, and iodine under atmospheric conditions: Thermochemistry and kinetics.* Journal of Physical Chemistry A, 2014. **118**(16): p. 2959-2975.

45. Reischl, M.S., *Bromine comes to the rescue for mercury power plant emissions*, in *Chemical & Engineering News*. 2015. p. 17-19.

46. Van Otten, B., et al., *Gas-phase oxidation of mercury by bromine and chlorine in flue gas.* Energy Fuels, 2011. **25**(8): p. 3530-3536.

47. Jensen, F., *Introduction to computational chemistry*. Third Edition ed. 2017, Hoboken, NJ: John Wiley & Sons.

48. Handy, N.C. and Lee, A., *The adiabatic approximation.* Chemical Physics Letters, 1996. **252**: p. 425-430.

49. Watts, J.D., Gauss, J., and Bartlett, R.J., *Coupled-cluster methods with noniterative triple excitations for restricted open-shell hartree–fock and other general single determinant reference functions. Energies and analytical gradients.* Journal of Chemical Physics, 1993. **98**(11): p. 8718-8733.

50. Peterson, K.A., Woon, D.E., and Dunning, T.H., *Benchmark calculations with correlated molecular wave functions. Iv. The classical barrier height of the* $h+h_2 \rightarrow h_2+h$ *reaction.* Journal of Chemical Physics, 1994. **100**(10): p. 7410-7415.

51. Vasilyev, V., *Online complete basis set limit extrapolation calculator.* Computational and Theoretical Chemistry, 2017. **1115**: p. 1-3.

52. Figgen, D., et al., *Energy-consistent pseudopotentials for group 11 and 12 atoms: Adjustment to multi-configuration dirac–hartree–fock data.* Chemical Physics, 2005. **311**(1-2): p. 227-244.

53. Peterson, K.A., et al., *Systematically convergent basis sets with relativistic pseudopotentials. Ii. Small-core pseudopotentials and correlation consistent basis sets for the post-d group 16–18 elements.* Journal of Chemical Physics, 2003. **119**(21): p. 11113-11123.

54. Peterson, K.A., et al., *On the spectroscopic and thermochemical properties of clo, bro, io, and their anions.* Journal of Physical Chemistry A, 2006. **110**: p. 13877-13883.

55. Peterson, K.A. and Puzzarini, C., *Systematically convergent basis sets for transition metals. Ii. Pseudopotential-based correlation consistent basis sets for the group 11 (cu, ag, au) and 12 (zn, cd, hg) elements.* Theoretical Chemistry Accounts, 2005. **114**(4-5): p. 283-296.

56. Dunning, T.H., *Gaussian basis sets for use in correlated molecular calculations. I. The atoms boron through neon and hydrogen.* Journal of Chemical Physics, 1989. **90**(2): p. 1007-1023.

57. Kendall, R.A., Dunning, T.H., and Harrison, R.J., *Electron affinities of the first-row atoms revisited. Systematic basis sets and wave functions.* Journal of Chemical Physics, 1992. **96**(9): p. 6796-6806.

58. Woon, D.E. and Dunning, T.H., *Gaussian basis sets for use in correlated molecular calculations. Iii. The atoms aluminum through argon.* Journal of Chemical Physics, 1993. **98**(2): p. 1358-1371.

59. Jiao, Y. and Dibble, T.S., *Structures, vibrational frequencies, and bond energies of the brhgox and brhgxo species formed in atmospheric mercury depletion events.* Journal of Physical Chemistry A, 2017. **121**(41): p. 7976-7985.

60. J.Hehre, W., et al., *Molecular orbital theory of the electronic structure of organic compounds. V. Molecular theory of bond separation.* Journal of American Chemical Society, 1970. **92**(16): p. 4796-4801.

61. Asatryan, R., Bozzelli, J.W., and Simmie, J.M., *Thermochemistry of methyl and ethyl nitro, rno$_2$, and nitrite, rono, organic compounds.* Journal of Physical Chemistry A, 2008. **116**: p. 3172-3185.

62. Hohenberg, P. and Kohn, W., *Inhomogeneous electron gas.* Physical Review B, 1964. **136**(3B).

63. Kohn, W. and Sham, L.J., *Self-consistent equations including exchange and correlation effects.* Physical Review, 1965. **140**(4A): p. A1133-A1138.

64. Jiao, Y. and Dibble, T.S., *Quality structures, vibrational frequencies, and thermochemistry of the products of reaction of brhg(*) with no2, ho2, clo, bro, and io.* Journal of Physical Chemistry A, 2015. **119**(42): p. 10502-10.

65. Su, T. and Bowers, M.T., *Ion-polar molecule collisions: The effect of ion size on ion-polar molecule rate contants; the parameterization of the average-dipole-orientation theory.* International Journal of Mass Spectrometry and Ion Physics, 1973(12): p. 347-356.

66. Su, T. and Bowers, M.T., *Theory of ion-polar molecule collisions. Comparison with experimental charge transfer reactions of rare gas ions to geometric isomers of difluorobenzene and dichloroethylene.* Journal of Chemical Physics, 1973. **58**(7): p. 3027-3036.

67. Frisch, M.J., et al., *Gaussian 09, revision c.01.* 2009: Wallingford, CT.

68. Shepler, B.C., Balabanov, N.B., and Peterson, K.A., *Ab initio thermochemistry involving heavy atoms: An investigation of the reactions hg + ix (x = i, br, cl, o).* Journal of Physical Chemistry A, 2005. **109**(45): p. 10363-10372.

69. Balabanov, N.B. and Peterson, K.A., *Mercury and reactive halogens: The thermochemistry of hg + {cl$_2$, br$_2$, brcl, clo, and bro}.* Journal of Physical Chemistry A, 2003. **107**(38): p. 7465-7470.

70. Wennberg, P., et al., *Removal of stratospheric o$_3$ by radicals: In situ measurements of oh, ho$_2$, no, no$_2$, cio, and bro.* Science, 1994. **266**(21).

71. Ruscic, B., et al., *Active thermochemical tables: Thermochemistry for the 21st century.* Journal of Physics: Conference Series, 2005. **16**(561): p. 561-570.

72. Wang, H. and Bozzelli, J.W., *Thermochemical properties and bond dissociation energies for fluorinated methanol, ch_3-xfxoh, and fluorinated methyl hydroperoxides, ch_3-xfxooh: Group additivity.* Journal of Physical Chemistry A, 2016. **120**(35): p. 6998-7010.

73. Jung, D., Chung-Ju, C., and Bozzelli, J.W., *Structures, rotation barrier, and thermodynamic properties dhf°298, s°298, and cp(t)of chloromethyl hypochlorites ch_3ocl, ch_2clocl, $chcl_2ocl$, and ccl_3ocl.* Journal of Physical Chemistry A, 2000. **104**: p. 9581-9590.

74. Feller, D. and Peterson, K.A., *Re-examination of atomization energies for the gaussian-2 set of molecules.* Journal of Chemical Physics, 1999. **110**(17): p. 8384-8396.

75. Helgaker, T., et al., *Basis set convergence of correlated calculations on water.* Journal of Chemical Physics, 1997. **106**(23): p. 9639-9646.

76. Halkier, A., et al., *Basis set convergence in correlated calculations on ne, n_2 , and h_2o.* Chemical Physics Letters, 1998. **286**: p. 243-252.

77. Häussermann, U., et al., *Accuracy of energy adjusted quasirelativistic ab-initio pseudopotentials.* Molecular Physics, 1993. **78**(5): p. 1211-1224.

78. Balabanov, N.B. and Peterson, K.A., *A systematic ab initio study of the structure and vibrational spectroscopy of $hgcl_2$, $hgbr_2$, and hgbrcl.* Journal of Chemical Physics, 2003. **119**(23): p. 12271-12278.

79. Cheng, L. and Gauss, J., *Analytical evaluation of first-order electrical properties based on the spin-free dirac-coulomb hamiltonian.* Journal of Chemical Physics, 2011. **134**(24): p. 244112.

80. Nakajima, T. and Hirao, K., *The douglas-kroll-hess approach.* Chemical Reviews, 2012. **112**(1): p. 385-402.

81. Dibble, T.S., *Personal communication*. 2018: SUNY-ESF, 1 Forestry Drive Syracuse, NY 13210.

82. Hanson, D.R., et al., *Proton transfer reaction mass spectrometry at high drift tube pressure.* International Journal of Mass Spectrometry, 2003. **223–224**(0): p. 507-518.

83. Huey, L.G., Hanson, D.R., and Howard, C.J., *Reactions of sf6- and i- with atmospheric trace gases.* Journal of Physical Chemistry, 1995. **99**(14): p. 5001-5008.

84. Viggiano, A.A., Fernandez, A.I., and Troe, J., *Ion-molecule kinetics at 15-700 torr.* Physical Chemistry Chemical Physics 2005. **7**(7): p. 1533-1539.

85. Salcedo, D., et al., *Effect of relative humidity on the detection of sulfur dioxide and sulfuric acid using a chemical ionization mass spectrometer.* International Journal of Mass Spectrometry, 2004. **231**(1): p. 17-30.

86. Arijs, E., et al., *Stratospheric chemical ionization mass spectrometry: Nitric acid detection by different ion molecule reaction schemes.* International Journal of Mass Spectrometry, 1998. **181**: p. 99-111.

87. Viidanoja, J., Reiner, T., and Arnold, F., *Laboratory investigations of negative ion molecule reactions of formic and acetic acids: Implications for atmospheric measurements by ion-molecule reaction mass spectrometry.* International Journal of Mass Spectrometry, 1998. **181**: p. 31-41.

88. Amelynck, C., Fussen, D., and Arijs, E., *Reactions of nitric acid with di- and trichloride ions, di- and tri-iodide ions and with co−4 in the gas phase.* International Journal of Mass Spectrometry and Ion Processes, 1994. **133**(1): p. 13-28.

89. Eisele, F. and Tanner, D., *Measurement of the gas phase concentration of h2so4 and methna sulfonic acid and estimates of h2so4 production and loss in the atmosphere.* Journal of Geophysical Research, 1993. **98**(D5): p. 9001-9010.

90. Amelynck, C., Fussen, D., and Arijs, E., *Reactions of nitric-acid with diiodide and trichloride ions, diiodide and tri-iodide ions and with co4- in the gas-phase.* International Journal of Mass Spectrometry and Ion Processes 1994. **133**(1): p. 13-28.

91. Wlodek, S., Luczynski, Z., and Wincel, I., *Stabilities of gas-phase no3(hno3)n, n <= 6 clusters.* International Journal of Mass Spectrometry, 1980. **35**: p. 39-46.

92. Tröstl, J., et al., *The role of low-volatility organic compounds in initial particle growth in the atmosphere.* Nature, 2016. **533**(7604): p. 527-531.

93. Zhao, Y., and Truhlar, D. G., *The M06 suite of density functionals for main group thermochemistry, thermochemical kinetics, noncovalent interactions, excited sates, and transition elements: Two new functionals and systematic testing of four M06-class functionals and 12 other functionals.* Theoretical Chemistry Accounts, 2008. **120**: p. 215-241

94. Peverati, R., and Truhlar, D. G., *Quest for a universal density funtional: The accuracy of density functionals across a broad spectrum of databases in chemistry and physics.* Philosophical Transactions of the Royal Society A, 2014. **372**: p. 1-52

95. Ernzerhof, M., and Scuseria, G. E., *Assesment of the Perdew-Burke-Ernerhof exchange-correlation funtional.* Journal of Chemical Physics, 1999. **110**(11): p. 5029-5036

96. Adamo, C., and Barone, V., *Toward reliable density functional methods without adjustable parameters: The PBE0 model.* Journal of Chemical Physics, 1999. **110**(13): p. 6158-6170

97. Perdew, J. P., Burke, K., and Ernzerhof, M., *Generalized Gradient Approximation Made Simple.* Physical Review Letters, 1996. **77**(18): p. 3865-3868